MOMENTUM TRANSFER INSIDE A SINGLE FIBRE CAPILLARY MEMBRANE BIOREACTOR

by

BUNTU GODONGWANA

Thesis submitted in fulfilment of the requirements for the degree

Magister Technologiae: Chemical Engineering

in the

FACULTY OF ENGINEERING

at the

CAPE PENINSULA UNIVERSITY OF TECHNOLOGY

SUPERVISOR: **Mrs MARSHALL SHELDON**
CO-SUPERVISOR: **Dr DEON SOLOMONS**

CAPE TOWN
August 2007

DECLARATION

I, **Buntu Godongwana**, declare that the contents of this thesis represent my own unaided work, except where specifically acknowledged in the text, and that the thesis has not previously been submitted for academic examination towards any qualification. Furthermore, it represents my own opinions and not necessarily those of the Cape Peninsula University of Technology, the Mandela-Rhodes Foundation, or the National Research Foundation.

B. Godongwana

August 2007

ABSTRACT

Innovation in biotechnology research has resulted in a number of fungi being identified for diverse industrial applications. One such fungus, which is the subject of this study and has been one of the most intensively studied, is *Phanerochaete chrysosporium*. Much research has been done in developing optimized membrane bioreactor systems for the cultivation of these fungi because of their potent industrial applications. This research, however, has been hampered by the lack of a thorough understanding of the kinematics of flow, as well as the dynamics of the flow through these devices. Previous analyses of momentum transfer in membrane bioreactors have been entirely based on horizontally orientated bioreactor systems, and ignored the different modes of operations of membrane bioreactors. These models also ignored the osmotic pressure effects brought about by the retention of solutes on the membrane surface.

In this study, analytical and numerical solutions to the Navier-Stokes equations for the description of pressure, velocity, and volumetric flow profiles in a single fibre capillary membrane bioreactor (SFCMBR) were developed. These profiles were developed for the lumen and shell sides of the SFCMBR, taking into account osmotic pressure effects, as well as gel and/or cake formation on the lumen surface of the membrane. The analytical models developed are applicable to horizontal and vertical systems, as well as dead-end, continuous open shell, closed-shell, and shell side crossflow modes. A numerical scheme was also developed to complement the analytical models. The partial differential Navier-Stokes equations were solved in steps of time using a revised form of the SIMPLE algorithm. The mathematical expressions developed were proposed as solutions to transient-state, laminar, incompressible, viscous and isothermal flow inside a membrane with a variable hydraulic permeability.

The dimensionless form of the Navier-Stokes equations, after a consideration of the general applications of capillary membrane bioreactors, was shown to be a variant of Bessel's differential equation. This generic equation was solved for the specific case of no angular variations of the flow profiles. These expressions were based on a similarity solution since the wall Reynolds number was much smaller than one ($Re_w << 1$). The 'no slip' assumption was also imposed on the

analysis since the distortion of the velocity profile relative to that established in non-porous wall systems was also smaller than one ($\chi L << 1$).

The proposed models were tested on a vertically orientated membrane bioreactor, with a constant shell side pressure, operated in the dead-end mode with *P. chrysosporium* immobilised on the outside of a capillary polysulphone membrane. The resulting solutions from these models gave similar results to those in previous publications when ignoring gravitational effects, osmotic effects, and gel formation. From a sensitivity analysis, it was shown that the osmotic pressure flattens the lumenal velocity profiles and reduces the transmembrane pressure. Hence, the osmotic pressure was shown to have a negative effect on the membrane bioreactor efficiency. This study also showed that in the limiting case of the hydraulic permeability approaching zero, $\kappa \to 0$, the flow resembled that of a straight circular tube of constant cross section (Hagen Poiseuille flow). It was experimentally and theoretically shown that the hydraulic permeability of the polysulphone capillary membranes was a function of temperature. After monitoring the hydrostatic pressure profiles during operation, it was observed that the profiles follow a cycle similar to that of the growth phases of the *P. chrysosporium* fungus.

DEDICATION

To the memory of Mxokozeli Tylden Godongwana

"Kuthe kanti uyiNdoda kwedini!"

ACKNOWLEDGEMENTS

I would like to express my sincere appreciation and gratitude to the following persons for their support during my Magister Technologiae research at Cape Peninsula University of Technology:

- To my supervisors: Mrs Sheldon, for putting her faith in me, her guidance and motivation throughout the duration of my undergraduate and postgraduate studies. I will forever be grateful to her for nominating me for the Mandela-Rhodes scholarship, and providing me an opportunity to meet Mr Mandela. Dr Solomons, the brilliant mathematician, for making me realize that my mathematics is not so bad after all, and his priceless advice and support on mathematical principles covered in this thesis.

- The Mandela-Rhodes Foundation for their financial assistance, and more importantly their personal interest in my private and professional development.
- The National Research Foundation for financial support towards the completion of this research.
- Dr Alna van der Merwe for her contribution in validating some of the mathematical techniques in this research.
- Prof Rejoice Ngcongo for her continued support and encouragement in keeping me on track with my purpose.
- The memory of Dr Winston Leukes who, though under immense demands, was always available to make constructive comments on some of the topics covered in this work.
- Siphokazi Andries, Kashief Mohamed, Seteno Karabo Ntwampe, Fikiswa Majola, Simoné Collins, Debbie de Jager, and other colleagues in the biotechnology laboratory for all their assistance and advice.
- Ayanda Bambiso, Sheku Kanu, Ncedo Ntloko and Dr Patrick Ndakidemi for their support and encouragement in making this journey a wonderful and memorable one.

- Special thanks to Amanda Mokhatla, my dear sister Noluvuyo, and all my family and friends for helping me keep my mind off bugs and membranes when I couldn't.

RESEARCH OUTPUTS

Articles submitted to accredited journals

Godongwana, B., Sheldon, M.S. & Solomons, D.M. 2007. Momentum transfer inside a vertically orientated capillary membrane bioreactor. *Journal of Membrane Science,* 303: 86-99.

Conference presentations

Oral presentations

Godongwana, B., Sheldon, M.S. & Solomons, D. 2006. Momentum transfer inside a vertically orientated capillary membrane bioreactor. SAIChE (Western Cape Branch) Annual R & D Day [Stellenbosch, South Africa, 23 June 2006].

Poster snapshot presentations

Godongwana, B., Sheldon, M.S. & Solomons, D. 2005. Momentum transfer inside a vertically orientated capillary membrane bioreactor. 6th WISA-MTD Symposium and Workshop [George, South Africa, 13-15 March 2005].

TABLE OF CONTENTS

LIST OF FIGURES

LIST OF TABLES

LIST OF SYMBOLS

a	dimensionless entrance pressure drop
A	pressure constant (bioreactor of variable shell side pressure)
b	dimensionless gravitational acceleration
B	pressure constant (bioreactor of variable shell side pressure)
c	total concentration of ions in solution, kmol/m^3
C_i	integration constants, i = 1, 2, 3…
d_w	membrane wall thickness, m
d_g	gel layer thickness in the membrane lumen, m
D	pressure constant (bioreactor of variable shell side pressure)
D_{AB}	diffusivity of the molecule A in the solvent B, m^2/s
$e(x)$	local mass transfer coefficient, m^3/m^{2}s
f	fraction retentate
$f(R)$	arbitrary function of dimensionless radial coordinate
$f(Z)$	arbitrary function of dimensionless axial coordinate
g	gravitational acceleration, m/s^2
H_g	pressure constant (bioreactor of variable shell side pressure)
H	pressure constant neglecting gravitational acceleration
i	horizontal grid coordinate
j	vertical grid coordinate
J	flux, m^3/m^{2}s
$J_n(\alpha)$	Bessel function of order n of the first kind
k	hydraulic permeability, m^2
K	function of dimensionless time
L	membrane length, m
p	pressure, Pa
P	dimensionless pressure
q	arbitrary constant
Q	volumetric flowrate, m^3/s
r	radial coordinate, m
r_H	membrane hydraulic radius, m

R dimensionless radial coordinate

R^* Universal gas constant = 8.31451J/g-mol.K

Re_w wall Reynolds number ($\rho v_w r_H/\mu$)

Re_b bulk flow Reynolds number ($\rho v r_H/\mu$)

R_L membrane inner radius, m

S membrane resistance, m^{-1}

Sc Schmidt number ($\mu/\rho D_{AB}$)

t time, s

T temperature, K

U dimensionless axial velocity

v velocity, m/s

V dimensionless radial velocity

$Y_n(\alpha)$ Bessel function of order n of the second kind

z axial coordinate, m

Z dimensionless axial coordinate

Greek letters

α_n is the n^{th} root of the Bessel function $J_n(\alpha_n r)$

β dimensionless aspect ratio of the membrane (R_L/L)

χ distortion of the velocity profile, m^{-1}

ε surface porosity

ϕ slip coefficient

Φ osmotic pressure, Pa

γ shear rate, s^{-1}

Γ gamma function

η viscous force, $kg.m/s^2$

φ association parameter (2.6 for water)

κ dimensionless hydraulic permeability

λ shear stress, Pa

μ fluid dynamic viscosity, Pa.s

Π	dimensionless osmotic pressure
θ	angle in cylindrical coordinates, $\tan^{-1}(y/x)$
Θ	dimensionless function of the angle θ
ρ	fluid density, kg/m^3
τ	dimensionless time
ω	arbitrary constant
ϖ	dimensionless function of bioreactor dimensions
Ξ	function of the radial coordinate
ψ	dimensionless stream function
Ω	dimensionless flowrate
ζ	dimensionless function of transitional velocity

Subscripts

0	membrane entrance
1	membrane exit
2	extra capillary space radius
3	glass manifold inner radius
∞	steady-state
g	gel layer
in	internal fouling
L	membrane lumen
m	membrane matrix
S	shell side of membrane
$Sb\pi$	function of P_S, Π and b
τ	transient-state
w	wall
z, *y*, *x*	rectangular spatial co-ordinates
z, *r*, θ	cylindrical spatial co-ordinates
r, θ, ϕ	spherical co-ordinates

ABBREVIATIONS

BC	- Boundary condition
CFD	- Computational fluid dynamics
CTMP	- Chemi-thermomechanical pulping
HF	- Hollow fibre
IC	- Initial condition
LiP	- Lignin peroxidase
MnP	- Manganese peroxidase
MBR	- Membrane bioreactor
MGR	- Membrane gradostat reactor
PAH	- Polycyclic aromatic hydrocarbons
PCB	- Polychlorobiphenyls
P. chrysosporium	- *Phanerochaete chrysosporium*
PSu	- Polysulphone
RMP	- Refiner mechanical pulping
SFCMBR	- Single fibre capillary membrane bioreactor
SSC	- Steady state condition
TMP	- Transmembrane pressure
UF	- Ultrafiltration
WRF	- White rot fungus

1. INTRODUCTION

1.1 Background

The white-rot fungus (WRF), *Phanerochaete chrysosporium*, and its extracellular enzymes, Lignin Peroxidase (LiP) and Manganese Peroxidase (MnP), are promising for a number of industrial applications. This is as a result of this organism and its enzymes' ability to degrade lignin found in woody plants and its ability to function at extreme conditions of high temperatures (up to 40°C) and low pH of 4.5 (Kirk & Fenn, 1979; Tien & Kirk, 1988). Usage of the fungus and its extracellular enzymes has been reported in the treatment of hazardous waste (McGrath & Singleton, 2000), the mining industry (Martin, 2000), the wine industry (Howard *et al.,* 2003), and even in the biopulping of wood in the pulp and paper industry (Wall *et al.,* 1993).

Considerable research has been done in developing economically viable membrane bioreactor (MBR) systems for the cultivation of *P. chrysosporium* and the production of its ligninolytic enzymes (Willershausen *et al*., 1987; Venkatadri & Irvine, 1993; Moreira *et al*., 1997; Leukes, 1999; Domínguez *et al*., 2001). Leukes (1999) developed a membrane gradostat bioreactor (MGR), which uses to its advantage the nutrient gradients that are inherent of hollow fibre (HF) and capillary MBR's, for the continuous production of extracellular enzymes, Lignin and Manganese peroxidase (LiP and MnP), from *P. chrysosporium*. This bioreactor more closely resembles the natural growing conditions of the fungus than submerged fermentations (Leukes, 1999), and showed higher enzyme activities than previous and subsequent conventional bioreactor systems (Willershausen *et al*., 1987; Venkatadri & Irvine, 1993; Moreira *et al*., 1997; Domínguez *et al*., 2001). Following from the work of Leukes (1999) a number of other investigations have demonstrated the suitability and viability of the capillary polysulphone (PSu) MGR for LiP and MnP production (Govender, 2000; Solomon, 2001; Garcin, 2002; Ntwampe, 2005; Sheldon & Small, 2005). The capillary membranes used in constructing the MGR have been shown to offer many advantages over other membrane types.

The performance of these types of bioreactors is determined in large by the transport rate of the key nutrients and/or wastes through the membranes (Kelsey *et al.*, 1990; Catapano *et al.*, 1990). It is therefore crucial to have a complete description of momentum as well as mass transfer

through these devices for an optimum bioreactor design. A number of experimental and theoretical investigations have been conducted with the aim of modelling the momentum transfer in HF and capillary membranes (Tharakan & Chau, 1986; Catapano *et al.*, 1988; Bruining, 1989; Kelsey *et al.*, 1990; Catapano *et al.*, 1990; Moussy, 1999; Elshahed, 2004). Most of these investigations however were unsuccessful in providing adequate mathematical models for pressure and velocity profiles, which also account for the different modes and configurations of operation of membrane bioreactors. Kelsey *et al.* (1990) gave detailed mathematical models for velocity and pressure profiles, which also account for the different modes of operation. However, the models proposed by Kelsey *et al.* (1990) were restricted to the horizontally orientated bioreactor of varying shell hydrostatic pressure, ignored osmotic pressure effects that result from solute rejection on the membrane surface, and also ignored the additional resistance layers to permeation due to gel formation.

The Navier-Stokes equations are regarded as the fundamental equations governing fluid motion. Although there are no analytical solutions for the complete Navier-Stokes equations, these equations can still be solved numerically to attain a more descriptive analysis than a simplified analytical solution. Damak *et al.* (2004) used an implicit finite difference method to numerically develop pressure and velocity fields of crossflow filtration. This model however does not take into account the different modes of operation of membrane bioreactors and also ignores osmotic pressure effects.

Experimental work on LiP and MnP production by Garcin (2002) and Ntwampe (2005) has shown the vertically orientated single fibre capillary membrane bioreactor (SFCMBR) to be more suitable than the horizontal orientation. Currently there are no mathematical models to completely describe the momentum transfer through a vertically orientated capillary MGR, which also takes into account osmotic pressure effects, gel formation on the surface of the membrane, as well as the mode of operation of the bioreactor. This study is aimed at developing these mathematical models for the purpose of scaling up the MGR system for continuous LiP and MnP production.

1.2 Research Objectives

This study will focus on an analytical and numerical solution of the governing differential equations for viscous flow for the derivation of mathematical models to predict pressure drops and velocity profiles, during the cultivation of *P. chrysosporium* in a vertically orientated SFCMBR. The specific objectives will be to:

- Construct mathematical models for the momentum transfer inside a SFCMBR, which account for the different modes of operation, and compare results with those obtained from the literature.

- Include osmotic pressure effects and gel formation in a vertically orientated SFCMBR operated in the dead-end mode, and compare theoretical results obtained from the developed vertical model with experimental data.

- Test the validity of the developed models during operation with and without *P. chrysosporium* growth on the external surface of the membrane.

- Simulate velocity and pressure profiles of nutrient through a SFCMBR using numerical techniques and compare results with experimental data.

1.3 Overview

1.3.1 The research topic

Momentum transfer in capillary and HF membrane reactors has been a very extensively studied subject since the integration of the two disciplines of membrane technology and biotechnology in the early 1970's, which gave rise to a new technology called MBR's. An instructive review of the developments leading to this relatively new technology was given by Belfort (1989), and a summary of the momentum transfer models by Chatterjee and Belfort (1986). Unfortunately, most of these models and their later versions are restricted to specific conditions of operation, and

none of them were developed for a vertically orientated system. These models also tend to neglect the osmotic pressure effects, and gel formation on the surface of the membrane lumen.

1.3.2 Hypothesis

The premise of this research is to combine the Navier-Stokes equations and Darcy's law, taking into account osmotic effects and gel formation in a vertically orientated SFCMBR, for the prediction of velocity and pressure profiles. The models will be adjusted to account for the different modes and configurations of operations of HF and capillary membrane bioreactors.

1.3.3 Collection of the relevant data

The nature and scope of the research topic only allow for a quantitative approach to the analysis. This will take the form of validating the developed model predictions against measured experimental data. The theoretical model predictions will be for axial and radial velocity profiles, volumetric flowrates, as well as pressure profiles along the length of the SFCMBR. The measured experimental data will include pressure measurements at the inlet and outlet of the SFCMBR, biofilm thickness, gel layer thickness, membrane hydraulic permeability, and redox potentials of the permeate solution during the cultivation of *P. chrysosporium*.

1.3.4 Analysis of the data and interpretation of the results

The collected experimental data will be compared to the developed model predictions, as well as other widely accepted literature models, and the discrepancies will be discussed. The emphasis will be on the effects brought about by the inclusion of gravitational acceleration, gel formation, and osmotic pressure on the momentum transfer study.

2. LITERATURE REVIEW

2.1 Introduction

Recent developments in biotechnology have led to a number of enzymes, secreted by bacteria and fungi, being identified for diverse industrial applications. In some applications the usage of these microbes is far more viable than conventional separation and/or processing techniques. *P. chrysosporium* has been one of the most widely studied white-rot fungi (WRF). The properties and some of the most common applications of *P. chrysosporium* are detailed in this chapter.

This chapter will also highlight the recent developments in bioreactor designs for the continuous production of enzymes from *P. chrysosporium*. The membrane gradostat (MGR) developed by Leukes (1999) will be described. Membrane bioreactors (MBR's) can be operated in various modes, depending on the specific application. These different modes and their flow characteristics will be discussed in detail, as well as the most widely used momentum transfer models for flow through MBR's.

2.2 *Phanerochaete chrysosporium* and its properties

P. chrysosporium is a genome of WRF, which are so named because they degrade brown lignin and leave behind white cellulose. WRF are the only microbes capable of efficient depolymerisation and mineralisation of lignin (Mielgo *et al.,* 2003; JGI, 2004; Ferapontova *et al.,* 2006). *P. chrysosporium* has been one of the most intensively studied WRF (Hiratsuka *et al.,* 2005). This fungus, like all other WRF, secrete an array of peroxidases and oxidases that act non-specifically via the generation of lignin free radicals, which then undergo spontaneous cleavage reactions. These peroxidases include: LiP, MnP, endoglucanases, glyoxal oxidase, xylanases, pyranose 2-oxidase, mannose-6-phosphatases and many others. The non-specific nature and exceptional oxidation potential of these enzymes has attracted considerable interest for application in bioprocesses, such as organopollutant degradation and fibre bleaching (JGI, 2004; Ferapontova *et al.,* 2006). LiP and MnP are useful in the bioremediation of a wide variety of organic waste by-products including: textile dyes polyethylene, pesticides, herbicides, dynamite,

PAHs, polychlorobiphenyls (PCBs), and oil-contaminated soil (Dzul-Puc *et al.,* 2005; Fungal Genomics Project, 2005; De *et al.,* 2006; Chander & Arora, 2007).

2.3 Applications of *Phanerochaete chrysosporium*

P. chrysosporium has several features that have drawn attention for a number of possible uses. Firstly, unlike some WRF, it leaves the cellulose of wood virtually untouched. Secondly, it has a very high optimum temperature of 40°C (Kirk & Fenn, 1979; Tien & Kirk, 1988), which means it can grow on wood chips in compost piles that attain a very high temperature (JGI, 2004). This fungus also has an uncommon optimum pH of 4.5, making contamination of production cultures less of a problem (Kirk & Fenn, 1979). These characteristics point to possible applications in biotechnology. A number of studies have been conducted with the aim of exploiting some of these characteristics of *P. chrysosporium* and its ligninolytic enzymes, LiP and MnP, for various industrial applications such as:

a) The biological delignification (biopulping) of wood for the pulp and paper industry. Biopulping, in turn, has been used as an alternative to thermomechanical pulping and chemi-thermomechanical pulping (CTMP). This process involves the pre-treatment of wood chips with WRF prior to refiner mechanical pulping (RMP) or thermomechanical pulping. This process saves energy of up to 50% compared to CTMP, RMP or thermomechanical pulping without biological pre-treatment; it improves paper strength properties significantly as compared to the other processes without biological pre-treatment (Wall *et al.,* 1993).

b) Bioremediation, the process of using biological treatment systems to destroy or reduce the concentrations of hazardous waste from contaminated sites. During bioremediation, a variety of pollutant transformation products will be created, which may have toxic synergistic interactions and may not be detected by chemical analysis (McGrath & Singleton, 2000). The usage of *P. chrysosporium* on the bioremediation of soil, contaminated with the biocide *Pentachlorophenol*, has been reported (McGrath & Singleton, 2000).

c) The disposal of highly polluted olive by-products. A major environmental threat in the olive industry is the aqueous liquor, which comes from the vegetation water and the soft tissues of

the fruits. *P. chrysosporium* has been used to depolymerize polyphenolic fractions less than 8kDa and, with the use of LiP induction medium, polyphenolic fraction greater than 60kDa from olive mill wastewater (Sayadi *et al.,* 2000).

d) The recovery of wastewater contaminated with various heavy metals and organic pollutants for reuse in agricultural and other applications. The efficiency of water usage, especially in areas with fast population growth and industrial development, is becoming a major environmental issue. A number of studies have been performed with the aim of recovering water from process plants using *P. chrysosporium* and its extracellular enzymes MnP and LiP (Nilsson *et al.,* 2006; Hai *et al.,* 2006; Dhouib *et al.,* 2006; Wu & Yu, 2007).

e) The extraction of gold from damaged underground timber in the mining industry. A portion of the impregnated gold within the supporting timber, which results from blasting and crushing, is located so deep within the complex wood matrix that cyanidation on its own prove insufficient for recovery (Van der Plas, 1998). WRF can completely degrade the lignin, which forms 30% of woody plant tissues, by producing extracellular enzymes that catalyse the depolymerization of the lignin (Martin, 2000).

f) The transformation of "lignocellulose waste" into value-added products such as Auxin and Abscisic acid (Unyayar *et al.,* 2000), Vanillin and Gallic acid (Howard *et al.,* 2003), using *P. chrysosporium*.

2.4 Developments in bioreactor design for cultivation of *Phanerochaete chrysosporium*

A MBR can be defined as a flow reactor within which membranes are used to separate cells or enzymes from the feed or product streams. A common characteristic of most MBR's is that feed streams are delivered continuously. Products may be removed continuously, but in some applications they must be harvested intermittently or at the end of the run. Polymeric microfiltration (MF) or ultrafiltration (UF) membranes are most commonly used for the construction of MBR's, although other types of membranes have been used including: ceramic, silicone rubber and ion exchange membranes (Asenjo & Merchuk, 1994).

The applications of *P. chrysosporium* and its ligninolytic enzymes that have potential industrial importance, have been the driving force for research in the design of continuous economically viable bioreactor systems. In initial attempts, Willershausen *et al.* (1987) demonstrated growth of the fungus in the form of mycelial mats inside a 1.0 litre vessel bioreactor. The bioreactor consisted of silicone tubing wrapped around 4 stainless steel sticks to form a spiral. Venkatadri and Irvine (1993) have demonstrated the viability of the use of HF and silicone membrane stirred-tank bioreactor systems for the cultivation of *P. chrysosporium* and the production of LiP. In the silicone membrane stirred-tank bioreactor, very similar to that of Willershausen *et al.* (1987), the membrane appeared to be an excellent support for attached fungal growth. In the case of the HF membrane reactor, the membrane provided a shear-free environment and convenient separation of LiP from the cells and replacement of the growth medium. Venkatadri and Irvine (1993) also achieved to generate LiP on a semi-continuous basis using the silicone membrane stirred tank bioreactor.

One major problem inherent in MBR's is that radial nutrient gradients within the biofilm have been shown to exist in these systems. This phenomenon occurs because when nutrients are supplied to the biofilm the organisms closest to the membrane have first access to it, while cells furthest away from the membrane surface are normally starved of nutrients. On the contrary, a major advantage of the HF bioreactor system over submerged culture bioreactors is that it simulates the native state of the fungus, which have evolved on a solid-air interface. Leukes (1999) developed a MGR, which uses a synthetic capillary UF membrane as support matrix, which exploits the phenomenon of nutrient gradients as a solution to the challenge of continuous secondary metabolite production. The MGR showed higher enzyme activities than previous and subsequent conventional continuous bioreactor systems (Willershausen *et al.,* 1987; Venkatadri & Irvine, 1993; Moreira *et al.,* 1997; Domínguez *et al.,* 2001). This has led to an interest in optimisation studies of the operation (Garcin, 2000) and design (Govender, 2002; Ntwampe, 2005) of the MGR for LiP and MnP production. Other materials, such as ceramic membranes, have also been investigated for the supporting matrix of the MGR as an alternative to polysulphone (PSu) capillary membranes (Sheldon & Small, 2005).

2.5 Membranes

2.5.1 Characteristics of capillary and HF membranes

Capillary and HF membranes are examples of the tubular-type geometry UF membranes. HF membranes refer to very small diameter membranes. The most successful one has an outer diameter of only 93μm and is used for reverse osmosis (Perry *et al.,* 1998). HF membranes usually have a microporous skin, 1 to 2μm in thickness, where bioseparation takes place and a macroporous spongy matrix, 50 to 100μm thick, supporting the thin layer. Capillary membranes on the other hand are slightly larger diameter membranes, typically 0.5 to 5 mm in diameter. Capillary and HF membrane modules offer the greatest surface area per volume and hence the most efficient type of membrane separation. Some of the properties of these membranes include: continuous removal of inhibitory wastes; high cell densities; decreased contamination risks; and higher volumetric productivities. These membranes allow the possibility for simultaneous reaction and separation of products or wastes (Tharakan & Chau, 1986; Belfort, 1989; Kelsey *et al.*, 1990; Venkatadri & Irvine, 1993). Capillary and HF membranes are ideal for microbial growth because they provide a shear free environment, since the circulating medium does not come into direct contact with the cells immobilised on the external surface of the fiber (Belfort, 1989; Venkatadri & Irvine, 1993).

The structure of artificial membranes (HF, capillary, tubular, spiral wound, monolith, etc.) is generally referred to either as symmetric or asymmetric. Symmetric membranes have a uniform structure and are typically 10 to 30μm in thickness. Asymmetric membranes comprise a highly porous spongy support layer, often 50 to 500μm thick, with a thin layer about 0.5μm in depth that provides the permselective properties of the membrane. An asymmetric membrane provides less resistance to mass transfer than a comparable isotropic (symmetric) membrane but is more prone to mechanical damage (Asenjo & Merchuk, 1994).

2.5.2 Membrane materials and the polysulphone membrane

Membranes may be made from physical solids, organic or non-organic (metal, ceramic, etc.), homogeneous films (polymer, metal, etc.), heterogeneous solids (polymer mixes, mixed glasses, etc.), solutions (usually polymer) and liquids. Polymeric membranes dominate the membrane

separation field because they are well developed and competitive in separation performance and economics. Their usual final form is as HF or capillaries or as flat sheet, either of which is incorporated in a module (Perry *et al.,* 1998).

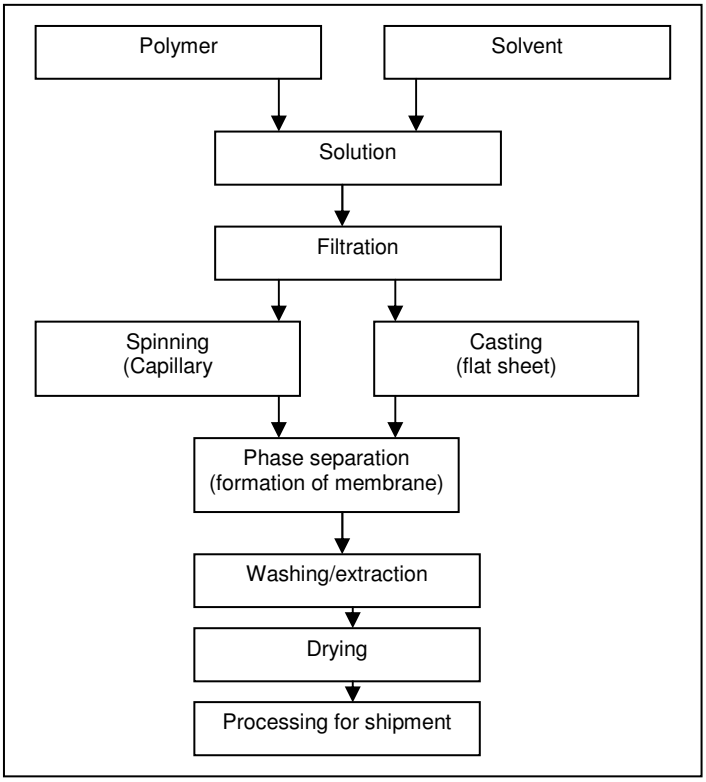

Figure 2-1: Flow diagram of the process of membrane manufacturing (Locatelli *et al.*, 2003)

A flow diagram of the general manufacturing process of polymeric membranes is shown in Figure 2-1. In principle a polymer has to be dissolved in a suitable solvent, pressed through a spinneret, and after the phase separation (membrane building) the membrane is washed and dried. Membranes with unique morphologies can be produced by manipulating the various factors that control the wet-phase inversion manufacturing process by which most asymmetric membranes are formed (Locatelli *et al.*, 2003).

The PSu capillary UF membrane used in this study was developed by Jacobs and Leukes (1996) and Jacobs and Sanderson (1997), by adjustment of the membrane spinning solution formulation and fabrication protocol. This membrane offers many advantages when used in a MBR, such as low resistance to liquid transport and a large external surface area.

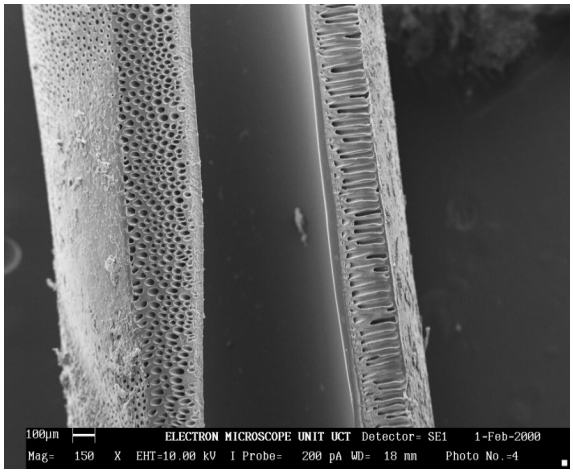

Figure 2-2:A scanning electron microscope image of the PSu capillary membrane (Solomon & Petersen, 2002)

The microporous structure and hydrophilic surfaces of the externally unskinned PSu capillary membranes, as shown in Figure 2-2, allow free exchange of nutrients and metabolic products between the cells, immobilised on the outside of the membrane, and the circulating medium flowing within the membrane (Jacobs & Leukes, 1996; Jacobs & Sanderson, 1997).

2.6 Modes and orientations of operation

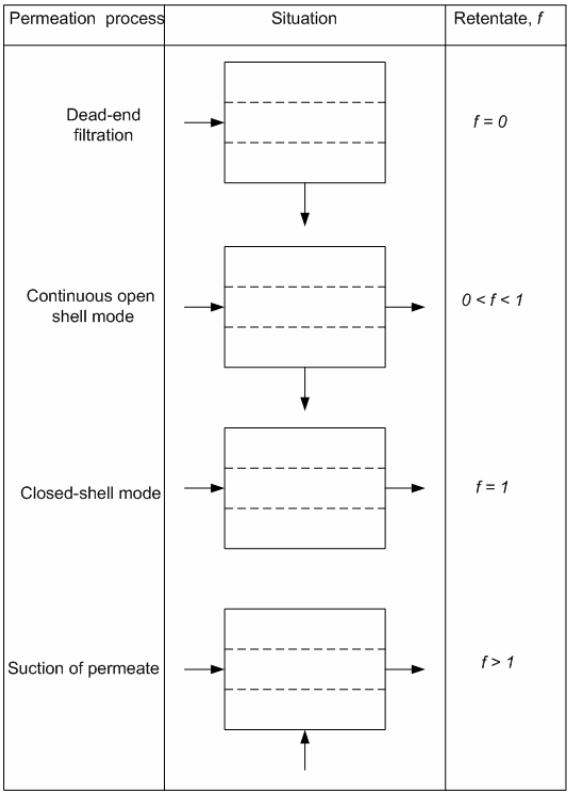

Figure 2-3: Some modes of operation of hollow fibre devices (Bruining, 1989)

The basic process of any membrane separation involves a feed mixture separated into a retentate (part of the feed that does not pass through the membrane) and a permeate (part of the feed that passes through the membrane) as shown in Figure 2-3. The basic design of HF and capillary membrane modules consists of a bundle of fibres, in an equilateral array as shown in Figure 2-4, sealed into a cylindrical casing forming a shell-and-tube configuration. Bruining (1989) described four of the most commonly utilised modes of operation of HF membrane devices by introducing the factor *f*, which denotes the ratio of the lumen side exit flow to the lumen side entrance flow. These modes of operation are shown schematically in Figure 2-3 and are: dead-end filtration, continuous open-shell mode, closed-shell mode and suction of permeate.

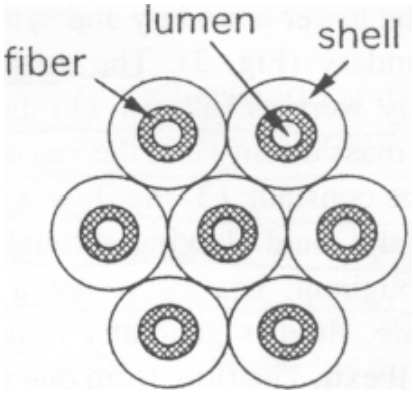

Figure 2-4: Schematic of hollow fibres in an equilateral array (Kelsey *et al.*, 1990)

In dead-end filtration, the feed stream enters the lumen side of the membrane and a permeate leaves continuously in the shell side. In this mode there is no retentate as shown in Figure 2-3; therefore, the fraction retentate, *f*, is zero. In continuous open-shell ultrafiltration, the feed stream is still through the lumen and the permeate leaves through a shell side port. The retentate flows at the downstream end of the fibre, and hence the feed will be greater than the retentate flowrate by the amount of permeate through the membrane shell ($0< f <1$). The tube side pressure is always greater than the shell side pressure in both dead-end and continuous open shell modes (Tharakan & Chau, 1986).

In closed-shell, there is no net volumetric solvent flow from the fibres to the shell; that is, the feed flowrate is equal to the retentate flowrate ($f = 1$). The transmembrane flux (flow between lumen and shell regions) for the first part of the membrane is directed towards the shell, and for the latter half of the membrane back to the lumen feed as shown in Figure 2-5. This phenomenon,

also referred to as convective recirculation or Starling recirculation flow, leads to non-uniform distribution of biomass in HF systems operated in the closed shell mode (Tharakan & Chau, 1986; Bruining, 1989; Kelsey *et al.*, 1990; Catapano *et al.*, 1990).

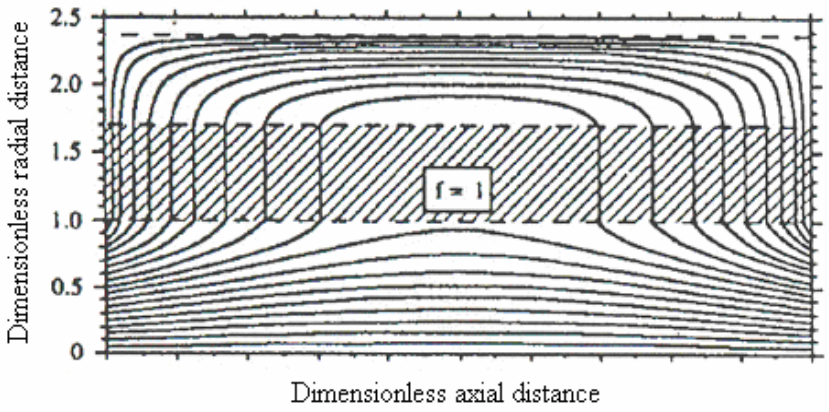

Figure 2-5: Convective recirculation in a membrane device (modified from Kelsey *et al.*, 1990)

In suction of permeate/shell side crossflow mode, the feed stream is delivered to the shell side and distributed uniformly along the length of the fibre. The feed flows across the fibre bed while simultaneously permeating the fibre wall and exiting from the tube side of the membrane. The shell side pressure is kept greater than the lumen side, with a positive transmembrane flux towards the lumen side. The tube side pressure gradient is relatively insignificant, and the result is a more uniform transmembrane flux along the axis of the fibre unit (Tharakan & Chau, 1986).

The different modes of operation of HF and capillary membranes have been shown, experimentally (Tharakan & Chau, 1986) and theoretically (Bruining, 1989; Kelsey *et al.*, 1990), to exhibit different pressure distributions as elaborated earlier in this section. This information is important for choosing and designing an optimum bioreactor configuration for continuous enzyme production.

MBRs are generally operated either horizontally or vertically depending on their application; however, other orientations are also in use. Recent results from experimental work on LiP and MnP production has shown the vertically orientated single fibre capillary membrane bioreactor (SFCMBR) to be more suitable than the horizontal orientation (Garcin, 2002; Ntwampe, 2005). This stems from the following observations: (a) in the horizontally orientated SFCMBR the PSu

capillary membrane tends to sag as the biofilm develops on the surface of the membrane, thus stretching the membrane which results in uneven growth; (b) the biofilm is denser, in both PSu and ceramic membranes, in the vertical configuration; (c) there is uneven growth of the biofilm in the horizontal configuration, with the biofilm thickest at the entrance of the membrane and gradually declines in thickness to almost no biofilm at the exit of the membrane; (d) higher glucose and ammonia consumption in the vertical configuration than in the horizontal; and (e) contamination of permeate is less of a problem in the vertical configuration as compared to the horizontal.

2.7 Mathematical models for momentum transfer

2.7.1 Significance of momentum transfer analysis in bioreactor design

The optimum production of enzymes in MBR's is influenced by a number of factors. One of the major factors is the pattern of flow of nutrients to the microorganisms or culture, which is regulated by the transmembrane flux. The flux of a membrane defines its productivity and therefore, largely influences the capital cost and the operating cost of a membrane unit operation (Perry *et al.,* 1998). The axial lumenal pressure gradient adversely affects transmembrane flux, and is thought to be the limiting factor in bioreactor scale up (Garcin, 2002). In effect, the performance of MBR's is largely dependent on the axial lumenal pressure gradient. It is also known that concentration polarization of dissolved solutes, which tends to depress membrane efficiencies, can be predicted and controlled at the membrane-solution interface through an understanding of the fluid mechanics and mass transfer (Chatterjee & Belfort, 1986). Thus, a momentum and mass transfer analysis are crucial for the purposes of enhancing MBR efficiencies. In some applications however, the momentum transfer can be solved independently of the mass transfer and vice-versa. The Schmidt number, *Sc*, is used to indicate the dominating transport phenomena as either momentum or mass transfer (Moussy, 1999).

2.7.2 Description of momentum transfer

The study of momentum transfer is concerned with the kinematics of flow (the description and visualisation of flow), as well as the dynamics of the flow (the forces necessary to produce the flow). Models of the fluid are necessary to visualize its path and to apply to it the fundamental principles of nature as it moves from one point to the next (Munson *et al.,* 2006).

Generally, there are three models of flow: (a) the finite control volume; (b) the infinitesimal fluid element and (c) the kinetic theory model of flow. When Newton's second law of motion is applied to any of the three models of flow mathematical equations can be extracted, which embodies the physical principle of Newton's second law (Anderson, 1995). The resulting mathematical equations are the governing equations for momentum transfer, for the specific model of flow chosen. Theoretically, from these equations a complete momentum transfer analysis can be carried out. Velocity fields, pressure profiles and acceleration fields can be obtained for any specific fluid flow application.

In this study, the infinitesimal fluid element model of flow was used, meaning the fluid was imagined to consist of infinitesimally small fluid elements with a differential volume. Moreover, the fluid element was assumed to be moving along a streamline with a velocity vector equal to the flow velocity at each point.

2.7.3 Previous models of momentum transfer

As an attempt to give a description of the flow behaviour, in particular momentum transfer, through MBR's for the purposes of design, process optimisation and control, a number of mathematical models have been proposed. Most of these models stem from the governing differential equations for incompressible Newtonian fluids, the Navier-Stokes equations; however other approaches have also been followed.

An excellent review was given by Chatterjee and Belfort (1986) of previously published models of flow through porous ducts of different cross-sectional geometries. These models were proposed as solutions to laminar, incompressible, steady-state flow. None of the tubular geometry models reviewed in this study takes into account the different modes of operation of MBR's. Chatterjee and Belfort (1986) also developed analytical and numerical solutions for flow in an idealized spiral wound membrane module. A perturbation technique was used to solve the Navier-Stokes equations to obtain the analytical solutions. This study revealed that a similarity solution cannot be found for wall Reynolds numbers $Re_w > 1$. Similarity in velocity profiles only exists for 'fully developed' flows. Tharakan and Chau (1986) gave a qualitative description of the pressure distribution in HF systems in different modes of operation. Their analysis included an explanation for the non-uniform distribution of biomass in HF systems operated in the closed and

open shell axial feed modes. No mathematical models were given with this analysis to give a sound quantitative account of the pressure and velocity distributions. On the other hand, Catapano *et al.* (1988) provided expressions for the axial and radial velocity components of a fluid flowing through a cell-loaded capillary membrane. These expressions were modifications of the Hagen-Poiseuille equation, taking into account the diminution of axial flow rate due to permeate flow. However, these expressions did not account for the mode of operation of the MBR or osmotic effects.

Bruining (1989) described convective flow in HF membranes by developing equations for pressure drops and flows at various operating modes. However, Bruining's models do not give information on velocity profiles in either the lumen or the shell sides. Kelsey *et al.* (1990) developed, from the Navier-Stokes equations, models for velocity and pressure profiles, which also accounts for the different modes of operations of HF and capillary membranes. Kelsey *et al.* (1990) also gave a visual description of the flow by means of streamlines. However, the treatment of Kelsey *et al.* (1990) was restricted to the horizontally orientated HF bioreactor system and does not consider osmotic pressure effects. Catapano *et al.* (1990) outlined the importance of convective fluxes in determining MBR performance. Their solutions were based on the analysis of Apelblat *et al.* (1974), with the estimate that the distortion of the velocity profile (relative to that established in non-porous walls) is negligible. Catapano *et al.* (1990) also established that, if the condition of no-slip velocity is assumed then the axial pressure profile can be assumed to be linear. Moussy (1999) applied analytical solutions developed by Yuan and Finkelstein (1956) to characterise flow in the lumen of a continuous arteriovenous HF hemofilter, and also developed expressions for the radial and axial velocity profiles in the shell. The expressions also took into account the axial variations in lumen pressure, shell pressure, and osmotic pressure. These expressions were restricted to the open shell mode and do not consider the resistance brought about by gel formation on the membrane lumen.

Diverging from the assumption of no-slip velocity, Elshahed (2004) developed velocity and pressure profiles for blood flows in capillaries under the Starling hypothesis. A perturbation technique was used to solve the Navier-Stokes and continuity equations. What is interesting to note in Elshahed's research is the variation of the velocity profile with changes in the slip coefficient. When the slip coefficient is taken as zero (as in most studies) the axial velocity profile coincides with the no-slip profile. More recently, Damak *et al.* (2004) developed a fluid

dynamic model of crossflow filtration by coupling the Navier-Stokes equations and Darcy's law. The model was solved using an implicit finite difference method, substituting the derivatives of flow equations with a second-order accurate central difference scheme (this method is explained in Section 4.2). Like many of its predecessors, this model does not take into account different modes of operation and ignores osmotic effects. This is in spite of studies (Patkar *et al.*, 1994; Taylor *et al.*, 1994; Taylor & Boukouris, 1995) that have shown that secondary fluid flows within the extra-capillary space of HF bioreactors, which tend to depress reactor productivity, can be minimised through manipulation of the osmotic pressure.

2.8 Summary and significance of literature study

The significance of this literature review is that it highlights developments made over the past years in studies of MBR designs, for the continuous production of enzymes from *P. chrysosporium*. Some of the properties that make this fungus one of the most intensively studied fungus were detailed. This literature review also highlighted the importance of a thorough momentum transfer analysis in the optimisation of a MBR. Some of the most widely used mathematical models for momentum transfer, with their short-comings, were discussed.

Results from experimental work on LiP and MnP production has shown the vertically orientated SFCMBR to be more suitable than the horizontal orientation. This suggests the need for either modifications on the horizontal models or totally new mathematical models to account for the vertical orientation. All of the currently available literature on modelling momentum transfer is based on horizontally orientated MBR's. These models also tend to neglect the osmotic pressure effects and gel formation on the surface of the membrane. Research on osmotic effects, however, has indicated that secondary fluid flows can be minimised through manipulation of the osmotic pressure.

The models developed in this study were intended to fill these gaps; in particular models that account for the different modes of operations, applicable in both horizontal and vertical configurations, also taking into account osmotic effects and gel formation.

3. THEORY

3.1 Introduction

This chapter is concerned with the theory pertaining to fluid motion in a capillary membrane bioreactor (MBR) and its application will be elaborated in Chapter 5. Since a detailed knowledge of the pressure and velocity fields of the fluid, as it moves through the membrane, is required, a point-relationship has to be developed for both pressure and velocity profiles. This approach, of seeking a point relationship between flow variables, is referred to as the differential analysis of fluid motion. Unfortunately, this approach is quite complicated and a number of simplifying assumptions have to be made regarding the flow. The differential equations of motion with their general assumptions will be discussed. These equations are generally applicable for bulk flows contained in non-porous materials. For porous materials, such as capillary membranes, a number of models exist for predicting the flux. These models will be discussed, and the effect of flux deterioration as a result of concentration polarization will also be described.

3.2 Differential equations of motion

3.2.1 Navier-Stokes and continuity equations

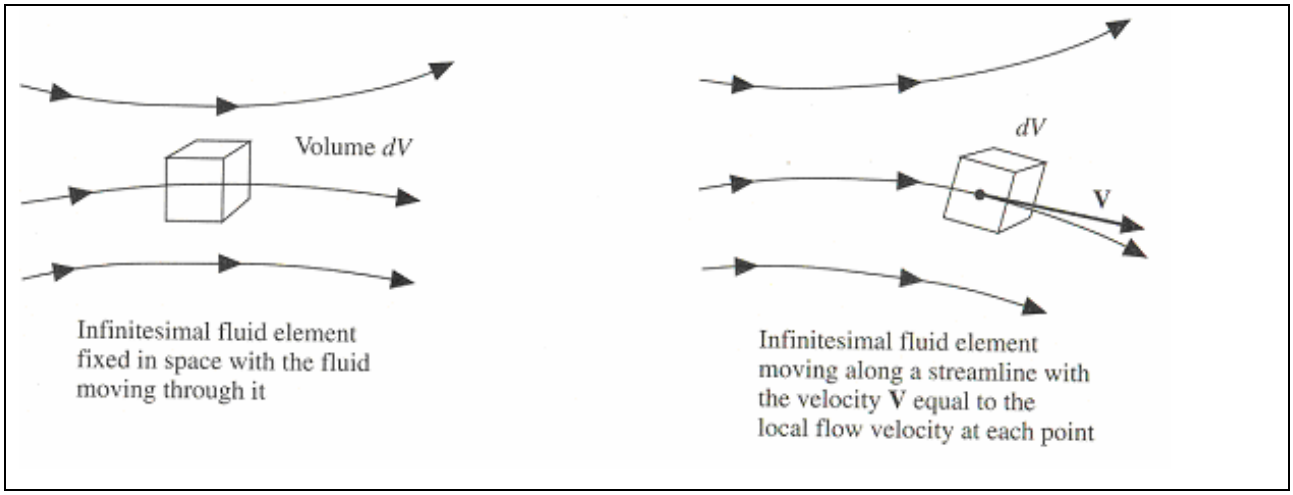

Figure 3-1: An infinitesimal element model of flow (Anderson, 1995)

The governing equations of momentum transfer, and the continuity equation, can be presented in various forms depending on the fluid model chosen. These mathematical expressions will either be in the conservation or non-conservation form depending on whether the fluid element chosen

is fixed in space or moving along with the bulk of the fluid as shown in Figure 3-1. The governing equations can also be presented as either partial derivatives or integrals depending on whether a finite control volume or infinitesimal fluid element is chosen to represent the fluid (Anderson, 1995).

The differential equations that describe in detail the flow of incompressible Newtonian fluids are referred to as the Navier-Stokes equations. For the z, r, and θ components in cylindrical co-ordinates (see Appendix G) the equations in non-conservation form are respectively (Bird *et al.,* 2002):

$$\rho\left(\frac{\partial v_z}{\partial t}+v_r\frac{\partial v_z}{\partial r}+\frac{v_\theta}{r}\frac{\partial v_z}{\partial \theta}+v_z\frac{\partial v_z}{\partial z}\right)= \mu\left[\frac{1}{r}\frac{\partial}{\partial r}\left(r\frac{\partial v_z}{\partial r}\right)+\frac{1}{r^2}\frac{\partial^2 v_z}{\partial \theta^2}+\frac{\partial^2 v_z}{\partial z^2}\right]-\frac{\partial p}{\partial z}+\rho g_z \qquad \textbf{3-1}$$

$$\rho\left(\frac{\partial v_r}{\partial t}+v_r\frac{\partial v_r}{\partial r}+\frac{v_\theta}{r}\frac{\partial v_r}{\partial \theta}-\frac{v_\theta^2}{r}+v_z\frac{\partial v_r}{\partial z}\right)= \mu\left[\frac{1}{r}\frac{\partial}{\partial r}\left(r\frac{\partial v_r}{\partial r}\right)-\frac{v_r}{r^2}+\frac{1}{r^2}\frac{\partial^2 v_r}{\partial \theta^2}-\frac{2}{r^2}\frac{\partial v_\theta}{\partial \theta}+\frac{\partial^2 v_r}{\partial z^2}\right]-\frac{\partial p}{\partial r}+\rho g_r \qquad \textbf{3-2}$$

$$\rho\left(\frac{\partial v_\theta}{\partial t}+v_r\frac{\partial v_\theta}{\partial r}+\frac{v_\theta}{r}\frac{\partial v_\theta}{\partial \theta}+\frac{v_\theta v_r}{r}+v_z\frac{\partial v_\theta}{\partial z}\right)= \mu\left[\frac{1}{r}\frac{\partial}{\partial r}\left(r\frac{\partial v_\theta}{\partial r}\right)-\frac{v_\theta}{r^2}+\frac{1}{r^2}\frac{\partial^2 v_\theta}{\partial \theta^2}+\frac{2}{r^2}\frac{\partial v_r}{\partial \theta}+\frac{\partial^2 v_\theta}{\partial z^2}\right]-\frac{1}{r}\frac{\partial p}{\partial \theta}+\rho g_\theta \qquad \textbf{3-3}$$

and the continuity equation:

$$\frac{\partial \rho}{\partial t}=-\left[\frac{1}{r}\frac{\partial(\rho r v_r)}{\partial r}+\frac{1}{r}\frac{\partial(\rho v_\theta)}{\partial \theta}+\frac{\partial(\rho v_z)}{\partial z}\right] \qquad \textbf{3-4}$$

In vector notation the Navier-Stokes equations are presented more compactly as:

$$\rho\frac{D\vec{v}}{Dt}=-\vec{\nabla}p+\eta\nabla^2\vec{v}+\rho\vec{g} \qquad \textbf{3-5}$$

where the term $\rho\, D\vec{v}/Dt$ represents the mass of fluid element per unit volume times acceleration, $\vec{\nabla}p$ represents the pressure force on the fluid element per unit volume of element, $\eta\nabla^2\vec{v}$ represents the viscous force on the element per unit volume, and $\rho\vec{g}$ the gravitational force on the element per unit volume. A principal difficulty in solving the Navier-Stokes equations is their

nonlinearity arising from the convective acceleration terms, on the left-hand-side of Equation 3-5. There are no general analytical methods for solving nonlinear partial differential equations, and each problem must be considered individually (Munson *et al.*, 2006). Special methods have to be used in order to simplify and solve these equations, like defining stream functions and velocity potentials, etc. Bird *et al.* (2002) discuss these special methods in detail. The stream function will be explained in Section 3.2.2 of this thesis. It is widely accepted that if the ratio of the inertial to viscous forces at the wall (of the surface containing the flow) is much less than 1 then the inertial terms on the left-hand-side of Equations 3-1, 3-2, and 3-3 can be neglected (Berman, 1953; Kelsey *et al.*, 1990; Moussy, 1999). In most viscous flows, normal stresses (e.g. $\partial^2 v_z / \partial z^2$ in Equation 3-1) are much smaller than shear stresses and are often neglected (Anderson, 1995).

3.2.2 The Stream function

Although fluid motion can be quite complicated, there are various concepts that can be used to help in the visualization and analysis of flow fields. The stream function ψ is a convenient parameter of representing and solving plane two-dimensional flow. By plane, two-dimensional flow is meant that there are only two velocity components, such as v_r and v_z, with $v_\theta = 0$ and no θ dependence. When the fluid is incompressible, meaning its density, ρ, is not a function of pressure and temperature, the continuity equation (Equation 3-4) reduces to (Munson *et al.*, 2006):

$$\frac{1}{r}\frac{\partial(rv_r)}{\partial r} + \frac{\partial v_z}{\partial z} = 0 \qquad \textbf{3-6}$$

Equation 3-6 contains two variables, v_r and v_z, which are related by a function $\psi(r,z)$, called the stream function, defined such that it satisfies the two-dimensional continuity equation (Munson *et al.*, 2006):

$$v_z = -\frac{1}{r}\frac{d\psi}{dr} \qquad \textbf{3-7}$$

and

$$v_r = \frac{1}{r}\frac{d\psi}{dz} \qquad \textbf{3-8}$$

By defining a stream function, the two-dimensional analysis is simplified to only one unknown function $\psi(r,z)$, instead of the two functions, $v_r(r,z)$ and $v_z(r,z)$. The stream function is very useful because its physical significance is that, in steady-state flow, lines defined by $\psi = constant$ are the paths of fluid elements (or streamlines as they are commonly known). A stream function exists for all two-dimensional, steady incompressible flow, whether viscous or inviscid (Bird *et al.,* 2002).

3.3 Flow through ultrafiltration membranes

3.3.1 Darcy's law

The combination of free flow and flow through porous media occurs in a wide range of fluid processes, such as membrane cross flow filtration. A fluid dynamic description of free flows is usually modelled using the Navier-Stokes equations described in Section 3.2.1. Darcy's law for the representation of non-inertial, incompressible flows in porous media with a small porosity (normally in the range of 10 to 20%) is widely accepted and used (Damak *et al.,* 2004). Darcy's law, which states that the pressure gradient through a porous media is directly proportional to the flowrate, can be expressed mathematically as follows (Bird *et al.,* 2002):

$$J = -\frac{k_m}{\mu}\left(\nabla p - \rho g\right) \qquad \textbf{3-9}$$

where μ is the fluid dynamic viscosity in Pa.s, k_m is the membrane hydraulic permeability in m^2, ρ is fluid density in kg/m^3, g is the gravitational acceleration in m/s^2 and, ∇p is a vector called the "gradient of (the scalar) p" in Pa/m given by (Bird *et al.,* 2002):

$$\vec{\nabla} p = \frac{\partial p}{dr} + \frac{1}{r}\frac{\partial p}{d\theta} + \frac{\partial p}{dz} \qquad \textbf{3-10}$$

where p is hydrostatic pressure in Pa and r, θ and z are spatial coordinates in m, and J is the volumetric flux of the solvent through the membrane in m^3/m^2s. The volumetric flux, J, can be defined as the volumetric productivity of a membrane unit per unit membrane area. Grouping of the terms in Equation 3-9, when assuming one dimensional flow through the pores of the membrane, results in:

$$J = \frac{\Delta p}{\mu S_m} + \frac{\rho g k_m}{\mu} \qquad \textbf{3-11}$$

where S_m is the clean membrane resistance in m^{-1}. One oversight of using Darcy's law for predicting flux is that this equation does not account for fouling and gel formation on the surface of the membrane lumen. A more rigour expression for predicting flux includes additional resistance from gel layers and internal pore fouling in the analysis, and is given by (Tu *et al.,* 2005):

$$J = \frac{\Delta p}{\mu\left[S_m + S_g + S_{in}\right]} + \frac{\rho g}{\mu}\left(\frac{1}{k_m} + \frac{1}{k_g} + \frac{1}{k_{in}}.\right)^{-1} \qquad \textbf{3-12}$$

where S_g, k_g and S_{in}, k_{in} are the resistance and hydraulic permeability of the gel layer and internal pore fouling respectively. Equation 3-12 is a more accurate expression for representing flux in ultrafiltration membranes, and may be written more explicitly as:

$$J = -\frac{\left(\frac{1}{k_m} + \frac{1}{k_g} + \frac{1}{k_{in}}\right)^{-1}}{\mu}\left[\frac{\left(p_S + \Phi\right) - p_L}{\left(d_w + d_g + d_{in}\right)} - \rho g\right] \qquad \textbf{3-13}$$

where p_S and p_L are the shell and lumenal side hydrostatic pressures in Pa respectively; Φ is the osmotic pressure in Pa; d_w, d_g, d_{in} and is the gel thickness, internal pore thickness, and membrane wall thickness in m respectively.

3.3.2 The Hagen-Poiseuille model

The Hagen-Poiseuille is another model often used to describe liquid flow through the pores of a membrane. When this model is applied to ultrafiltration membranes the assumptions are that all the pores in the membrane are of the same size and uniformly distributed and that no fouling and negligible concentration polarization occurs on the surface of the membrane (Brouckaert *et al.,* 1995). The Hagen-Poiseuille is expressed as:

$$J = \frac{\varepsilon d_{(pore)}^2 p_{(TMP)}}{32\mu d_w} \qquad \textbf{3-14}$$

where J is the permeate volumetric flux in m^3/m^2s, ε is the surface porosity, p_{TMP} is the applied transmembrane pressure in Pa, d_{pore} is the mean pore diameter in m, and d_w the membrane thickness in m. The transmembrane pressure (TMP) can be defined as the 'force' that drives liquid flow through the crossflow membrane. In tangential flow devices, the TMP is calculated as

an average related to the pressures of the inlet, outlet and permeate ports. The TMP can be expressed as:

$$p_{TMP} = \left(\frac{p_0 + p_1}{2} \right) - p_S \qquad \textbf{3-15}$$

where p_0 and p_1 are the inlet and outlet lumenal hydrostatic pressures, respectively. When real feed solutions are considered, the driving forces in both Darcy's and the Hagen-Poiseuille laws should be replaced by the difference between the transmembrane hydrostatic pressure and the transmembrane osmotic pressure (Brouckaert *et al.,* 1995). The inclusion of the osmotic pressure recognises that it is really the total thermodynamic potential that drives the transmembrane transport (Bird *et al.,* 2002). For most work, the van't Hoff approximation for osmotic pressure gives an adequate estimate (Perry *et al.,* 1998):

$$\Phi = c_w R^* T \qquad \textbf{3-16}$$

where c_w is the total concentration of ions at the wall-membrane interface on the feed side in kmol/m^3, T is the absolute temperature of the solution in K, and R^* is the universal gas constant 8.31451J/g-mol.K. When a number of macromolecular species are present then the osmotic pressure will be made up of contributions from the individual species:

$$\Phi = \sum_{i=1}^{n} \omega_i c_{wi} R^* T \qquad \textbf{3-17}$$

3.3.3 Hydraulic permeability of ultrafiltration membranes

The hydraulic permeability of an ultrafiltration membrane can be defined as the volumetric flow that the membrane allows to pass through an effective area of 1m^2 when a transmembrane pressure of 1Pa is applied across the membrane at a specific time interval. As much as there are a number of models available for predicting the hydraulic permeability of a membrane there are also a wide variety of units used to express this parameter. Most models used to predict the hydraulic permeability are based on the Forchheimer equation (Moreira *et al.,* 2004):

$$\frac{\Delta p}{d_w} = \frac{\mu}{k_1} J + \frac{\rho}{k_2} J^2 \qquad \textbf{3-18}$$

where k_1 (m^2) and k_2 (m) are referred to as Darcyan and non-Darcyan permeability parameters, respectively. These terms are assumed to be a function of the membrane characteristics only (Moreira *et al.,* 2004). The Ergun (1952) correlation is the most widely used for the determination of k_1 and k_2, and was derived from the flow through granular beds (Moreira *et al.,* 2004):

$$k_1 = \frac{\varepsilon^3 d_{pore}^2}{150(1-\varepsilon)^2} \qquad \textbf{3-19}$$

$$k_2 = \frac{\varepsilon^3 d_{pore}}{1.75(1-\varepsilon)} \qquad \textbf{3-20}$$

where d_{pore} is the pore diameter of the membrane in m.

The Kedem-Katchalsky equation, derived from irreversible thermodynamics is generally used to experimentally evaluate the hydraulic permeability of membranes (Liao *et al.,* 2005):

$$J = k_m(p_0 - p_1) - \sigma k_m R^* T(c_{s0} - c_{s1}) \qquad \textbf{3-21}$$

where J is the velocity, or volumetric flux, in m/s of the solvent leaving the surface of the membrane, c_{s0} and c_{s1} are the solute concentrations in kg/m^3 on each side of the membrane, R^* is the universal gas constant in J/g-mol.K, and σ is the reflection coefficient. The hydraulic permeability is obtained by running water through the lumen of the membrane, in which case the Kedem-Kathchalsky equation simplifies to:

$$J = k_m(p_0 - p_1) \qquad \textbf{3-22}$$

From Equation 3-22 the value of the hydraulic permeability k_m for a given membrane is the slope of the graph of the volumetric flux J versus the pressure difference of the inlet and outlet, $p_0 - p_1$, (Liao *et al.,* 2005).

The effect of variations in temperature on membrane hydraulic permeability was studied by Garcin (2002) and more recently by Sharaf and Abo-Elmagd (2005). The results obtained in these studies indicated that the hydraulic permeability of the polymeric membranes was very much dependant on temperature whereas that of paper-type membranes was temperature independent (Sharaf & Abo-Elmagd, 2005). For a specific batch of polymeric membranes, the hydraulic

permeability at the specific operating temperature needs to be evaluated so as to more accurately evaluate pressure moduli and predict flux (Garcin, 2002).

3.3.4 Concentration polarization

Concentration polarization is the accumulation of retained solutes on the surface of a membrane to form a concentration boundary layer. Due to the transport of solutes from the bulk solution to the membrane surface and subsequent retention, the concentration of the retained macromolecules is maximal at the membrane surface and decreases back to the bulk concentration with distance from the membrane. This distance is known as the concentration boundary layer thickness (Moussy, 2000). Permeate flux deterioration due to fouling and concentration polarization greatly impacts the performance and economics of membrane processes, particularly in water treatment applications (Tu *et al.,* 2005). Concentration polarization is caused by a combination of factors including TMP, solute concentration and crossflow velocity (Liao *et al.,* 2005). The effect of this phenomenon is that during operation up to a certain TMP difference, the ultrafiltration flux increases almost linearly with the TMP difference. At higher pressures the concentration boundary layer grows in thickness as the TMP increases. The flux is then independent of the pressure (and in some extreme instances a negative response to pressure) as illustrated in Figure 3-2 (Perry *et al.,* 1998; Moussy, 2000).

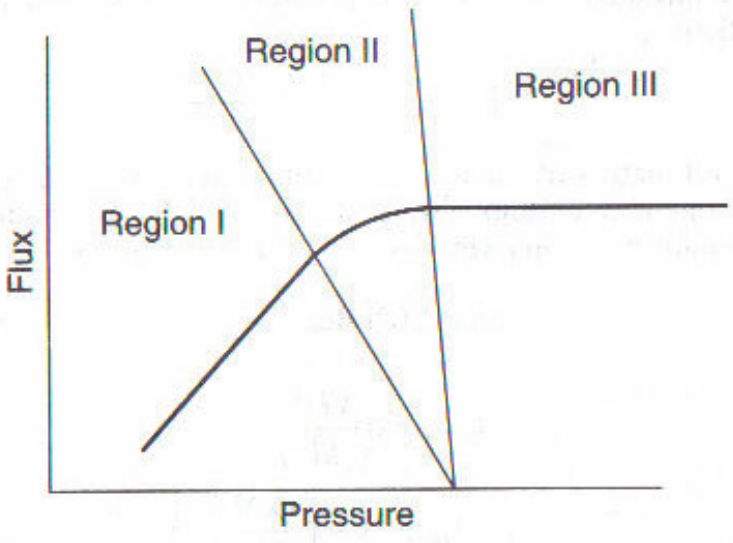

Figure 3-2: Characteristic curve for flux through an ultrafiltration membrane as a function of transmembrane pressure (Perry *et al.,* 1998)

4. NUMERICAL METHODS

4.1 Introduction

Mathematical models of many biochemical processes, such as the one considered in this study, give rise to systems of differential–algebraic equations. Very few of these equations can be solved analytically, and the majority of them are solved using numerical algorithms. Of the various techniques available for the numerical solution of governing differential equations of fluid flow, the following three types are most common: (a) the finite difference method, (b) the finite element (or finite volume) method, and (c) the boundary element method. In each of these methods the continuous flow field is described in terms of discrete values at prescribed locations. By this technique the differential equations are replaced by a set of algebraic equations that can be solved on a computer (Munson *et al.*, 2006). This chapter describes the finite difference method of discretizing a differential equation and, in brief, the usage of computational fluid dynamics (CFD) techniques in solving flow problems. Bessel functions, which arise frequently in studies of applied mathematics, will also be discussed. The relevance and application of the theory discussed in this chapter is elaborated in Chapter 5.

4.2 The finite difference method

Analytical solutions of partial differential and/or integral equations involve closed-form expressions which give the variations of the dependant variable continuously throughout the domain. In contrast, numerical solutions can give answers at only discrete points in the domain, called grid points and the partial derivative/integral is said to be discretized. Discretization of partial differential equations is called finite differences, and discretization of integral equations is called finite volumes (Anderson, 1995).

Most common finite-difference representations of derivatives are based on Taylor's series expansion:

$$u_{i+1,j} = u_{i,j} + \left(\frac{\partial u}{\partial x}\right)_{i,j} \Delta x + \left(\frac{\partial^2 u}{\partial x^2}\right)_{i,j} \frac{(\Delta x)^2}{2} + \left(\frac{\partial^3 u}{\partial x^3}\right)_{i,j} \frac{(\Delta x)^3}{6} + \cdots \qquad \textbf{4-1}$$

where $u_{i,j}$ and $u_{i+1,j}$ denotes the value of u at points (i,j) and $(i+1,j)$ respectively.

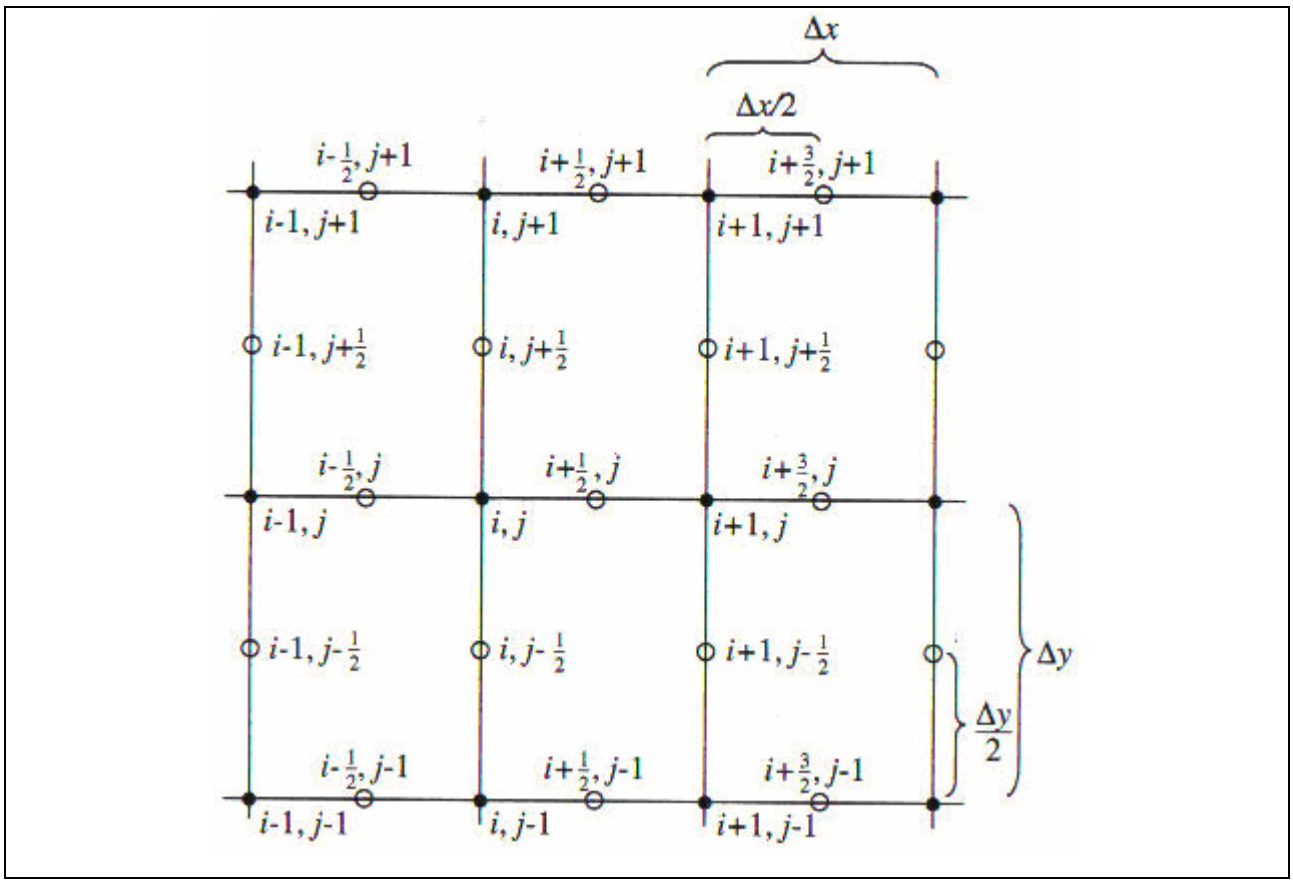

Figure 4-1: A staggered grid

Equation 4-1 can be algebraically manipulated to make the partial derivative $(\partial u/\partial x)_{i,\,j}$ the subject of the equation. Therefore,

$$\left(\frac{\partial u}{\partial x}\right)_{i,j} = \frac{u_{i+1,j} - u_{i,j}}{\Delta x} \qquad \textbf{4-2}$$

This is called a forward difference of first-order accuracy or a first-order forward difference. Referring to Figure 4-1, it can be seen that the finite difference expression uses information to the right of grid point (i,j); that is, it uses $u_{i+1,\mathrm{j}}$ as well as $u_{i,j}$. No information to the left of (i,j) is used, and hence the name forward difference. A similar expression can be obtained from Equation 4-1 by making use of grid points (i,j) and $(i\text{-}1,j)$

$$\left(\frac{\partial u}{\partial x}\right)_{i,j} = \frac{u_{i,j} - u_{i-1,j}}{\Delta x} \qquad \textbf{4-3}$$

This is called a first-order rearward (or backward) difference. Often in CFD applications, first-order accuracy is not sufficient (Anderson, 1995). A second-order finite difference quotient

makes use of information from both sides of the grid point located at (i,j); that is, it uses $u_{i+1,j}$ as well as $u_{i-1,j}$:

$$\left(\frac{\partial u}{\partial x}\right)_{i,j} = \frac{u_{i+1,j} - u_{i-1,j}}{2\Delta x} \qquad \textbf{4-4}$$

Hence the finite difference quotient is called a second order central difference (Anderson, 1995).

Once a differential equation has been discretized as described above, a number of algorithms are available to carry out the solution of the equation and this is the domain of a relatively new field called computational fluid dynamics.

4.3 Computational fluid dynamics

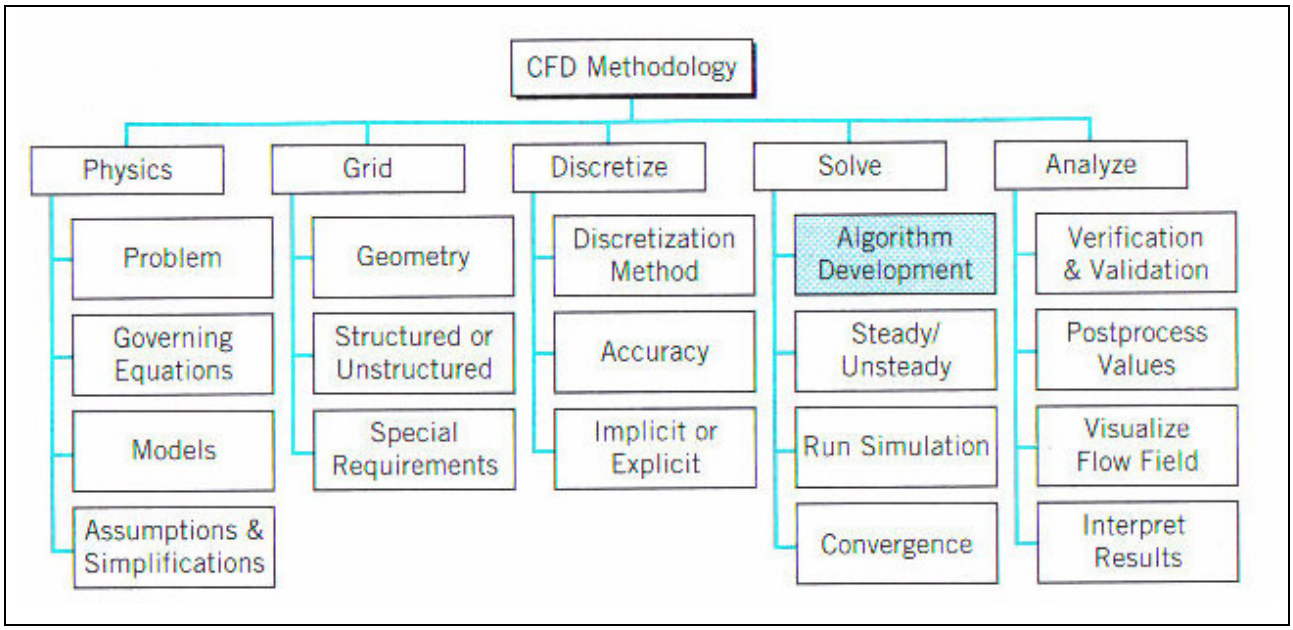

Figure 4-2: A flow chart of general CFD methodology (Munson *et al.*, 2006)

CFD entails breaking down a physical system, for example the lumen side of a membrane bioreactor or the air around an aircraft, into a large number of cells or control volumes (the mesh or grid). In each of these cells, the partial differential equations describing the fluid flow (the Navier-Stokes equations) are rewritten as algebraic equations that relate the pressure, velocity, temperature and other variables, such as species concentrations, to the values in the neighbouring cells (Munson *et al.,* 2006). This procedure is referred to as discretization of the governing

equations (refer to Section 4.2). These equations are then solved numerically to obtain flow field values at the discrete points in space and/or time.

Most applications of CFD take the same basic approach and can be summarized in the flowchart shown in Figure 4-2. Some of the differences in the approaches include problem complexity, available computer resources, available expertise in CFD, and whether a commercially available CFD package is used, or a problem-specific CFD algorithm is developed (Munson *et al.,* 2006). Naturally, the first step is to define the problem and presenting it in a "well-posed manner". In the context of CFD, a problem is said to be "well-posed" if: the solution to a partial differential equation exists and is unique, if the solution depends continuously upon the initial and boundary conditions (Anderson, 1995). In essence this means a thorough understanding of the physics of the flow. Once the problem is "well-posed" the next step in any CFD model is to create a geometry that represents the object being modelled. From this point, a mesh is generated which creates the cells or control volumes.

Once the mesh is complete, the model input values are specified and the software then solves the equations of state for each cell until an acceptable convergence is achieved. When the model has been solved, the results can be analyzed both numerically and graphically (CFX, 2005).

Even though computer codes have been developed to handle these equations, the definition of consistent initial conditions is an essential step to assure convergence of the numerical solvers. Generally, the definition of consistent initial conditions is the most difficult step in the solution of a DAE set (Resende *et al.,* 2002).

4.4 Bessel functions

Bessel's differential equation can be expressed as follows:

$$r^2u'' + ru' + \left(r^2 - n^2\right)u = 0 \qquad n \geq 0 \qquad \left(' = \frac{d}{dr}\right) \qquad \textbf{4-5}$$

In mathematics Bessel functions are standard solutions of Bessel's differential equation. These functions arise frequently in advanced studies of applied mathematics, specifically in physical situations where there is cylindrical symmetry. This occurs in problems involving electric fields,

vibrations, heat conduction, optical diffraction and others. The general solution of Equation 4-5 is given by (Spiegel, 1974):

$$u = c_1 J_n(r) + c_2 Y_n(r) \qquad \textbf{4-6}$$

The solution $J_n(r)$, that has a finite limit as r approaches zero, is called a Bessel function of the first kind and order n. The solution $Y_n(r)$ that has no finite limit as r approaches zero is called a Bessel function of the second kind and order n or Neumann function. If the independent variable r in Equation 4-5 is changed to qr where q is a constant, the resulting equation is:

$$r^2 u'' + ru' + \left(q^2 r^2 - n^2\right)u = 0 \qquad n \geq 0 \qquad \textbf{4-7}$$

with general solution:

$$u = c_1 J_n(qr) + c_2 Y_n(qr) \qquad \textbf{4-8}$$

where the Bessel function of the first kind of order n is defined as (Spiegel, 1974):

$$J_n(r) = \frac{r^n}{2^n \Gamma(n+1)}\left\{1 - \frac{r^2}{2(2n+2)} + \frac{r^4}{2\times 4(2n+2)(2n+4)} - \ldots\right\} \qquad \textbf{4-9}$$

where $\Gamma(n+1)$ is the gamma function. If n is a positive integer, $\Gamma(n+1) = n!$, $\Gamma(1) = 1$. The Bessel function of the second kind of order n is defined as (Spiegel, 1974):

$$Y_n(r) = \begin{cases} \dfrac{J_n(r)\cos n\pi - J_{-n}(r)}{\sin n\pi} & n \neq 0, 1, 2, 3, \ldots \\ \lim\limits_{p \to n} \dfrac{J_p(r)\cos p\pi - J_{-p}(r)}{\sin p\pi} & n = 0, 1, 2, 3, \ldots \end{cases} \qquad \textbf{4-10}$$

When n is zero in Equation 4-9 the series expansion becomes:

$$J_0(r) = 1 - \frac{r^2}{2^2} + \frac{r^4}{2^2 4^2} - \frac{r^6}{2^2 4^2 6^2} + \ldots \qquad \textbf{4-11}$$

From Equation 4-11 the following relation can be extracted:

$$J_0'(\alpha_n r) = -J_1(\alpha_n r) \qquad \textbf{4-12}$$

where α_n is the nth root of the Bessel function $J_n(\alpha_n r)$. Bessel functions have many other interesting and important properties, among them being the following (Lowry *et al.*, 1971):

$$\frac{d}{dr}\left\{r^n J_n(r)\right\} = r^n J_{n-1}(r), \qquad \frac{d}{dr}\left\{r^{-n} J_n(r)\right\} = -r^{-n} J_{n+1}(r) \qquad \textbf{4-13}$$

$$\int_0^x rJ_n^2(\alpha_m r)dr = \frac{x^2}{2}\left[J_n'(\alpha_m x)^2 + \left(1 - \frac{n^2}{\alpha_m^2 x^2}\right)J_n^2(\alpha_m x)\right] \qquad \textbf{4-14}$$

$$\int_0^x r\left(x^2 - r^2\right)J_0(\alpha_m r)dr = -\frac{4x}{\alpha_n^3}J_0'(\alpha_m x) \qquad \textbf{4-15}$$

$$\int_0^x J_n(\alpha_l r)J_n(\alpha_m r)rdr = 0, \qquad (l \neq m) \qquad \textbf{4-16}$$

The above properties of Bessel functions, Equations 4-13 to 4-16, demonstrate the orthogonality of these functions.

5. MODEL DEVELOPMENT

5.1 Introduction

This chapter presents both analytical and numerical solutions to the Navier-Stokes equations for the description of fluid motion through a SFCMBR. The theory discussed in Chapter 3 and 4 will be used in formulating pressure profiles, stream functions, as well as velocity and volumetric flow profiles through a SFCMBR device. The model solutions presented are intended for use in the scaling-up of a continuous bioreactor system, and hence all the model parameters will be defined as dimensionless variables.

A major problem in solving the Navier-Stokes equations is that there are no general analytical methods for solving nonlinear partial differential equations, and this practically means that each problem must be solved from scratch. However, after a consideration of the general applications of capillary membrane bioreactors it is possible to develop a generic equation. This generic equation will be developed for laminar flows through cylindrical surfaces, and will be solved for the specific case where angular variations of the flow are negligible.

5.2 Model assumptions

The theoretical models to be developed will be based on the following conditions of operation and assumptions:

- *the system is isothermal*. In essence this means that the energy equation has been decoupled from the momentum transfer. Darcy's law, the continuity and Navier-Stokes equations were all that was necessary to solve the velocity and pressure fields.

- *the flow regime within the fiber lumen is fully developed, laminar, and homogeneous*. Since the flow regime is very sensitive in the immobilisation of spores (i.e. high flowrates will lead to spores detached from the membrane, and poor mass transfer characteristics), in almost all HF and capillary membrane bioreactors the flow regime will be laminar.

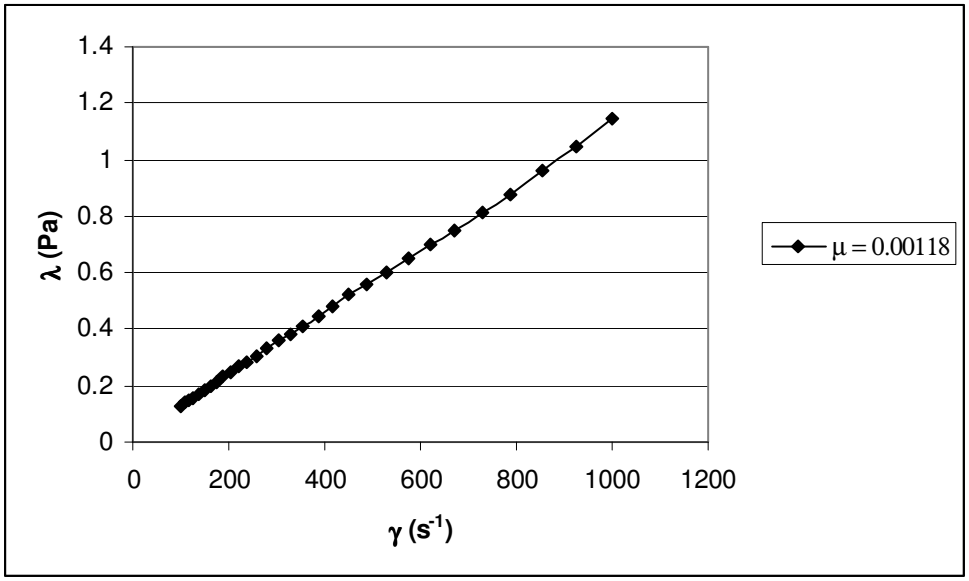

Figure 5-1: The flow curve of the nutrient solution at 37°C

- *physical and transport parameters (e.g. density, viscosity and diffusivity) are constant*. This holds only if the nutrient solution is an incompressible Newtonian fluid, which is true for the nutrient solution used in this research as described by Tien and Kirk (1988). Figure 5-1 is a plot of shear stress λ versus shear rate γ of the nutrient solution, obtained from a Paar Physica MCR300 Rheometer, which illustrates the Newtonian behaviour of the nutrient solution used in this study. The slope of the graph is constant, as is the case for all Newtonian fluids. This is compatible with the initial assumption that the temperature *T* is constant, since dynamic viscosity is a function of temperature.

- *the membrane hydraulic permeability is uniform throughout*. The PSu capillary membranes used in this study are asymmetric membranes, however, for simplicity in the model development they were assumed to be isotropic.

- *the entrance velocity to the membrane bioreactor is governed by Poiseuille's equation*.

- *the momentum transfer can be solved independently of the mass transfer*. A useful dimensionless parameter for indicating whether or not the mass transfer can be decoupled from the momentum transfer analysis is the Schmidt number, *Sc*:

$$Sc = \frac{\mu}{\rho D_{AB}} \qquad \textbf{5-1}$$

Sc larger than 1 indicate that the concentration boundary layer is much smaller than the momentum boundary layer (Moussy, 1999). The *Sc* for the nutrient solution used was much greater than 1 (see Appendix E).

- *no fungal growth occurs in the membrane lumen*. The membrane has an internal UF skin preventing growth to the lumen side

- *in the dense and in the spongy layers of the membrane the flow is only one dimensional.* That is, there are no axial components of the velocity profiles in the membrane matrix (see Figure 2-2).

- *The aspect ratio, β, of the membrane is much smaller than unity.* The aspect ratio is the ratio of the membrane inner radius to the effective membrane length, and if it is much smaller than unity then normal stress effects are negligible.

5.3 Dimensionless variables

For the purpose of data correlation, model studies, and scale-up, there are many advantages of expressing the differential equations of motion and their solutions in dimensionless form as opposed to working with actual units. For the current study it is necessary to introduce the following dimensionless variables:

$$U = \frac{v_z}{v_{z0}} = \frac{v_z}{(p_0 - p_1)R_L^2 / 4\mu L} \qquad \textbf{5-2}$$

where U represents the dimensionless axial velocity of the membrane, p_0 and p_1 are the inlet and outlet hydrostatic pressures respectively, v_z and v_{z0} are the axial velocities at a point z and at the entrance respectively, R_L is the membrane inner radius and, L the length of the membrane.

$$V = \frac{v_r}{v_{z0}} = \frac{v_r}{(p_0 - p_1)R_L^2 / 4\mu L} \qquad \textbf{5-3}$$

where V is the dimensionless radial velocity. The velocity components, U and V, are expressed as ratios of the maximum axial velocity at the membrane entrance. The maximum axial velocity at the membrane entrance is expressed by Poiseuille's equation:

$$v_{z0} = \frac{R_L^2}{4\mu}\left(\frac{p_0 - p_1}{L}\right) \qquad \textbf{5-4}$$

Similarly, the volumetric flowrate, Ω, is taken to be a ratio of the maximum entrance volumetric flowrate:

$$\Omega = \frac{Q}{Q_{z0}} \qquad \textbf{5-5}$$

Again, the maximum axial volumetric flow at the membrane entrance is assumed to be expressed by Poiseuille's law:

$$Q_{z0} = \frac{\pi R_L^4 (p_0 - p_1)}{8\mu L} \qquad \textbf{5-6}$$

The pressures are given as ratios of the total pressure drop along the membrane lumen:

$$\Pi = \frac{4\Phi}{(p_0 - p_1)} \qquad \textbf{5-7}$$

$$P = \frac{4p}{(p_0 - p_1)} \qquad \textbf{5-8}$$

where Φ is the osmotic pressure, and p is the hydrostatic pressure. The spatial coordinates, z and r, are normalized about their axis:

$$Z = \frac{z}{L} \qquad \textbf{5-9}$$

$$R = \frac{r}{R_L} \qquad \textbf{5-10}$$

The dimensionless time, τ, is expressed as a ratio of viscous to inertial forces:

$$\tau = \frac{\mu t}{\rho R_L^2} \qquad \textbf{5-11}$$

where ρ is the density of the fluid in the lumen, and t is the time. The dimensionless permeability:

$$\kappa = \frac{L\left(\frac{1}{k_m} + \frac{1}{k_g}\right)^{-1}}{R_L^2 (d_w + d_g)} \qquad \textbf{5-12}$$

where k_m is the membrane hydraulic permeability, k_g is the permeability of the gel layer, d_w and d_g is the membrane wall and gel thickness respectively (pore fouling will not be considered); and

$$b = \frac{4\rho g_z L}{(p_0 - p_1)} \qquad \textbf{5-13}$$

where g_z is gravitational acceleration.

5.4 Boundary and initial conditions

The boundary and initial conditions which match the imposed operating conditions, and necessary to solve the differential equations which arise in the modelling of the system are presented in Table 5-1. In the far left column of the table are the boundary conditions (B.C.), the initial condition (I.C.), and steady-state condition (S.S.C.). The second and third columns from left give the values of the independent and corresponding dependent variables, respectively.

Table 5-1: The boundary, initial and steady-state conditions of the SFCMBR

I.C./B.C./S.S.C.	**τ, R, Z**	**U_L, U_S, V_L, V_S, P_L, P_S**	**Range**	**Equation**
I.C.	$\tau = \tau_0$	$U = U_\tau = U_\infty$	$0 \le R \le 1$, $0 \le Z \le 1$	**5-14a**
S.S.C	$\tau \ge \tau_\infty$	$\frac{\partial U}{\partial \tau} = U_\tau = 0$	$0 \le R \le 1$, $0 \le Z \le 1$	**5-14b**
B.C.1	$R = 0$	U = finite	$0 \le Z \le 1$	**5-14c**
B.C.2	$R = 1$	$U = 0$	$0 \le Z \le 1$	**5-14d**
B.C.3	$R = 0$	$\frac{\partial U}{\partial R} = 0$	$0 \le Z \le 1$	**5-14e**
B.C.4	$R = 0$	$V = 0$	$0 \le Z \le 1$	**5-14f**
B.C.5	$R = 1$	$V = V_M$	$\tau = \infty$	**5-14g**
B.C.6	$Z = 0$	$P_L = P_L(0)$, $P_L' = a$	$0 \le R \le 1$	**5-14h**
B.C.7	$Z = 0$	$U_S = 0$, $P_S = P_{S(0)}$	$0 \le R \le 1$	**5-14i**
B.C.8	$R = R_2$	$\frac{\partial U_S}{\partial R} = 0$	$0 \le Z \le 1$	**5-14j**
B.C.9	$R = R_3$	$U_S = 0$	$0 \le Z \le 1$	**5-14k**
B.C.10	$R = R_2$	$V_S = 0$	$0 \le Z \le 1$	**5-14l**
B.C.11	$R = R_x$	$V_M = V_S$	$0 \le Z \le 1$	**5-14m**
B.C.12	$R = R_2$	U_S = finite	$0 \le Z \le 1$	**5-14n**

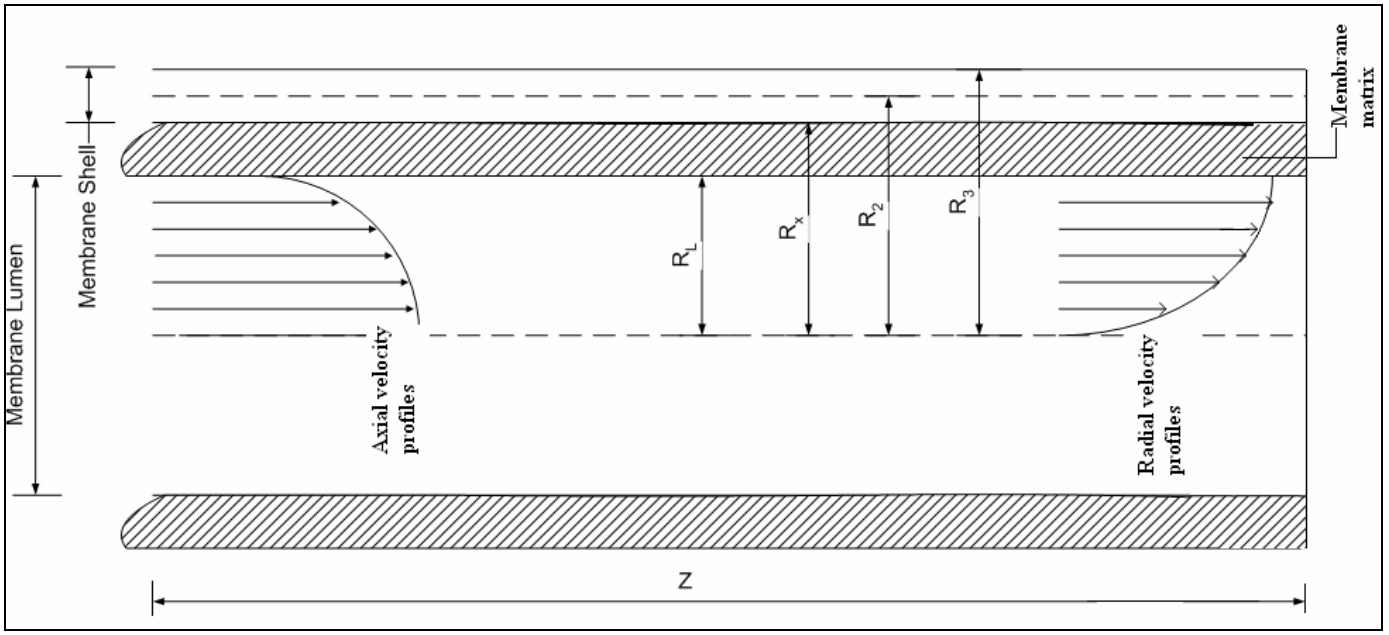

Figure 5-2: Hypothesised velocity distributions through the PSu capillary membrane

Figure 5-2 is a representation of the hypothesised flow through the PSu capillary membrane, dictated by the boundary conditions specified by Equations 5-14a to 5-14n. Strictly speaking, the well known Beavers and Joseph condition should be used instead of the boundary condition given by Equation 5-14d. The Beavers and Joseph condition may be written as (Elshahed, 2004):

$$\phi \frac{dU}{dR} + U = 0 \quad at \quad R = 1 \qquad \textbf{5-15}$$

where ϕ is the slip coefficient. However, according to Catapano *et al.* (1990), the distortion of the velocity profile relative to that established in non-porous wall systems is measured by the parameter χL, where:

$$\chi = 4\sqrt{\mu k_m / R_L^3} \qquad \textbf{5-16}$$

In Equation 5-16 χ is in m^{-1} and k_m is in m/Pas, and if the value of χL is less than unity, the distortion of the velocity profile induced by the porous wall is negligible. This means the boundary condition given by Equation 5-14d is valid for bioreactor systems where χL is less than unity, as is the case for the current bioreactor system (χL = 0.02). The velocity profiles in Figure 5-2 are for fully developed, axisymmetric, laminar flow, through a porous media.

5.5 Analytical model solutions

5.5.1 The generic equation

The dimensionless form of Equation 3-1 when ignoring the inertial terms (a valid assumption only for operations with small Re_w) is:

$$\frac{\partial U_L}{\partial \tau} = \frac{1}{R}\frac{\partial}{\partial R}\left(R\frac{\partial U_L}{\partial R}\right) + \frac{1}{R^2}\frac{\partial^2 U_L}{\partial \theta^2} - \left(\frac{\partial P_L}{\partial Z} - b\right) \qquad \textbf{5-17}$$

If the solution of Equation 5-17 is assumed to be of the form:

$$U_L(R,\theta,\tau) = \Xi(R)\Theta(\theta)\mathrm{K}(\tau) \qquad \textbf{5-18}$$

and the following assumptions are made regarding the functions Θ and K:

$$\frac{\partial^2 \Theta}{\partial \theta^2} = -m^2\Theta \qquad \textbf{5-19}$$

$$\frac{\partial \mathrm{K}}{\partial \tau} = -\alpha^2 \mathrm{K} \qquad \textbf{5-20}$$

then Equation 5-17 may be written as a generic equation of the form:

$$R^2\frac{d^2\Xi}{dR^2} + R\frac{d\Xi}{dR} + \left(\alpha^2 R^2 - m^2\right)\Xi = f(Z,\theta,\tau) \qquad \textbf{5-21}$$

where:

$$f(Z,\theta,\tau) = \frac{e^{-\alpha^2\tau}R^2 G}{(A_1\cos m\theta + A_2 \sin m\theta)B_0}, \qquad B_0 \neq 0 \qquad \textbf{5-22}$$

and

$$G = \left(\frac{\partial P_L}{\partial Z} - b\right) \qquad \textbf{5-23}$$

Table 5-2: Generic equation of flows with a low Re_w through cylindrical surfaces

α	m	$f(Z,\theta,\tau)$	**Resulting equation**
> 0	≥ 0	= 0	Bessel's equation
= 0	> 0	> 0	Poisson's equation
= 0	> 0	= 0	Laplace's equation

Equation 5-21 may be thought of as a generic equation for small Re_w flows through cylindrical surfaces, because under the conditions specified in Table 5-2 it reduces to the familiar and extensively studied equations listed in the table, which arise frequently in studies of flow behaviour. The complete derivation of Equation 5-21 is given in Appendix A.

5.5.2 Vertical orientation (constant shell side pressure)

The solutions presented in this section assume $m = 0$ to be the applicable condition in solving Equation 5-21, and are only applicable to a system with a constant shell side hydrostatic pressure. The independence of the function Ξ on Θ (i.e. $m = 0$) corresponds to the assumption of circular symmetry about the z-axis of the capillary membranes used. Only the resulting mathematical expressions are presented, the complete analysis is given in Appendix A. The dimensionless axial velocity profile in the lumen side, U_L, is therefore given by:

$$U_L = -\frac{1}{4}\left[\left(1-R^2\right)-8\sum_{n=1}^{\infty}\frac{J_0\left(\alpha_n R\right)}{\alpha_n^3 J_1\left(\alpha_n\right)}e^{-\alpha_n^2\tau}\right]\left(\frac{dP_L}{dZ}-b\right) \qquad \textbf{5-24}$$

where α_n is the nth root of the Bessel function $J_n(\alpha_n R)$. The dimensionless radial velocity in the lumen side, V_L, is:

$$V_L = \frac{1}{4}\left[\frac{R}{2}\left(1-\frac{R^2}{2}\right)-8\sum_{n=1}^{\infty}\frac{J_1\left(\alpha_n R\right)}{\alpha_n^4 J_1\left(\alpha_n\right)}e^{-\alpha_n^2\tau}\right]\frac{d^2P_L}{dZ^2} \qquad \textbf{5-25}$$

the dimensionless lumenal flowrate, Ω_L, is given by:

$$\Omega_L = -\left(\frac{1}{4}-8\sum_{n=1}^{\infty}\frac{e^{-\alpha_n^2\tau}}{\alpha_n^4}\right)\left(\frac{dP_L}{dZ}-b\right) \qquad \textbf{5-26}$$

the dimensionless velocity profile through the matrix, V_M, is:

$$V_M = -\kappa\left[P_{Sb\pi}-P_L\right] \qquad \textbf{5-27}$$

the dimensionless axial velocity profile in the shell U_S is:

$$U_S = \frac{b}{4}\left\{\left[2R_2^2\ln\frac{R}{R_3}+R_3^2-R^2\right]-4\sum_{n=1}^{\infty}B_n e^{-\alpha_n^2\tau}J_0\left(\alpha_n R\right)\right\} \qquad \textbf{5-28}$$

where:

$$B_n = -\frac{2}{J_1^2(\alpha_n)}\left\{\frac{R_2^2}{2}\left(\frac{1}{2}\ln R_3 + \frac{1}{4}\right)J_0(\alpha_n) + \frac{R_2^2}{4\alpha_n^2}\left[\alpha_n\left(\frac{1}{2\Gamma(2)} - J_1(\alpha_n)\right) + \left(\ln R_3 + \frac{1}{2}\right)J_2(\alpha_n)\right] - \frac{J_1(\alpha_n)}{\alpha_n^3}\right\}$$

5-29

there is no radial shell velocity for the constant shell pressure SFCMBR (i.e., $V_S = 0$), and the dimensionless shell volumetric flowrate, Ω_S, is given by:

$$\Omega_S = -b\left\{\left[R_2^2\left(\ln R_3 + \frac{1}{2}\right) - \frac{R_3^2}{2} + \frac{1}{4}\right] + \frac{4}{\alpha_n b}\sum_{n=1}^{\infty} B_n e^{-\alpha_n^2\tau} J_1(\alpha_n)\right\}$$

5-30

the dimensionless pressure profile inside the lumen of the membrane bioreactor is given by:

$$P_L(Z) = (P_0 - P_{Sb\pi})\cosh\left(4\sqrt{\kappa}\right)Z + \frac{a}{4\sqrt{\kappa}}\sinh\left(4\sqrt{\kappa}\right)Z + P_{Sb\pi}$$

5-31

where:

$$a = \frac{4\sqrt{\kappa}(P_0 - P_{Sb\pi})\sinh\left(4\sqrt{\kappa}\right)}{\left[f - \cosh\left(4\sqrt{\kappa}\right)\right]} - \frac{b(1-f)}{\left[f - \cosh\left(4\sqrt{\kappa}\right)\right]}$$

5-32

$$P_{Sb\pi} = P_S + \Pi - \left(\frac{d_w + d_g}{L}\right)b$$

5-33

From the definition of a stream function in Section 3.2.2, the equation for the stream function in the lumen side of the membrane is given by:

$$\psi_L(R,Z,\tau) = \frac{1}{4}\left\{\left[\frac{1}{2} - 8\sum_{n=1}^{\infty}\frac{e^{-\alpha_n^2\tau}}{\alpha_n^4}\right]\left(\frac{dP_L}{dZ} - b\right) + \left[\frac{R^2}{2}\left(1 - \frac{R^2}{2}\right) - 8\sum_{n=1}^{\infty}\frac{RJ_1(\alpha_n R)e^{-\alpha_n^2\tau}}{\alpha_n^4 J_1(\alpha_n)}\right]\left(\frac{dP_{L(1)}}{dZ} - \frac{dP_{L(0)}}{dZ}\right)\right\}$$

5-34

At steady state (i.e., at $\tau = \tau_\infty$), Equation 5-34 reduces to:

$$\psi_L = \frac{1}{4}\left\{\frac{1}{2}\left(\frac{dP_L}{dZ} - b\right) + \left[\frac{R^2}{2}\left(1 - \frac{R^2}{2}\right)\right]\left(\frac{dP_{L(1)}}{dZ} - \frac{dP_{L(0)}}{dZ}\right)\right\}$$

5-35

the stream function in the shell side of the membrane is given by:

$$\psi_S = -b\left\{\frac{R_2^2}{4}\left[\ln(R_3 - R_2) - \ln R_3\right]\left(R_3^2 - R_2^2\right) - \frac{R_2^2}{8}\left(R_3^2 - R_2^2\right) + \frac{R_3^2}{8}\left(R_3^2 - R_2^2\right) - \frac{\left(R_3^4 - R_2^4\right)}{16}\right\}$$

5-36

5.5.3 Vertical orientation (variable shell side pressure)

The solutions presented in this section are applicable to a system with a shell side hydrostatic pressure that is a function of the axial position. The axial and radial velocity profiles as well as the volumetric flowrate in the lumen side are still governed by the same expressions as for a constant shell side pressure SFCMBR:

$$U_L = -\frac{1}{4}\left[\left(1-R^2\right)-8\sum_{n=1}^{\infty}\frac{J_0\left(\alpha_n R\right)}{\alpha_n^3 J_1\left(\alpha_n\right)}e^{-\alpha_n^2\tau}\right]\left(\frac{dP_L}{dZ}-b\right) \quad \textbf{5-24}$$

$$V_L = \frac{1}{4}\left[\frac{R}{2}\left(1-\frac{R^2}{2}\right)-8\sum_{n=1}^{\infty}\frac{J_1\left(\alpha_n R\right)}{\alpha_n^4 J_1\left(\alpha_n\right)}e^{-\alpha_n^2\tau}\right]\frac{d^2P_L}{dZ^2} \quad \textbf{5-25}$$

$$\Omega_L = -\left(\frac{1}{4}-8\sum_{n=1}^{\infty}\frac{e^{-\alpha_n^2\tau}}{\alpha_n^4}\right)\left(\frac{dP_L}{dZ}-b\right) \quad \textbf{5-26}$$

the axial and radial velocity profiles in the shell U_S and V_S are governed by respectively:

$$U_S = -\frac{1}{4}\left\{\left[2R_2^2\ln\frac{R}{R_3}+R_3^2-R^2\right]-4\sum_{n=1}^{\infty}B_n e^{-\alpha_n^2\tau}J_0\left(\alpha_n R\right)\right\}\left(\frac{dP_S}{dZ}-b\right) \quad \textbf{5-37}$$

$$V_S = \frac{1}{16R}\left[R_2^4-R^4-2R_3^2\left(R_2^2-R^2\right)-8R_2^2\left[\left(\frac{R_2^2}{2}\ln\frac{R_2}{R_3}-\frac{R_2^2}{4}\right)-\left(\frac{R^2}{2}\ln\frac{R}{R_3}-\frac{R^2}{4}\right)\right]\right]\frac{d^2P_S}{dZ^2} \quad \textbf{5-38}$$

the dimensionless shell volumetric flowrate, Ω_S, is given by:

$$\Omega_S = \left\{\left[R_2^2\left(\ln R_3+\frac{1}{2}\right)-\frac{R_3^2}{2}+\frac{1}{4}\right]+\frac{4}{\alpha_n b}\sum_{n=1}^{\infty}B_n e^{-\alpha_n^2\tau}J_1\left(\alpha_n\right)\right\}\left(\frac{dP_S}{dZ}-b\right) \quad \textbf{5-39}$$

The hydrostatic pressure profile in the shell is given by:

$$P_S = \frac{AR_x\cosh\omega Z}{\omega^2 f\left(R_x\right)}+\frac{BR_x\sinh\omega Z}{\omega^3 f\left(R_x\right)}+H_g Z+D \quad \textbf{5-40}$$

the corresponding lumenal pressure profile is:

$$P_L = \frac{A\cosh\omega Z}{\omega^2}+\frac{B\sinh\omega Z}{\omega^3}+H_g Z+D \quad \textbf{5-41}$$

where:

$$\omega^2 = 16\kappa\left(\frac{f(R_x)-R_x}{f(R_x)}\right) \quad \textbf{5-42}$$

$$f(R_x)=\left[R_2^4 - R_x^4 - 2R_3^2\left(R_2^2 - R_x^2\right) - 8R_2^2\left[\left(\frac{R_2^2}{2}\ln\frac{R_2}{R_3} - \frac{R_2^2}{4}\right) - \left(\frac{R_x^2}{2}\ln\frac{R_x}{R_3} - \frac{R_x^2}{4}\right)\right]\right] \quad \textbf{5-43}$$

$$A = \frac{\omega^2 f(R_x)\left(P_{L(0)} - P_{S(0)}\right)}{\left[f(R_x)-R_x\right]} \quad \textbf{5-44}$$

$$B = \frac{\omega^3 f(R_x)^2\left(P_{L(0)} - P_{S(0)}\right)\sinh\omega}{\left[f(R_x)-R_x\right]\left[f(R_x)(f-\cosh\omega)+R_x(f-1)\right]} \quad \textbf{5-45}$$

$$D = P_{L(0)} - \frac{f(R_x)\left(P_{L(0)} - P_{S(0)}\right)}{\left[f(R_x)-R_x\right]} \quad \textbf{5-46}$$

$$H_g = b + \frac{\omega R_x f(R_x)\left(P_{L(0)} - P_{S(0)}\right)\sinh\omega}{\left[f(R_x)-R_x\right]\left[f(R_x)(f-\cosh\omega)+R_x(f-1)\right]} \quad \textbf{5-47}$$

the stream function in the lumen side of the membrane is still governed by the same expressions as for a constant shell side pressure SFCMBR:

$$\psi_L = \frac{1}{4}\left\{\frac{1}{2}\left(\frac{dP_L}{dZ} - b\right) + \left[\frac{R^2}{2}\left(1 - \frac{R^2}{2}\right)\right]\left(\frac{dP_{L(1)}}{dZ} - \frac{dP_{L(0)}}{dZ}\right)\right\} \quad \textbf{5-35}$$

the stream function in the shell side of the membrane is given by:

$$\psi_S = \frac{1}{16}\left\{R_2^4 - R^4 - 2R_3^2\left(R_2^2 - R^2\right) - 8R_2^2\left[\left(\frac{R_2^2}{2}\ln\frac{R_2}{R_3} - \frac{R_2^2}{4}\right) - \left(\frac{R^2}{2}\ln\frac{R}{R_3} - \frac{R^2}{4}\right)\right]\right\}\left(\frac{dP_{S(1)}}{dZ} - \frac{dP_{S(0)}}{dZ}\right)$$
$$+\left(\frac{dP_S}{dZ} - b\right)\varpi$$

5-48

where:

$$\varpi = \frac{R_2^2}{4}\left[\ln(R_3 - R_2) - \ln R_3\right]\left(R_3^2 - R_2^2\right) - \frac{R_2^2}{8}\left(R_3^2 - R_2^2\right) + \frac{R_3^2}{8}\left(R_3^2 - R_2^2\right) - \frac{\left(R_3^4 - R_2^4\right)}{16} \quad \textbf{5-49}$$

5.5.4 Horizontal orientation (constant shell side pressure)

For the horizontally orientated SFCMBR with a constant shell side pressure it is assumed that gravitational acceleration effects will be negligible (i.e. $b = 0$) as compared to other forces. The resulting mathematical expressions then become, for the dimensionless axial velocity profile U_L in the lumen side:

$$U_L = -\frac{1}{4}\left[\left(1-R^2\right)-8\sum_{n=1}^{\infty}\frac{J_0\left(\alpha_n R\right)}{\alpha_n^3 J_1\left(\alpha_n\right)}e^{-\alpha_n^2\tau}\right]\frac{dP_L}{dZ} \qquad \textbf{5-50}$$

the radial velocity profile in the lumen side V_L is the same as in the vertically orientated SFCMBR:

$$V_L = \frac{1}{4}\left[\frac{R}{2}\left(1-\frac{R^2}{2}\right)-8\sum_{n=1}^{\infty}\frac{J_1\left(\alpha_n R\right)}{\alpha_n^4 J_1\left(\alpha_n\right)}e^{-\alpha_n^2\tau}\right]\frac{d^2P_L}{dZ^2} \qquad \textbf{5-25}$$

the velocity profile through the matrix V_M is

$$V_M = -\kappa\left[P_{S\pi} - P_L\right] \qquad \textbf{5-51}$$

there is no radial or axial shell flow for the constant shell pressure horizontal SFCMBR (i.e., $V_S = U_S = 0$). The dimensionless lumenal flowrate, Ω_L, is given by:

$$\Omega_L = -\left(\frac{1}{4}-8\sum_{n=1}^{\infty}\frac{e^{-\alpha_n^2\tau}}{\alpha_n^4}\right)\frac{dP_L}{dZ} \qquad \textbf{5-52}$$

and the pressure profile inside the lumen of the membrane bioreactor is given by:

$$P_L(Z) = \left(P_0 - P_{S\pi}\right)\cosh\left(4\sqrt{\kappa}\right)Z + \frac{a}{4\sqrt{\kappa}}\sinh\left(4\sqrt{\kappa}\right)Z + P_{S\pi} \qquad \textbf{5-53}$$

where:

$$a = \frac{4\sqrt{\kappa}\left(P_0 - P_{S\pi}\right)\sinh\left(4\sqrt{\kappa}\right)}{\left[f - \cosh\left(4\sqrt{\kappa}\right)\right]} \qquad \textbf{5-54}$$

$$P_{S\pi} = P_S + \Pi \qquad \textbf{5-55}$$

5.5.5 Horizontal orientation (variable shell side pressure)

The treatment is exactly the same as for the vertical SFCMBR with variable shell side pressure, neglecting the gravitational acceleration terms. The axial and radial velocity profiles in the lumen side are still governed by the same expressions as for a horizontal constant shell side pressure SFCMBR:

$$U_L = -\frac{1}{4}\left[\left(1-R^2\right)-8\sum_{n=1}^{\infty}\frac{J_0\left(\alpha_n R\right)}{\alpha_n^3 J_1\left(\alpha_n\right)}e^{-\alpha_n^2\tau}\right]\frac{dP_L}{dZ} \qquad \textbf{5-50}$$

$$V_L = \frac{1}{4}\left[\frac{R}{2}\left(1-\frac{R^2}{2}\right)-8\sum_{n=1}^{\infty}\frac{J_1\left(\alpha_n R\right)}{\alpha_n^4 J_1\left(\alpha_n\right)}e^{-\alpha_n^2\tau}\right]\frac{d^2P_L}{dZ^2} \qquad \textbf{5-25}$$

the shell side radial velocity profile U_S is given by:

$$U_S = -\frac{1}{4}\left\{\left[2R_2^2\ln\frac{R}{R_3}+R_3^2-R^2\right]-4\sum_{n=1}^{\infty}B_n e^{-\alpha_n^2\tau}J_0\left(\alpha_n R\right)\right\}\frac{dP_S}{dZ} \qquad \textbf{5-56}$$

the radial velocity profile on the shell side V_S is given by:

$$V_S = \frac{1}{16R}\left[R_2^4-R^4-2R_3^2\left(R_2^2-R^2\right)-8R_2^2\left[\left(\frac{R_2^2}{2}\ln\frac{R_2}{R_3}-\frac{R_2^2}{4}\right)-\left(\frac{R^2}{2}\ln\frac{R}{R_3}-\frac{R^2}{4}\right)\right]\right]\frac{d^2P_S}{dZ^2} \qquad \textbf{5-38}$$

and the pressure profile on the shell side P_S is:

$$P_S = \frac{AR_x\cosh\omega Z}{\omega^2 f\left(R_x\right)}+\frac{BR_x\sinh\omega Z}{\omega^3 f\left(R_x\right)}+HZ+D \qquad \textbf{5-57}$$

the corresponding lumenal pressure profile will be given by:

$$P_L = \frac{A\cosh\omega Z}{\omega^2}+\frac{B\sinh\omega Z}{\omega^3}+HZ+D \qquad \textbf{5-58}$$

where the constants A, B, and D are the same as in the vertically orientated SFCMBR, and H is given by:

$$H = \frac{\omega R_x f\left(R_x\right)\left(P_{L(0)}-P_{S(0)}\right)\sinh\omega}{\left[f\left(R_x\right)-R_x\right]\left[f\left(R_x\right)\left(f-\cosh\omega\right)+R_x\left(f-1\right)\right]} \qquad \textbf{5-59}$$

5.6 Finite difference scheme formulation

The numerical solutions of the two-dimensional Navier-Stokes equations were obtained by finite differencing the dimensionless partial differential equations as shown in Table 5-3. The complete analysis is given in Appendix B. These solutions are restricted to luminal flows only.

Table 5-3: Discretization of the dimensionless Navier-Stokes equations

Differential	Discretization	Type
$\frac{\partial U}{\partial \tau}$	$\frac{U_{i,j}^{n+1} - U_{i,j}^{n}}{\Delta \tau}$	Forward difference
$\frac{\partial U}{\partial R}$	$\frac{U_{i,j+1}^{n} - U_{i,j-1}^{n}}{2\Delta R}$	Central difference
$\frac{\partial U}{\partial Z}$	$\frac{U_{i+1,j}^{n} - U_{i-1,j}^{n}}{2\Delta Z}$	Central difference
$\frac{\partial^2 U}{\partial Z^2}$	$\frac{U_{i+1,j}^{n} - 2U_{i,j}^{n} + U_{i-1,j}^{n}}{\Delta Z^2}$	Central difference
$\frac{\partial^2 V}{\partial R^2}$	$\frac{V_{i,j+1}^{n} - 2V_{i,j}^{n} + V_{i,j-1}^{n}}{\Delta R^2}$	Central difference
$\frac{\partial P}{\partial Z}$	$\frac{P_{i+1,j}^{n} - P_{i,j}^{n}}{\Delta Z}$	Forward difference
$\frac{\partial P}{\partial R}$	$\frac{P_{i,j+1}^{n} - P_{i,j}^{n}}{\Delta R}$	Forward difference

The dimensionless form of the *z*-component of the Navier-Stokes equations, in cylindrical form, is given by the following:

$$\frac{\partial U}{\partial \tau} + \mathrm{Re}_b \left(V \frac{\partial U}{\partial R} + \beta U \frac{\partial U}{\partial Z} \right) = \frac{1}{R} \frac{\partial}{\partial R} \left(R \frac{\partial U}{\partial R} \right) + \beta^2 \frac{\partial^2 U}{\partial Z^2} - \beta \frac{\partial P}{\partial Z} + b \qquad \textbf{5-60}$$

and the dimensionless *r*-component is:

$$\frac{\partial V}{\partial \tau} + \mathrm{Re}_b \left(V \frac{\partial V}{\partial R} + \beta U \frac{\partial V}{\partial Z} \right) = \frac{1}{R} \frac{\partial}{\partial R} \left(R \frac{\partial V}{\partial R} \right) - \frac{V}{R^2} + \beta^2 \frac{\partial^2 V}{\partial Z^2} - \frac{\partial P}{\partial R} \qquad \textbf{5-61}$$

where Re_b is the bulk fluid Reynolds number, which is different from the wall Reynolds number (Re_w) that is calculated using the wall velocity. Re_b is defined as:

$$\mathrm{Re}_b = \frac{\rho v_{z0} R_L}{\mu} \qquad \textbf{5-62}$$

and β is the aspect ratio defined as:

$$\beta = \frac{R_L}{L} \qquad \textbf{5-63}$$

The corresponding axial and radial finite difference equations are, respectively:

$$\frac{U_{i,j}^{n+1} - U_{i,j}^{n}}{\Delta\tau} + N_{\mathrm{Re}}\left(V_{i,j}^{n} \frac{U_{i,j+1}^{n} - U_{i,j-1}^{n}}{2\Delta R} + \beta U_{i,j}^{n} \frac{U_{i+1,j}^{n} - U_{i-1,j}^{n}}{2\Delta Z} \right) = \frac{1}{R} \frac{U_{i,j+1}^{n} - U_{i,j-1}^{n}}{2\Delta R}$$
$$+ \frac{U_{i,j+1}^{n} - 2U_{i,j}^{n} + U_{i,j-1}^{n}}{\Delta R^2} + \beta^2 \frac{U_{i+1,j}^{n} - 2U_{i,j}^{n} + U_{i-1,j}^{n}}{\Delta Z^2} - \beta \frac{P_{i+1,j}^{n} - P_{i,j}^{n}}{\Delta Z} + b$$

5-64

and

$$\frac{V_{i,j}^{n+1} - V_{i,j}^{n}}{\Delta\tau} + N_{\mathrm{Re}}\left(V_{i,j}^{n} \frac{V_{i,j+1}^{n} - V_{i,j-1}^{n}}{2\Delta R} + \beta U_{i,j}^{n} \frac{V_{i+1,j}^{n} - V_{i-1,j}^{n}}{2\Delta Z} \right) = \frac{1}{R} \frac{V_{i,j+1}^{n} - V_{i,j-1}^{n}}{2\Delta R} + \frac{V_{i,j+1}^{n} - 2V_{i,j}^{n} + V_{i,j-1}^{n}}{\Delta R^2}$$
$$- \frac{V_{i,j}^{n}}{R^2} + \beta^2 \frac{V_{i+1,j}^{n} - 2V_{i,j}^{n} + V_{i-1,j}^{n}}{\Delta Z^2} - \frac{P_{i,j+1}^{n} - P_{i,j}^{n}}{\Delta R}$$

5-65

Equations 5-64 and 5-65 were solved using a revised form of the semi-implicit method for pressure-linked equations (SIMPLE). The procedure for the SIMPLE algorithm is as follows (Anderson, 1995):

1. Start the iterative process by guessing the pressure field. Denote the guessed pressures as $(P^*)^n$.
2. Use the values of $(P^*)^n$ to solve for U^n and V^n from the momentum equations. Since these values are those associated with the values of $(P^*)^n$, denote them by $(U^*)^n$ and $(V^*)^n$.
3. Since the values of $(U^*)^n$ and $(V^*)^n$ were obtained from guessed values of $(P^*)^n$, they will not necessarily satisfy the continuity equation. Hence, using the continuity equation, construct a pressure correction $(P')^n$ which when added to $(P^*)^n$ will bring the velocity

field more into agreement with the continuity equation. That is, the corrected pressure P^n is given by

$$P^n = \left(P^*\right)^n + \left(P'\right)^n \qquad \textbf{5-66}$$

4. Designate the new value of P^n in Equation 5-66 as the new value of $(P^*)^n$. Return to step 2 and repeat the process until a velocity field which satisfies the continuity equation is obtained.

In this study, the SIMPLE algorithm was simplified by using the expressions obtained from the analytical solution (Equation 5-31, 5-40, 5-41, 5-53, 5-57, and 5-58) to develop the pressure field in step 1. The pressure profile was assumed to exhibit an exponential decay with time to a steady-state value. The velocity profiles obtained from this pressure field satisfy the continuity equation.

6. MATERIALS AND METHODS

6.1 Introduction

This chapter provides a description of the materials and methods that were used to validate the proposed theoretical models that were developed in Chapter 5. Only a summary of the procedures that were used to prepare the reagents and the fungus will be given. A complete description of the growth and maintenance of the fungus and the preparation of the nutrient solution is given in Appendix C and D, respectively. The experimental procedure that were followed to cultivate *P. chrysosporium* for continuous enzyme production, in a single fibre capillary membrane bioreactor (SFCMBR), was previously explained by Leukes (1999), Garcin (2000), Solomon (2001), Ntwampe (2005), and Sheldon and Small (2005).

6.2 Description of materials

6.2.1 Microorganism

The WRF, *P. chrysosporium* strain BKM-F-1767 (ATCC 24725), was used in all the experiments. Cultures of the fungus were maintained on supplemented malt agar slants, and were grown on petri plates containing growth medium at 37ºC, according to Tien and Kirk (1988). The resulting mycelia was homogenised with sterile distilled water, to form a spore-mycelia mixture, which was then filtered to obtain a pure spore solution (see Appendix C: C1 - C5). The pure spore solution was freeze-dried to a temperature of -70ºC and stored at 4ºC. For an experimental run the freeze-dried spores were homogenised, with sterile distilled water, to make up the required spore solution concentration. For each biofilm growth experimental run 3×10^6 spores were prepared (see Appendix C: C6) and inoculated onto the external skin of the capillary polysulphone membrane using reverse filtration as described in Govender *et al.* (2004).

6.2.2 Nutrient medium

A nutrient medium was used to provide the fungus with low-molecular mass nutrient sources, like carbon and nitrogen, and was also the standard medium as described by Tien and Kirk (1988). The nutrient medium contained (in 1 liter): 100ml Basal medium, 100ml of 10% glucose

stock solution, 100ml of 0.1M 2,2-dimethylsuccinate, 10ml thiamin, 25ml ammonium tartrate, 100ml of 0.02M veratryl alcohol, 60ml trace elements, and 505ml of sterile distilled water (see Appendix D). The nutrient medium was supplied through the membrane lumen to the fungus, immobilized on the external skin of the capillary membrane, at a flow rate of 6.20ml/hr using a Watson Marlow 505S perilstatic pump (Dune Engineering, RSA).

6.2.3 Polysulphone capillary membrane

The capillary PSu membrane bioreactor that was used in this study was described by Jacobs and Leukes (1996); Leukes (1999); Solomon (2001); Sheldon and Small (2005). It consisted of a single capillary, made of surface modified polysulphone, encased in a glass bioreactor. The PSu capillary membranes were produced and supplied by the Institute of Polymer Science at the University of Stellenbosch (RSA). The membranes are characterized by an internally skinned and externally un-skinned region of microvoids, approximately 0.15mm long and 0.015mm thick, as shown in Figure 2-2. These membranes have inner diameters of approximately 1.395mm and outer diameters of 1.925mm.

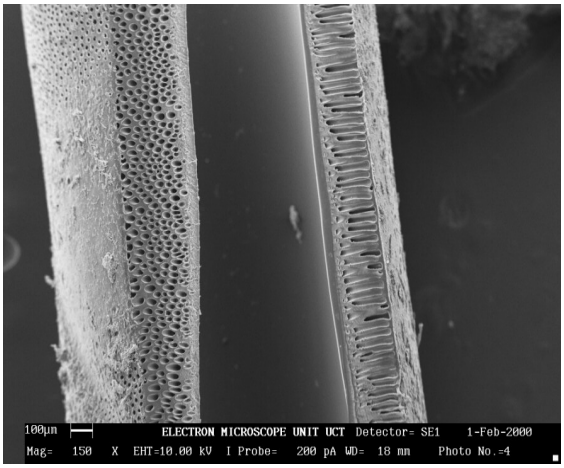

Figure 2-2:A scanning electron microscope image of the PSu capillary membrane (Solomon & Petersen, 2002)

6.2.4 Air pump

A Hailea ACO 9220 diaphragm air pump was used to supply the shell of the SFCMBR with a consistent throughput of humidified air at 240 L/hr. The air supplied by the pump was filter-sterilised, using a 0.22µm Cameo filter, before being fed to the humidifier.

6.2.5 Humidifier

A 500ml Schott bottle, half-filled with sterile distilled water, was used as a humidifier. The humidifier was connected to the SFCMBR and the diaphragm air pump by silicone tubing (ID = 3cm; OD = 5cm). The air from the diaphragm pump was first filter-sterilised and humidified before being fed to the shell side of the SFCMBR.

6.2.6 Pressure transducers

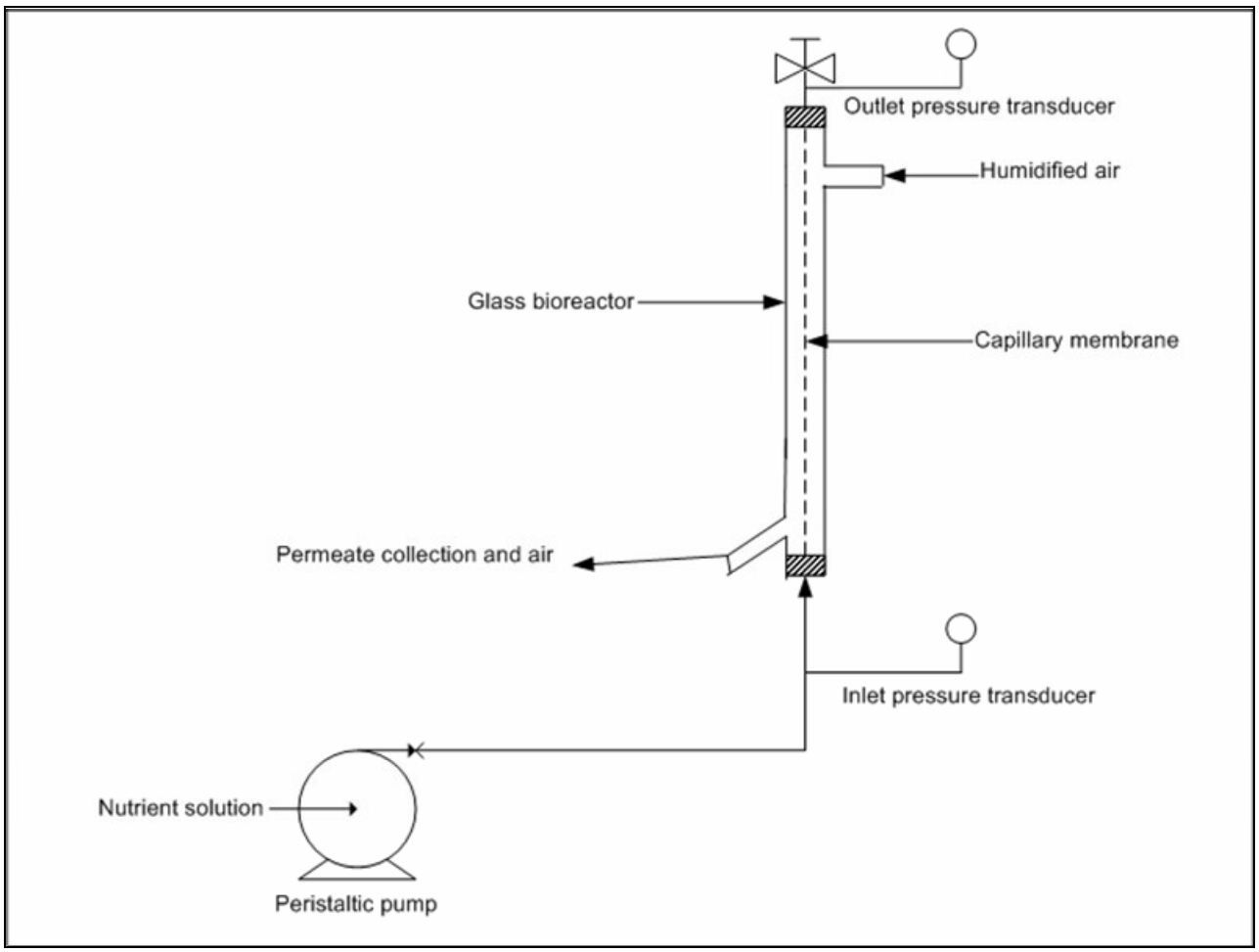

Figure 6-1: A schematic diagram of the single fibre capillary membrane bioreactor (SFCMBR)

The SFCMBR was fitted with two Vega (United Kingdom) pressure transducers (model: BAR14.X1CA1GV1), which were connected to a computer for online pressure readings. The two pressure transducers were connected at the inlet and outlet of the SFCMBR, as shown in Figure 6-1. LabView®, a data acquisition programme developed by National Instruments, was utilised

for acquiring, transforming and displaying the data from the pressure transducers. The transmembrane pressure (TMP) was calculated by:

$$p_{TMP} = \left(\frac{p_0 + p_1}{2} \right) - p_S \qquad \textbf{3-15}$$

The shell side pressure of the SFCMBR, p_S, was at atmospheric pressure (101.325 kPa) for both the control and biofilm growth experiments.

6.3 Description of experiments

6.3.1 Control experiments

Before performing the biofilm growth experimental runs, experiments with no biofilm growth were undertaken to serve as a control. The control experiments also involved validation of the properties of both the nutrient solution and PSu capillary membrane.

Table 6-1: The dimensions of the single fibre capillary membrane bioreactor

Membrane inner radius	R_L	m	6.63×10^{-04}
Membrane outer radius	r_x	m	9.10×10^{-04}
Extra capillary space radius	r_2	m	5.91×10^{-03}
Glass manifold inner radius	r_3	m	10.91×10^{-03}
Effective membrane length	L	m	0.29

The dimensions of the SFCMBR are indicated in Table 6-1. The PSu capillary membrane, described in Section 6.2.3, was fixed to the centre of the glass reactor using epoxy glue, one side at a time, and left over night to dry. For the control runs, it was not necessary to autoclave the tubing and the distilled water that was used. Silicone tubing (ID = 3cm; OD = 5cm) was used to feed the bioreactor with distilled water. The one end of the bioreactor was clamped, to force the distilled water through the membrane (i.e. dead-end filtration). The tubing to and from the bioreactor was fitted with a splitter to allow pressure transducers to be connected, as shown in Figure 6-1. Distilled water was pumped at varying flowrates (refer to Section 6.3.4) from a 500ml bottle to the bioreactor using a Watson Marlow 505S peristaltic pump. The system was allowed to run for about an hour for all the tubing to be filled with water, before the inlet and outlet pressure readings were taken. Pressure readings were taken until the system reached steady-state.

The inlet and outlet pressure readings were used in the developed models to firstly validate the accuracy of the developed model, and secondly, to predict various model parameters such as membrane hydraulic permeability; the pressure and velocity profiles along the length of the membrane.

6.3.2 Biofilm growth experiments

When carrying out the biofilm growth experiments precautionary sterilisation measures had to be taken in all the preparation steps, to prevent contamination. It was important that the membranes were handled gently and with the minimum amount of distortion. All the tubing, glassware and bioreactors that were used were autoclaved for 20min at 120 ºC. A 4% formaldehyde solution was used to chemically sterilize the lumen side of the capillary membranes. The formaldehyde solution was run for 6 hours through the system, and thereafter the bioreactor was rinsed with autoclaved distilled water for 12hr to remove all the traces of formaldehyde.

Figure 6-2: A pictorial view of the single-fibre capillary membrane bioreactor (SFCMBR)

After the sterilization and rinsing process, the membrane was inoculated with 3.0×10^6 *P. chrysosporium* spores. Inoculation was achieved by forcing the spore solution from the shell side of the membrane, through the membrane, to the lumen side (reverse filtration), as described in Govender *et al.* (2004). Immediately after the inoculation process, the system was fed with nutrients, supplied at a flow rate of 6.20ml/hr on the lumen side of the membrane. When more than one SFCMBR system was running, as shown in Figure 6-2, individual nutrient feeds were used so as to minimise the risk of contamination. The nutrient solution was allowed to fill-up the membrane lumen, before the pump was stopped and the system was left for 24hr for the spores to germinate and acclimatise to their new environment (referred to as the lag phase).

Following the 24hr lag-period, the nutrient supply was continued, and the system was allowed to run with as little disturbance as possible. The mode of operation was dead-end; the nutrient was forced to permeate through the walls of the membrane, to the fungus immobilized on the external skin of the membrane. Permeate was collected daily using 50ml bottles. The pH and redox potential of the permeate solution was monitored daily, using a Hanna HI 8314 pH meter in order to check whether the reactors were biochemically similar. A redox potential of above 200mV was used as an indicator of LiP and MnP activity (Leukes, 1999).

Humidified air was filter sterilized before being supplied on the shell side of the bioreactor at a flowrate of 240 L/hr, using a Hailea ACO 9220 diaphragm air pump. The system was fitted with pressure transducers at the inlet and outlet of the membrane, as shown in Figure 6-2. An experimental run consisted of 10 reactors connected to individual nutrient feeds as shown in Figure 6-2.

6.3.3 Scanning electron microscope preparation

After biofilm growth was visible in all the bioreactors, one bioreactor was stopped every 24hr and prepared for SEM imaging. Samples of the membrane, with biofilm growth, were cut with a sterile blade and placed into a 10% gluteraldehyde solution to preserve the biofilm. The samples were then taken through an alcohol dehydration series. This involved placing the samples in different concentrations of alcohol for at least 10 minutes each. This procedure is explained in APPENDIX H. Once the samples were in 100% alcohol they were taken to the Electron Microscopic Unit (EMU) at the University of Cape Town, where they were critical point dried

and sputter coated with gold/palladium for examination with the SEM. The SEM that was used was a fully analytical Leo S440 SEM. The SEM images were used to determine the biofilm thicknesses over time.

6.3.4 Hydraulic permeability

Two batches of membranes were used for all the experiments covered in this thesis, and the hydraulic permeability of each batch was determined experimentally. The hydraulic permeabilities were obtained by running distilled water through the lumen side of the SFCMBR at five different flowrates of 1.716ml/hr, 3.186ml/hr, 4.86ml/hr, 6.18ml/hr and 13.56ml/hr; and measuring the pressures at the inlet and outlet of the SFCMBR operated in the dead-end mode at 20°C, as explained in Section 6.3.1.

An investigation of the effect of temperature on the hydraulic permeability of the membranes was also performed. The hydraulic permeability of membranes at two differing temperatures of 20°C and 37°C was compared. For the bioreactor operated at 37°C the flowrates used were: 6.90ml/hr, 13.56ml/hr, 20.28ml/hr, 26.94ml/hr and 33.66ml/hr.

7. EVALUATION OF MODEL PARAMETERS

7.1 Introduction

In any process design or optimisation it is always desirable to have a method of examining the effects of uncertainties in the forecasting of process output variables. This is simply because 'if process behaviour can be predicted, then it can be controlled'. The study of how unknown variables might affect the overall performance of a unit operation is often referred to as a sensitivity analysis. In this chapter the effects of the different model variables, in both the numerical and analytical modelling of the momentum transfer of a SFCMBR, are evaluated.

7.2 Numerical scheme parameters

The sensitivity of the numerical and analytical models developed in this study was tested on a vertically orientated SFCMBR system, with a constant shell-side pressure, operated in the dead-end mode. The model parameter values for this system are listed in Table 7-1.

Table 7-1: Model parameter values used to test the developed models

Model parameter	Symbol	Unit	Basic value
Fraction retentate	f	dimensionless	0
Membrane hydraulic permeability	k_m	m^2	1.74×10^{-17}
Membrane inner radius	R_L	m	6.63×10^{-04}
Membrane outer radius	r_x	m	9.10×10^{-04}
Extra capillary space radius	r_2	m	5.91×10^{-03}
Glass manifold inner radius	r_3	m	10.91×10^{-03}
Effective membrane length	L	m	0.29
Inlet hydrostatic pressure	p_0	Pa	117.01×10^{3}
Outlet hydrostatic pressure	p_1	Pa	113.57×10^{3}
Osmotic pressure	π	Pa	100.00
Nutrient flowrate	Q	ml/hr	6.20
Nutrient medium viscosity	μ	Pa.s	1.18×10^{-3}
Nutrient medium density	ρ	kg/m^3	994.00

7.2.1 Stability analysis

Difference equations can be solved by employing a number of techniques and these techniques fall into one of two different general approaches; the implicit or explicit approach. The difference equations developed and solved in this study, Equations 5-64 and 5-65, each contain only one unknown and can therefore be solved explicitly in a straightforward manner. The unknowns are $U_{i,j}^{n+1}$ and $V_{i,j}^{n+1}$, since we assume that U and V are known at all grid points at time level n. By definition therefore, the solution of Equations 5-64 and 5-65 follows an explicit approach. Besides its simplicity compared to the implicit approach, a major disadvantage of an explicit approach is that there are restrictions on the values of the independent variables. Once $\Delta\tau$ is chosen, then ΔR is not an independent, arbitrary choice; rather ΔR is restricted to be equal or less than a certain value prescribed by a stability criterion. The von Neumann stability method is the most frequently used method to obtain the relationships between the independent variables of linear difference equations.

Unfortunately, an exact stability analysis of the difference representation of the nonlinear Navier-Stokes equations does not exist (Anderson, 1995). A trial-and-error approach was adopted to obtain a relationship between the independent variables of Equations 5-64 and 5-65. The relationship was found to be of the form:

$$\Delta\tau \leq \frac{\Delta\tau \times \Delta R}{0.0007} < 1 \qquad \textbf{7-1}$$

A more rigour stability analysis for Equations 5-64 and 5-65 was developed by Godongwana *et al.* (2007).

7.2.2 Grid independence

A tenable solution of a differential equation, when using a finite difference scheme (or finite volume method), should be independent of the number of grid points (or volume cells) used. If this condition is not met then the solution is not stable. This means that the steady-state values of U and V should be independent of the time increment chosen. Generally, to remedy this situation, the number of grid points used must be increased, i.e., the time increment needs to be decreased. In Table 7-2, decreasing $\Delta\tau$ from 0.01 to 0.005 improves the numerical solution only marginally;

Table 7-2: Grid independence of the flow field

$\Delta\tau$	U	V	(Z ;R)
0.1	2.33×10^{-6}	9.74×10^{-8}	(0.38; 0.09)
0.05	2.29×10^{-6}	1.38×10^{-7}	(0.38; 0.09)
0.01	2.26×10^{-6}	1.70×10^{-7}	(0.38; 0.09)
0.005	2.26×10^{-6}	1.75×10^{-7}	(0.38; 0.09)
0.001	2.25×10^{-6}	1.78×10^{-7}	(0.38; 0.09)
Analytical solution	2.29×10^{-6}	1.79×10^{-7}	(0.38; 0.09)

therefore the solution that uses $\Delta\tau$ equal to 0.01 is essentially grid-independent. The model parameter values corresponding to the velocity values in Table 7-2 are listed in Table 7-1, and the spatial increments ΔR and ΔZ were chosen to be 0.02.

7.2.3 Convergence of the numerical solver

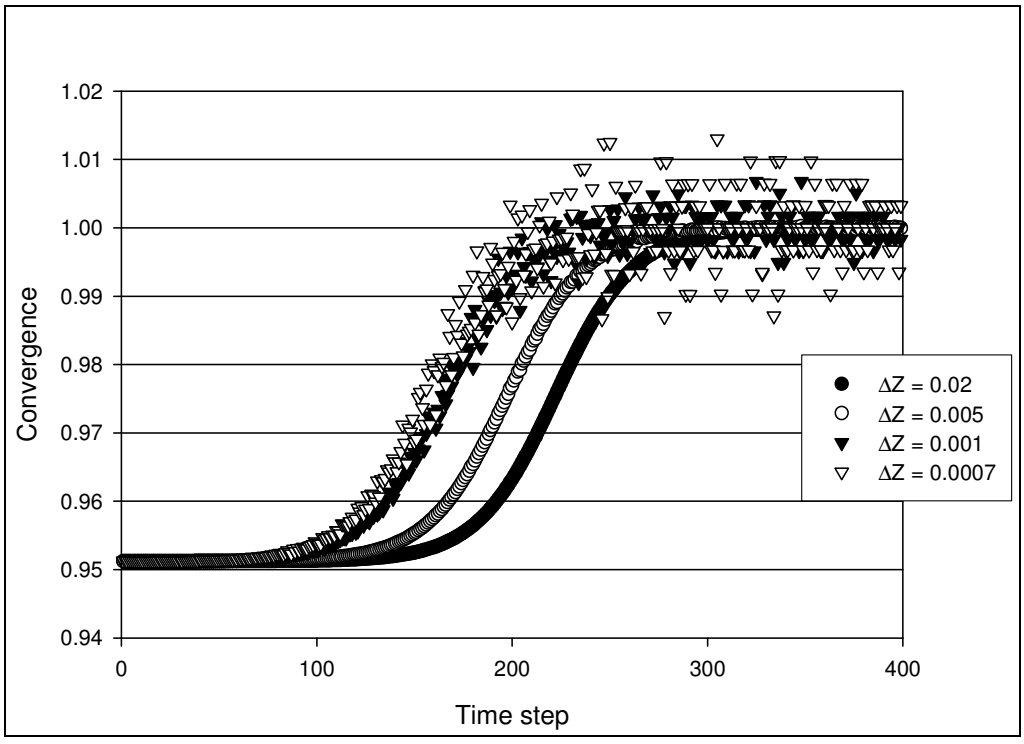

Figure 7-1: Convergence of the numerical solver as a function of grid spacing

The rate of convergence of the numerical solution is influenced by a number of factors including: the aspect ratio; the Re_w and the grid spacing. In Figure 7-1, the convergence is defined as U^{n+1}/U^n, and the solution is said to be converged when the value of the convergence is unity.

The influence of the grid spacing is that the rate of convergence increases with increasing grid spacing. This is demonstrated by a comparison of the time required for a grid spacing of 0.02 to converge to that of 0.0007, in Figure 7-1. On the other hand, the accuracy of the solution decreases with increasing grid spacing. The grid spacing required therefore and the corresponding accuracy will be dictated by the application of the numerical solver; and a trade off will have to be reached between a comprehensive solution that takes up more computing time and a less precise solution that is fairly quick to solve.

7.3 Analytical model parameters

7.3.1 Membrane hydraulic permeability

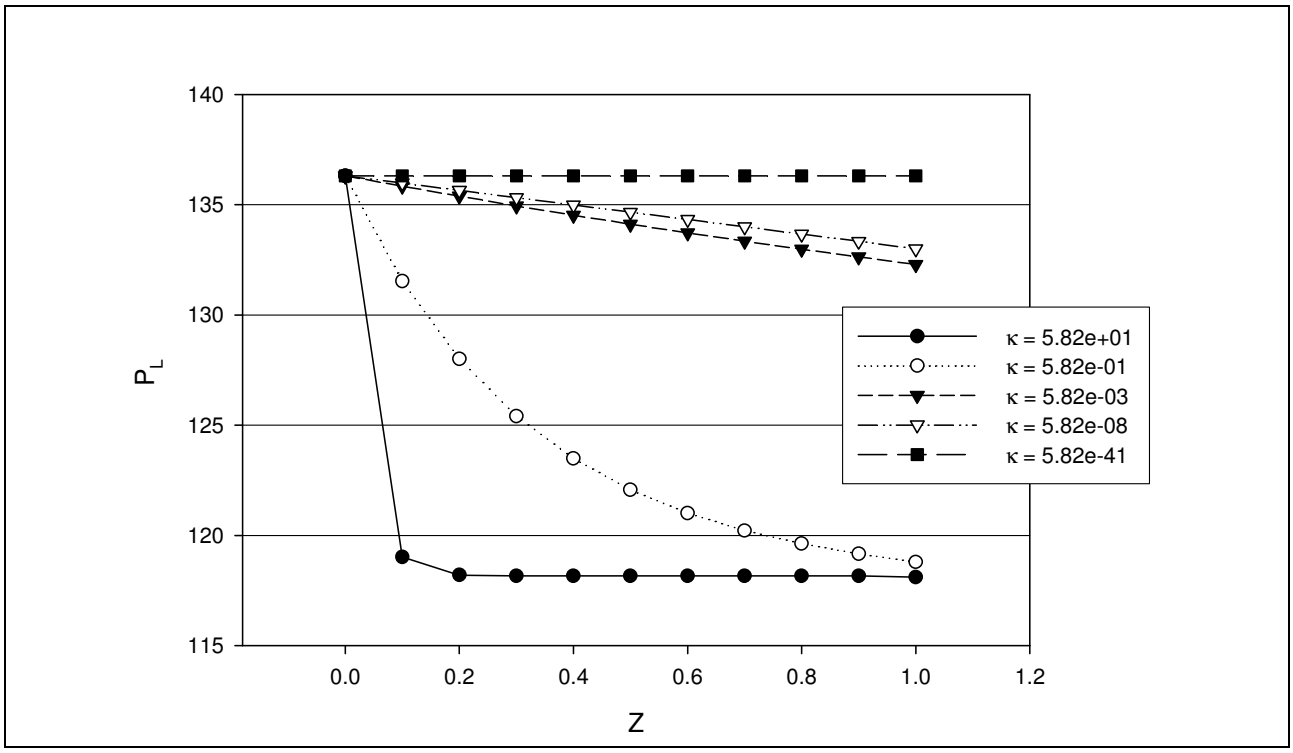

Figure 7-2: Pressure profile (P_L) as a function of hydraulic permeability (κ)

When the model parameter values in Table 7-1 are fitted to Equation 5-31, for different hydraulic permeabilities (κ), it can be deduced that the pressure drop along the membrane decreases with decreasing membrane hydraulic permeability. By way of illustration, when the dimensionless permeability decreases from 5.82×10^{-1} to 5.82×10^{-3}, as would be the case with increasing growth of the fungus, the dimensionless pressure drop, ΔP_L, also decreases from 17.5 to 4. In Figure 7-2,

ΔP_L is the difference between P_L at $Z = 0$ and at $Z = 1$. In the limiting case $\kappa \to 0$, the pressure profile will resemble that of a straight circular tube of constant cross section (Poiseuille flow). This result is also expected, since the pressure drop in a vertically orientated SFCMBR is merely due to permeation of the lumenal fluid and gravity. Figure 7-2 also indicates that the pressure drop is only linear for very small hydraulic permeabilities of the membrane. This result was also observed by Kelsey *et al.* (1990) in the simulation of a HF membrane bioreactor operated in the closed-shell mode.

7.3.2 Concentration polarization layer

The hydraulic resistance of the concentration boundary layer includes any layer (e.g., gel layer or cake) that deposits on the membrane surface. For the specific SFCMBR described in this investigation there were three main sources of this resistance, namely: (a) a gel layer deposit on the surface of the membrane as shown on Figure 7-3; (b) yeast cells forming a continuous strand on the surface of the membrane as shown on Figure 7-4; and (c) a combination of the yeast cells and gel layer as shown on Figure 7-5. The gel layer deposit on the surface of the membrane is a function of both flux, which increases the mass rate of material retained at the membrane, and cross-flow velocity, which reduces polarization by enhancing feed-side mass transfer (Perry *et al.,* 1998). If cross-flow velocity is insufficient, as is the case in dead-end mode operations, rejected solutes concentrate near the membrane to extremely high levels. This results in an increase in the osmotic pressure, which in turn acts negatively on the efficiency of the MBR.

The effect of the osmotic pressure on the velocity field is described in Section 7.3.3. Under thoroughly sterile conditions the only resistance to permeate flux is the gel layer deposit of retained solutes. However, in some of the experiments performed in this study, SEM images revealed the existence of a layer of yeast cells forming near the surface of the membrane, as shown on Figure 7-4. The effect of these cells is twofold: firstly, they form a secondary or dynamic membrane (this is sometimes referred to as autofiltration). Secondly, this dynamic membrane retains micro-solutes that would otherwise permeate through the membrane, resulting in increased osmotic pressures.

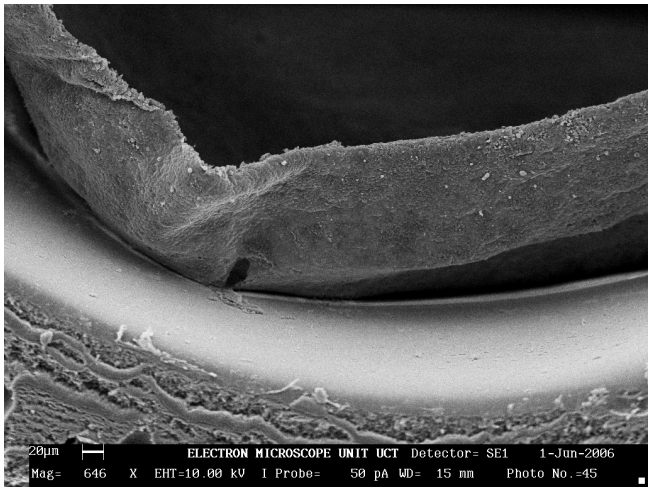

Figure 7-3: An SEM of gel layer deposit on the surface of the membrane

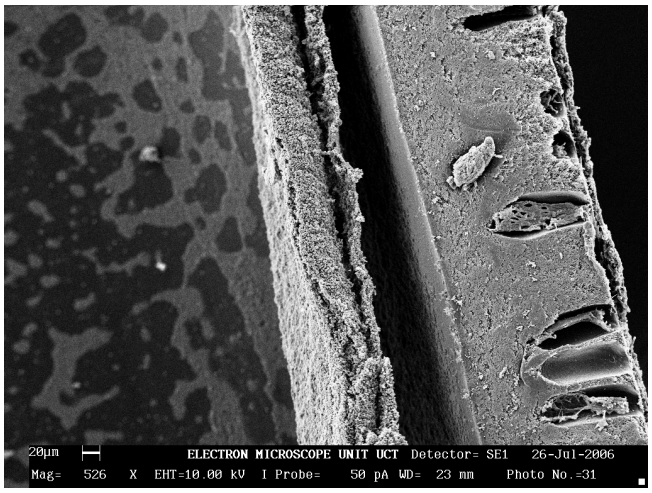

Figure 7-4: An SEM of yeast cells agglomerating near the surface of the membrane

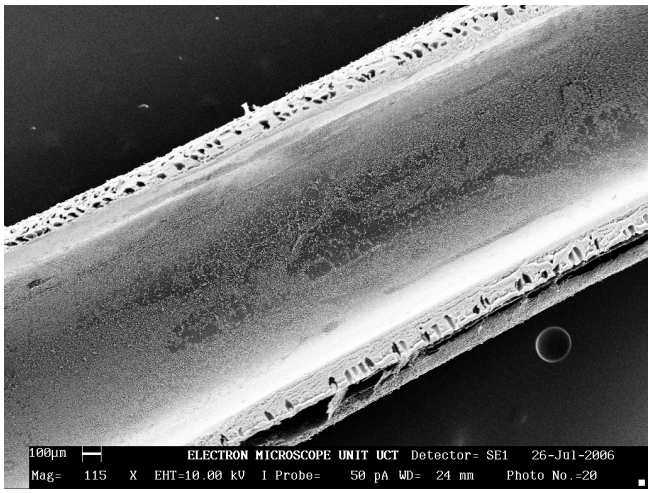

Figure 7-5: An SEM of yeast cells and gel layer forming a resistance layer to permeation

7.3.3 Osmotic pressure

The composition of the nutrient solution that was used is tabulated in Table D- 1 of Appendix D. Only glucose, thiamin and ammonium tartrate were considered as contributing species in solving Equation 3-17, for the osmotic pressure; for the simple reason that they were the only solutes with a molecular weight considered to be retainable by the membrane. The concentration of the species retained at the surface of the membrane, c_w, is related to the bulk concentration, c_b, by a material balance of the solute, when assuming total retention of the solute (Moussy, 2000):

$$J(x) = e(x)\ln\left[{}^{c_w}\!\!\diagup\!\!{}_{c_b} \right] \qquad \textbf{7-2}$$

where $J(x)$ is the local filtrate flux (or wall velocity) in m^3/m^2s, and $e(x)$ is the local mass transfer coefficient also in m^3/m^2s. The local mass transfer coefficient $e(x)$, for laminar flows in a circular tube, is evaluated from the Leveque relation (Perry *et al.,* 1998):

$$e(x) = 1.62\left(\frac{vD_{AB}^2}{Ld} \right)^{0.33} \qquad \textbf{7-3}$$

and the filtrate flux $J(x)$ is given by (Perry *et al.,* 1998):

$$J(x) = \left(\frac{QD_{AB}^2}{Ld^3} \right)^{0.33} \qquad \textbf{7-4}$$

where Q is the volumetric flowrate in m^3/s, and D_{AB} is the solute diffusity in m^2/s. Combining of Equations 7-2 to 7-4 results in the following expression for c_w:

$$c_w = c_b \exp\left[\frac{(\pi/4)^{0.33}}{1.62} \right] \qquad \textbf{7-5}$$

Equation 7-5 was formulated on the assumption of complete solute retention. During actual operation of the SFCMBR, however, this assumption is only valid after prolonged periods of operation. Solute retention on the surface of the membrane will increase with operation time of the membrane. To illustrate the effect of osmotic pressure on the axial velocity profiles, Equation 7-5 was substituted into Equation 3-17 for different hypothetical solute retentions. The resulting velocity profiles for the different osmotic pressures are shown in Figure 7-6.

In Figure 7-6, when the dimensionless osmotic pressure (Π) is zero, the velocity profile is maximal. However, an increase in the osmotic pressure, following an increase in c_w, results in the flattening of the axial velocity profiles and hence poor momentum transfer characteristics of the MBR.

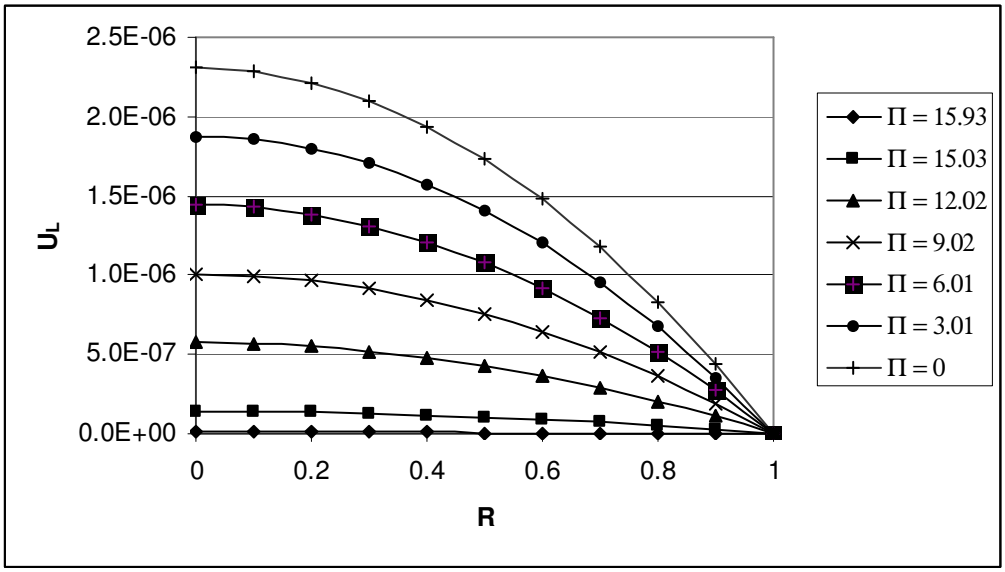

Figure 7-6: Dimensionless axial velocity profiles (U_L) as functions of the radial spatial coordinate (R) for different dimensionless osmotic pressures (Π)

7.3.4 Pressure drop across the membrane

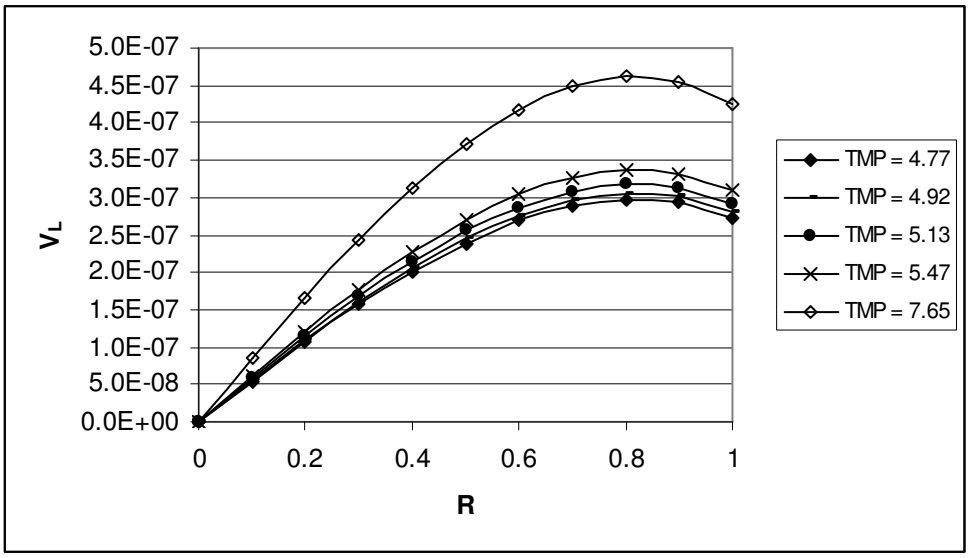

Figure 7-7: Dimensionless radial velocity profiles (V_L) as functions of the radial spatial coordinate (R) for different dimensionless transmembrane pressures (TMP)

Figure 7-7 is a plot of dimensionless radial velocity profiles (V_L) for different dimensionless TMP's for the model parameter values listed in Table 7-1, when using Equation 5-25. The numerical values of the dimensionless radial velocities (V_L), at R equal to one, correspond to the wall velocities of the membrane. As expected, an increase in the TMP results in higher wall velocities through the membrane.

8. RESULTS AND DISCUSSION

8.1 Introduction

In this chapter the experimental results, from the materials and methods described in Chapter 6, will be presented and discussed, with the aim of correlating the experimental data to the research objectives, as was stipulated in Chapter 1. These results include an evaluation of the hydrostatic pressure drops along and across the membrane; biofilm thicknesses; flow profiles; and hydraulic permeabilities. As stated in Chapter 1, the objective of this study was to present a detailed momentum transfer analysis of the nutrient solution in the membrane lumen, for a SFCMBR, operated continuously for LiP and MnP production. Although the models presented were developed for a SFCMBR in different modes of operation and orientations, these models were only tested for a vertically orientated SFCMBR, with an open-shell, operated in the dead-end filtration mode.

8.2 Hydraulic permeability (without biofilm growth)

8.2.1 Experimental and theoretical evaluation

Two batches of membranes were used for all the experiments covered on this thesis, and the hydraulic permeability of each batch was determined both experimentally and theoretically (using Equation 3-18). The data for the experimental evaluation was obtained by running distilled water through the lumen of a SFCMBR, with the dimensions listed in Table 7-1, at five different flowrates and measuring the pressures at the inlet and outlet of the SFCMBR, operated in the dead-end mode. This data was fitted to Equation 3-22, to obtain a profile such as the one in Figure 8-1. For the first batch of membranes, the numerical value obtained for k_m at 20°C was found to be 1.09×10^{-10}m/Pa.s (2.62×10^{-17}m^2), as shown in Figure 8-1. For the second batch, k_m at 20°C was found to be 7.26×10^{-11}m/Pa.s (1.74×10^{-17}m^2), as shown in Figure 8-2. To convert from m/Pa.s to m^2 the hydraulic permeability in m/Pa.s was multiplied by the product of the viscosity of the fluid and the membrane thickness (μd_w).

The Forchheimer equation with the correlation proposed by Ergun (1952) gives fairly accurate predictions of the value of k_m (see Appendix E). This model gives a prediction of $3.93\times10^{-17}m^2$ for k_m at 20°C and $4.68\times10^{-17}m^2$ at 37°C. This translated to a percentage error of <30%. The percentage error was calculated as: (the experimental value – theoretical value)/(experimental value). The Forchheimer equation was used to predict values of k_m when the fungus was immobilised on the surface of the membrane.

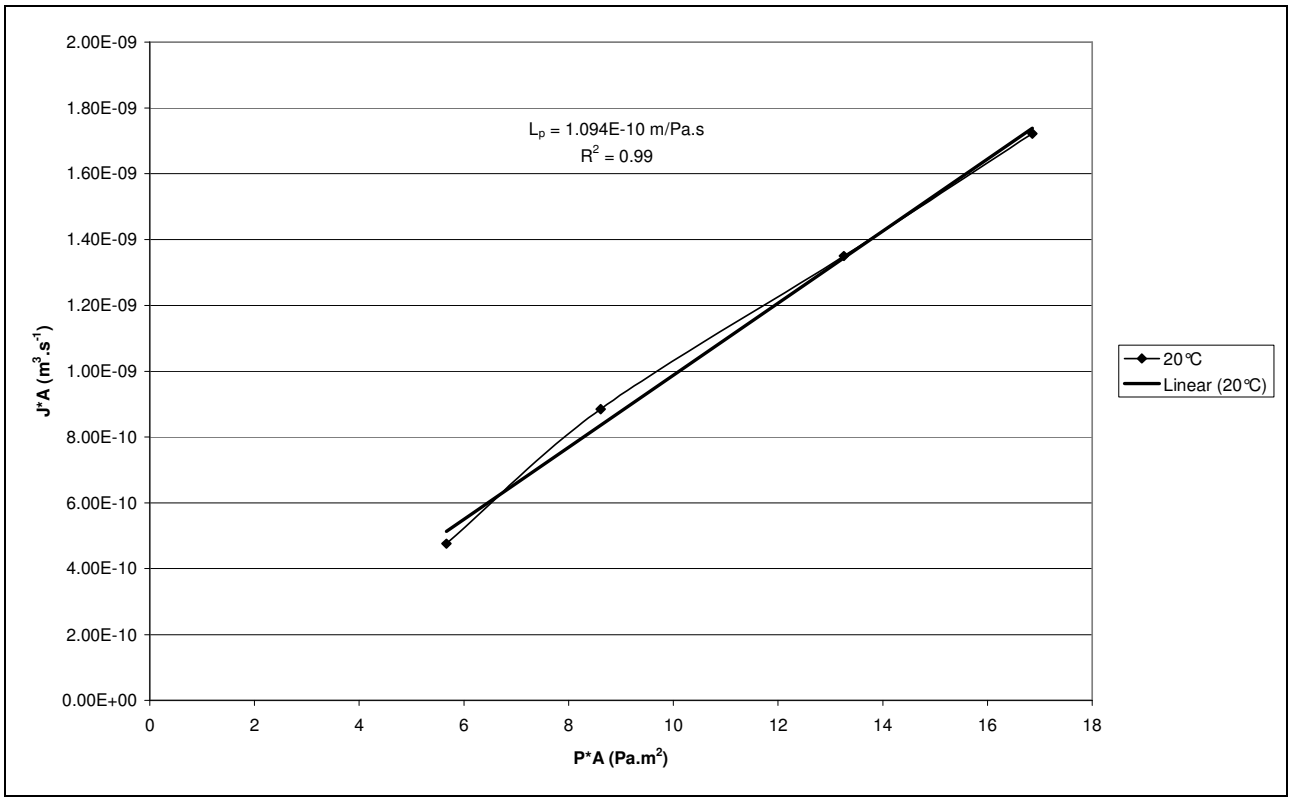

Figure 8-1: Hydraulic permeability of the capillary polysulphone membrane at 20°C

8.2.2 Membrane hydraulic permeability versus temperature

As mentioned in Section 3.3.3, the hydraulic permeability of polymeric membranes is dependant on the operating temperature. This dependency was studied by Garcin (2002) and Sharaf and Abo-Elmagd (2005). Figure 8-2 confirms that, for this study, an increase in temperature resulted in an increase in the membrane hydraulic permeability. In Figure 8-2, the hydraulic permeabilities of two PSu membranes, operated at two different temperatures of 20°C and 37°C are compared. For the bioreactor operated at 20°C the flowrates used were: 1.72ml/hr, 3.19ml/hr,

4.86ml/hr, 6.20ml/hr, and 13.6ml/hr. For the MBR operated at 37°C the flowrates used were: 6.90ml/hr, 13.6ml/hr, 20.3ml/hr, 26.9ml/hr, and 33.7ml/hr.

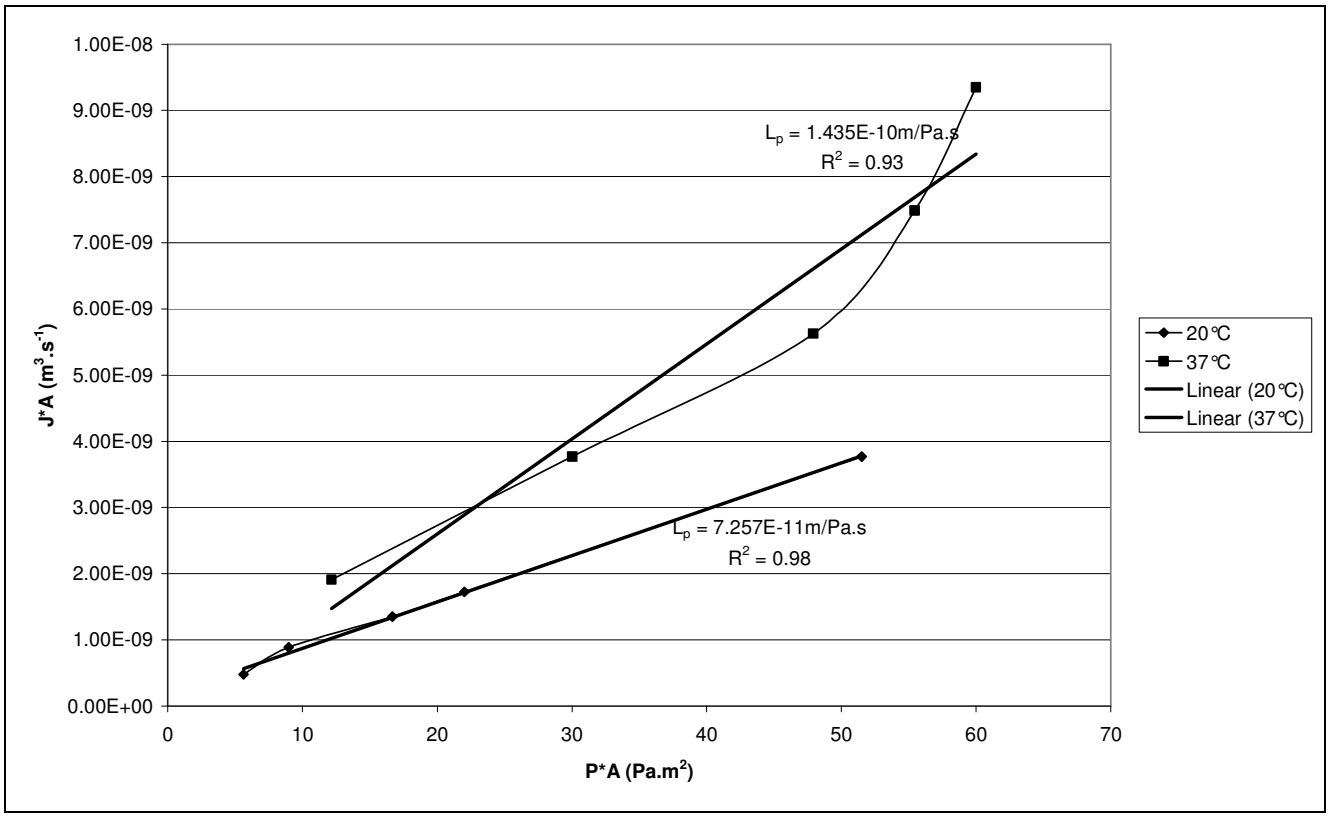

Figure 8-2: Hydraulic permeability of the capillary polysulphone membrane at 20°C and 37°C

8.3 Biofilm thicknesses

As a preliminary study to linking the biofilm growth to the momentum transfer analysis, experiments aimed at correlating the biofilm thickness to the membrane spatial coordinates and operational time were performed. The method used in the preparation of the biofilm for SEM imaging is described in Appendix H. The respective results of these experiments are shown in Figure 8-3 to Figure 8-5. Figure 8-3 represents the average biofilm thicknesses from 3 MBR's operated at a nutrient flowrate of 6.20ml/hr for 72 hr of operation. The general trend in Figure 8-3 is that the biofilm was thickest at the inlet and middle sections of the SFCMBR, and it gradually decreased towards the end of the membrane. This phenomenon was also observed by Sheldon and Small (2005), and was attributed to axial concentration gradients.

On average, biofilm growth was visible on the outside of the membrane after 72hr of operation. An SEM image of the biofilm development, on the membrane, is shown in Figure 8-4. As observed in Figure 8-5, the biofilm thicknesses increased with time. Figure 8-5 illustrates the biofilm thickness profile for 8 days of operation, when 3×10^{06} spores were inoculated on the capillary membrane. The thickest biofilms for the inlet, middle, and outlet sections were measured after 120hr (day 5) of operation.

Theoretically, the growth cycle of the fungus for a batch system consists of: (a) the lag phase; (b) the accelerated growth phase; (c) the exponential growth phase; (d) the decelerated growth phase; and (e) the stationary phase (Ntwampe, 2005; Ntwampe & Sheldon, 2006). The first 24hr in Figure 8-5 correspond to the lag phase of acclimatisation. After 24hr up to 96hr the first exponential growth was observed, and after 96hr a second exponential growth phase, referred to as biphasic growth, was observed (Kodama *et al.*, 1969; Meunier *et al.*, 1999).

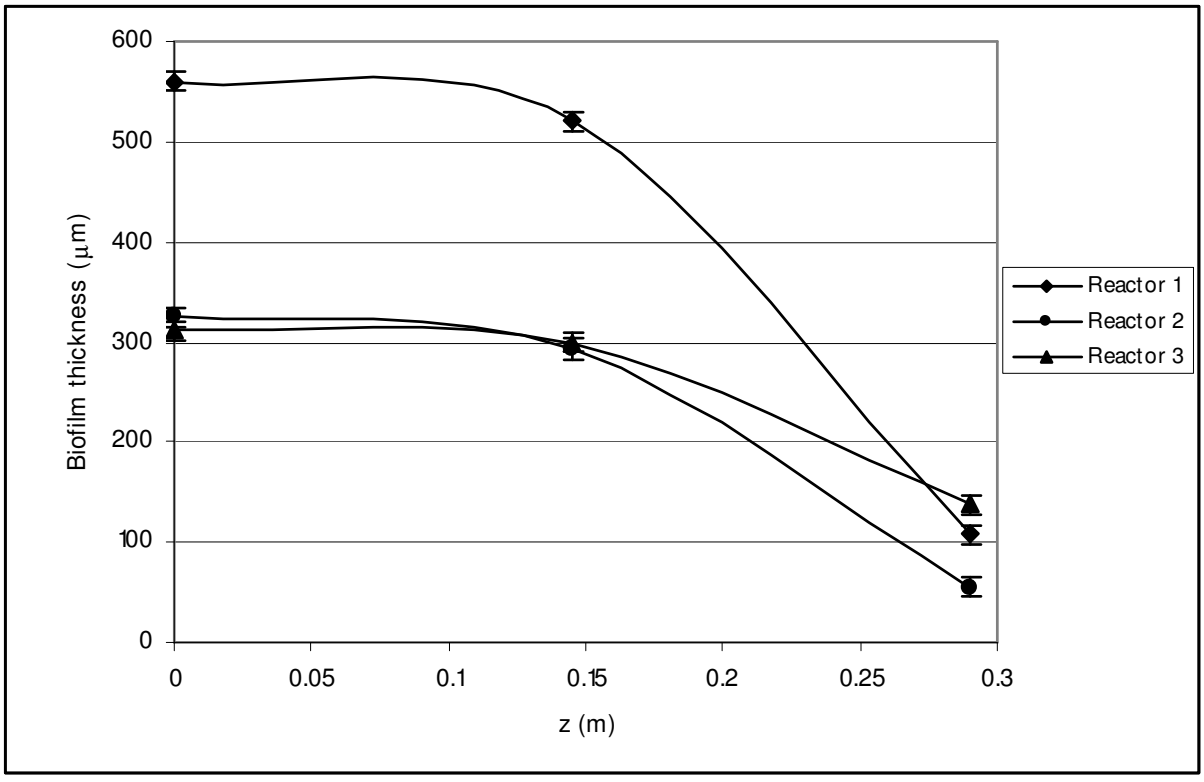

Figure 8-3: Average biofilm thickness along the length of the SFCMBR after 3 days of operation

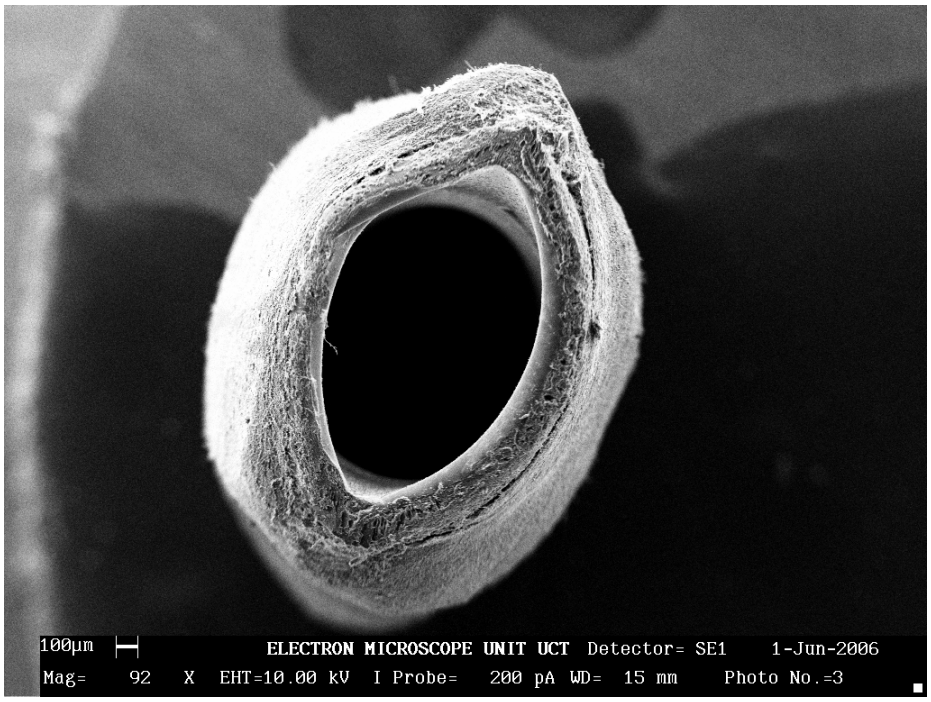

Figure 8-4: A scanning electron microscope (SEM) image of the membrane with biofilm taken after 3 days of operation

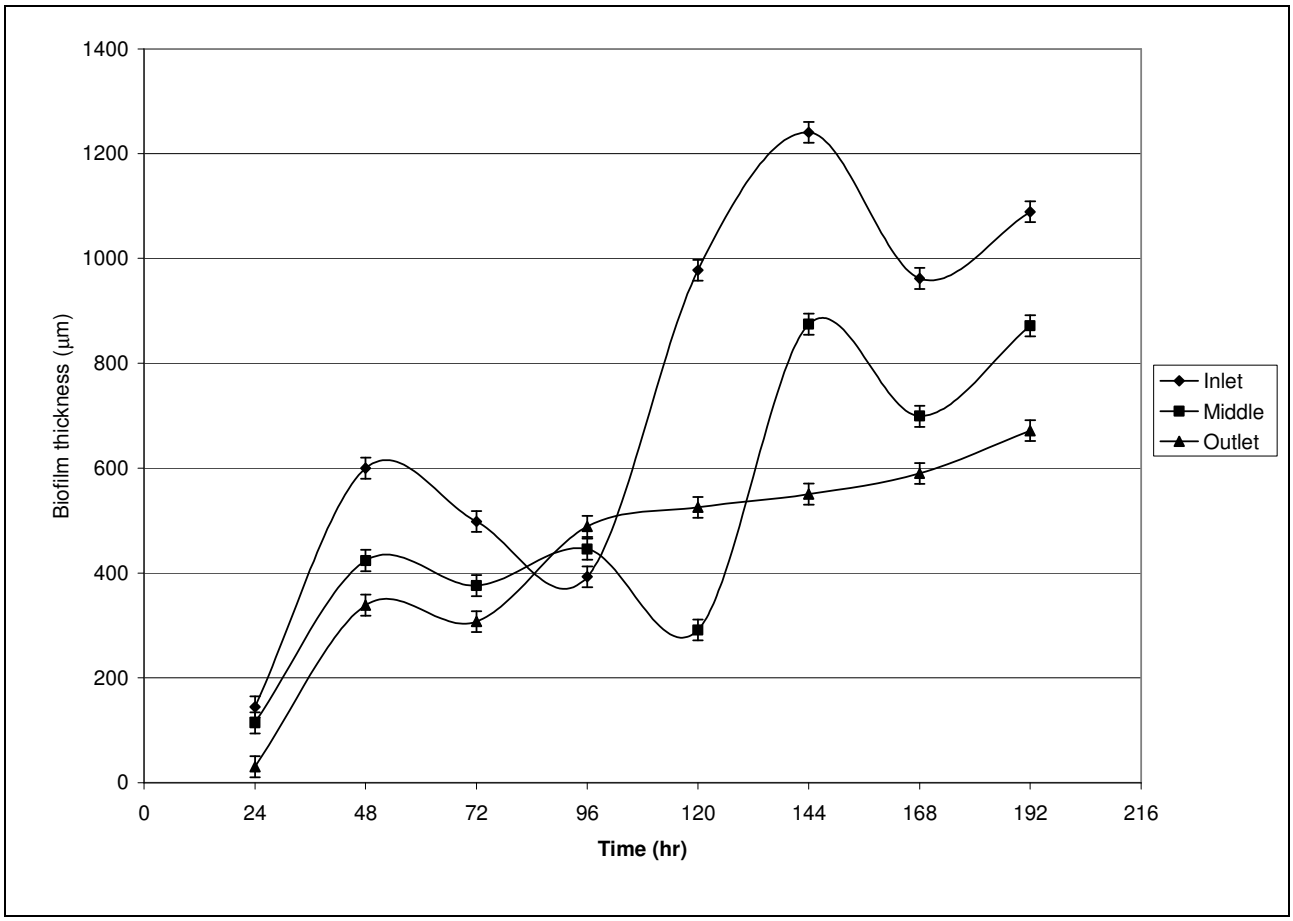

Figure 8-5: Average biofilm thickness of the SFCMBR as a function of time

8.4 Hydrostatic pressure drop

8.4.1 Pressure drop along the membrane for the control experiments (*without biofilm growth*)

An evaluation of changes in the pressure drop along the membrane for different membrane lengths, at varying flowrates, was performed. These experiments were aimed at comparing pressure drops between the vertical and horizontal orientations for different reactor lengths. Figure 8-6 is a plot of the results from these experiments. Distilled water was used as the liquid medium running through the membrane with no growth on the surface. From the experimental data of the 3 different membrane lengths used (0.233m, 0.29m and 0.55m) at 3 different flowrates (10.20ml/hr, 6.60ml/hr, and 3.54ml/hr) it was found that the axial pressure drop along the membrane, from inlet to outlet, for the vertical SFCMBR increased linearly with membrane length. The pressure also decreases linearly along the length of the membrane, as expected. On the contrary, the pressure drop on the horizontal SFCMBR generally remained constant with increasing length, as shown on Figure 8-6.

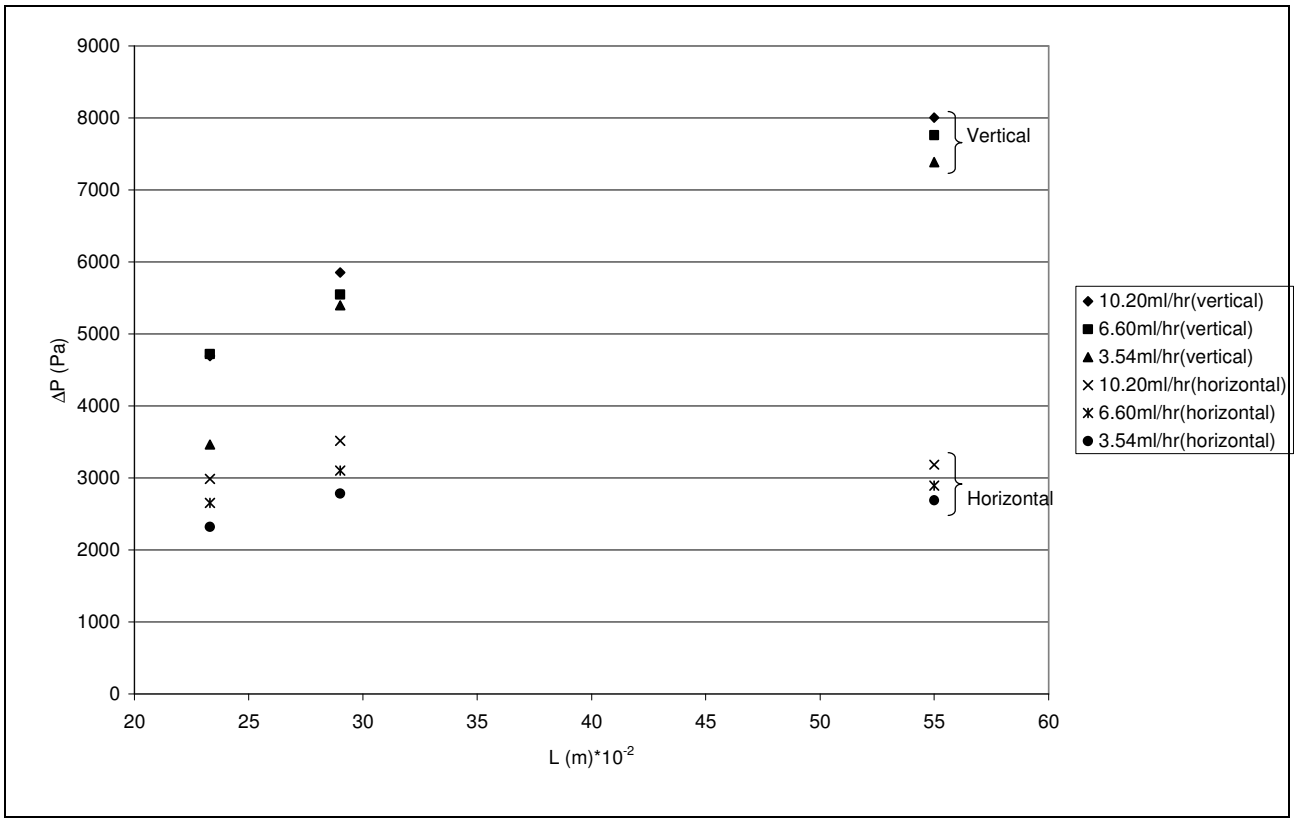

Figure 8-6: Membrane axial pressure drop (*ΔP*) versus membrane length for the horizontal and vertical orientations

The differences in the pressure drops between the horizontal and vertical SFCMBR, for the same operating conditions, highlight the error of using models developed for the horizontal configuration in the vertical orientation. These differences highlight the significance of the contributions of gravitational effects on the hydrostatic lumenal pressure profile in the vertical SFCMBR. As can be extrapolated from Figure 8-6, the difference will increase even further with an increase in the membrane length, and therefore at longer membrane lengths most of the published models will not be suitable for modelling the pressure profile of a vertical SFCMBR.

8.4.2 Pressure profiles during operation with biofilm growth

A series of experiments were performed to investigate the effect of the *P. chrysosporium* biofilm development on the pressure profile. As can be seen in Figure 8-7 to Figure 8-9, initially there is a linear increase in both inlet and outlet hydrostatic pressures with time. In Figure 8-7 this linear increase in pressure continues to the end of the experiment (108hr of operation). In Figure 8-8 and Figure 8-9, however, this linear pressure increase continues up to ±120hr of operation. After this period an exponential increase in the pressures can be seen. The difference in hydrostatic pressures between the inlet and outlet generally remained constant throughout the duration of the experiments (± 3kPa for a flowrate of 6.20ml/hr).

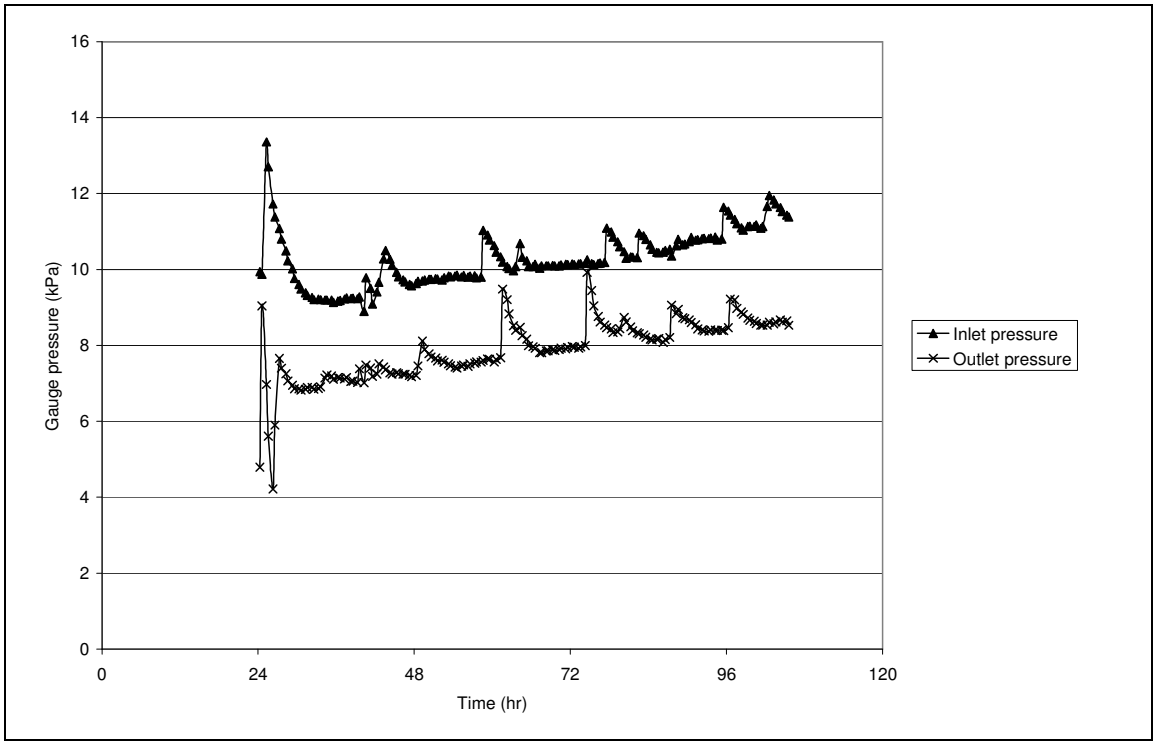

Figure 8-7: Pressure profiles of the vertical SFCMBR with *P. chrysosporium* (3×10^6 spores) on the external surface of the membrane at a flowrate of 6.20ml/hr

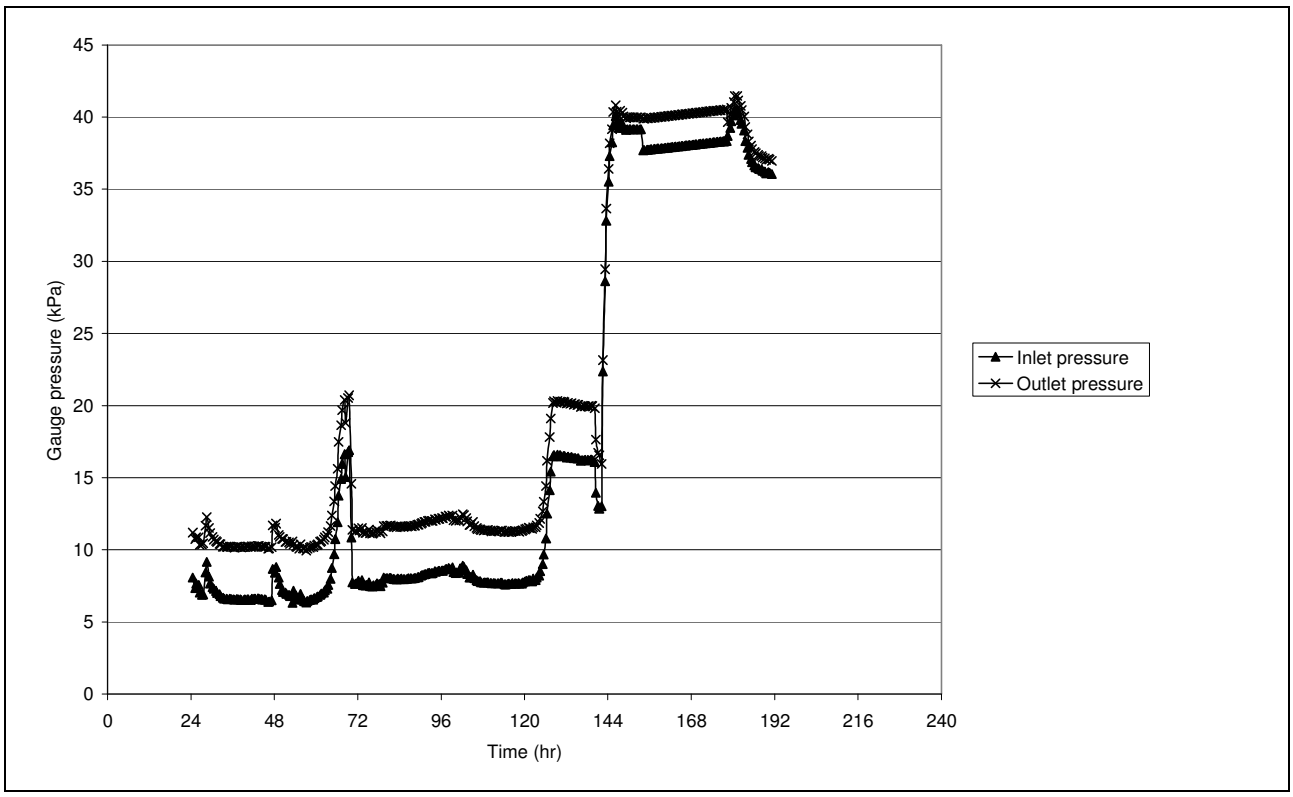

Figure 8-8: Pressure profiles of the vertical SFCMBR with *P. chrysosporium* (3×10^6 spores) on the external surface of the membrane at a flowrate of 6.20ml/hr

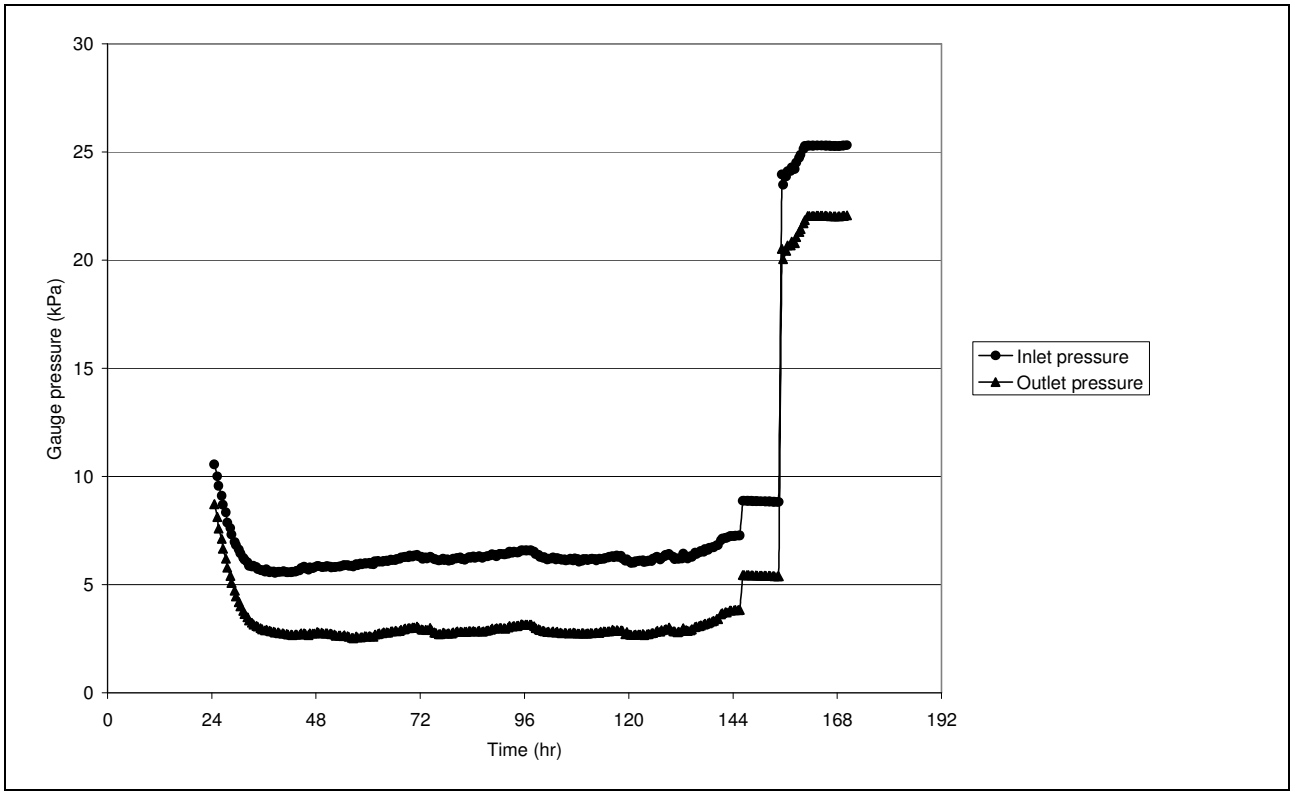

Figure 8-9: Pressure profiles of the vertical SFCMBR with *P. chrysosporium* (3×10^6 spores) on the external surface of the membrane at a flowrate of 6.20ml/hr

The exponential increase in the pressures, as observed in Figure 8-8 and Figure 8-9, can be attributed to the growth phases of the fungus. This exponential increase is presumed to be as a result of the secondary exponential growth phase that was previously shown in Figure 8-5 and discussed by Ntwampe and Sheldon (2006). Because the operation is continuous, the fungus immediately goes into a secondary exponential growth phase after the deceleration phase. An exponential increase in biofilm growth will result in higher resistances of the membrane to permeation. Because the mode of operation is dead-end, this increase in resistance has to be accompanied by an increase in TMP for a constant flux system.

8.4.3 Pressure predictions using developed model versus literature models

A comparison of Equation 5-31 with two of the most widely used models for predicting pressure profiles in HF and capillary membrane devices is shown in Figure 8-10. The model parameter values used for this comparison are listed in Table 7-1, and this simulation was done for a vertically orientated SFCMBR. Figure 8-10 clearly shows the divergence of the Bruining (1989) and Kelsey *et al.* (1990) models from the experimental data. The developed model gives an average percentage error of 0.5%, whereas the Bruining (1989) and Kelsey *et al.* (1990) models give percentage errors of 1.5% and 3% respectively. This discrepancy is amplified with increasing membrane length, as shown on Figure 8-10. The difference between Equation 5-31 and the Bruining (1989) and Kelsey *et al.* (1990) models is that this model accounts for osmotic pressure and gravitational force, whereas the others do not. Equation 5-31 indicates a linear decline in the hydrostatic pressure along the length of the membrane. This result is in agreement with Catapano's (1990) contention that the axial pressure profile is linear when there is 'no-slip' velocity.

The challenge that still remains, however, in validating the accuracy of Equation 5-31 is devising a means of experimentally obtaining the pressure profiles within the membrane lumen. Only the inlet and outlet pressures to the SFCMBR could be measured experimentally. Quaile and Levy (1975) used a hot wire anemometer to experimentally obtain the velocity profiles in a porous tube of 9.4mm inner diameter (7 times bigger than the one used in this study) with wall suction. From such a profile, it is possible to obtain a pressure profile of the flow, and this could be used to validate the theoretical predictions. Another alternative would be to use ultrasonic velocimeters

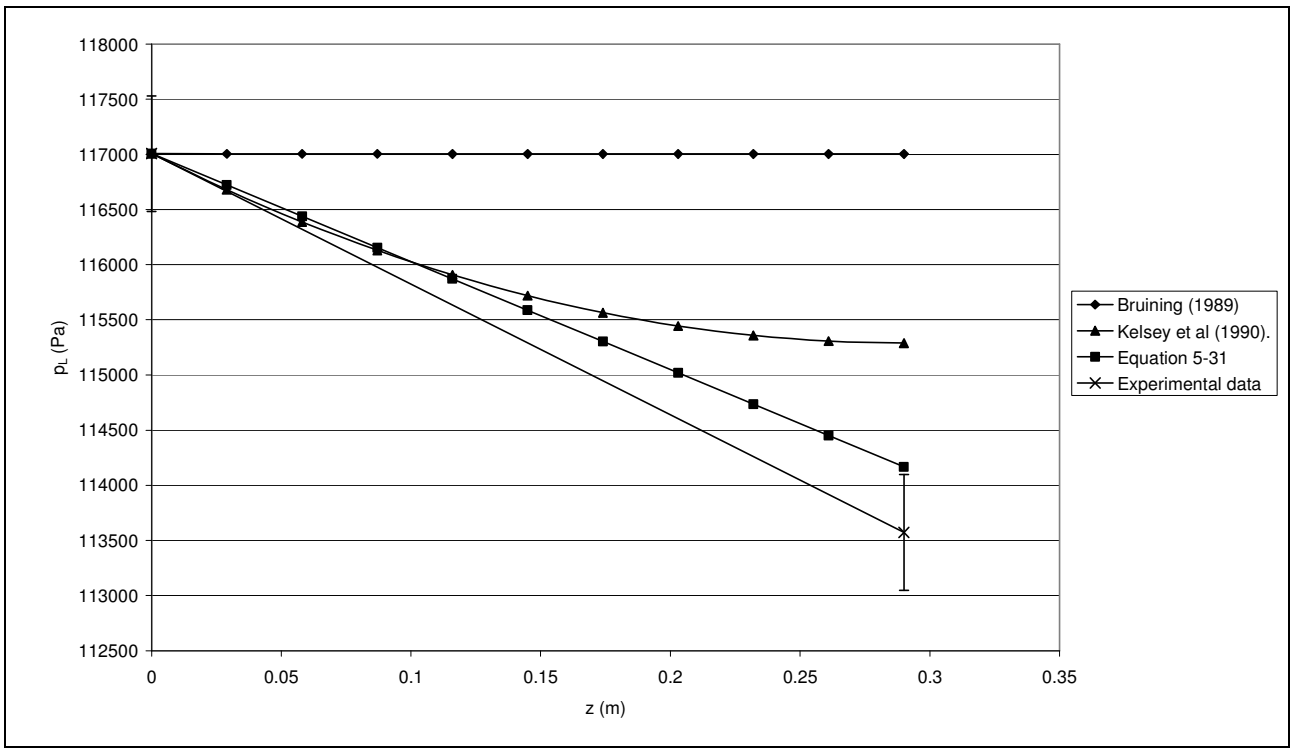

Figure 8-10: A comparison of the developed model with literature models and experimental data

(custom made for the size of capillary membranes used) or magnetic resonance imaging to obtain the velocity profiles, and from these profiles determine the pressure profiles. The major hindrance in using the commonly available instruments for measuring the pressures is the small sizes of the capillary membranes used.

8.4.4 Osmotic effects on pressure profile (without biofilm growth)

The osmotic pressure plays a very significant role in influencing the hydrodynamics of a MBR. To evaluate this function, four different hypothetical osmotic pressures were fitted to Equation 5-31 for a MBR with the dimensions listed in Table 7-1. As can be seen on Figure 8-11, an increase in the osmotic pressure tends to depress the lumenal pressure profile (and hence the TMP). Osmotic pressure in a SFCMBR was as a result of solutes being rejected on the surface of the membrane, thereby creating a concentration polarization layer (this phenomenon was explained in Section 3.3.4). Only significantly high concentrations (i.e., high osmotic pressures) will have a significant influence on the lumenal pressure profile, as can be seen on Figure 8-11. This result has very important consequences in the optimisation of capillary MBR, in particular

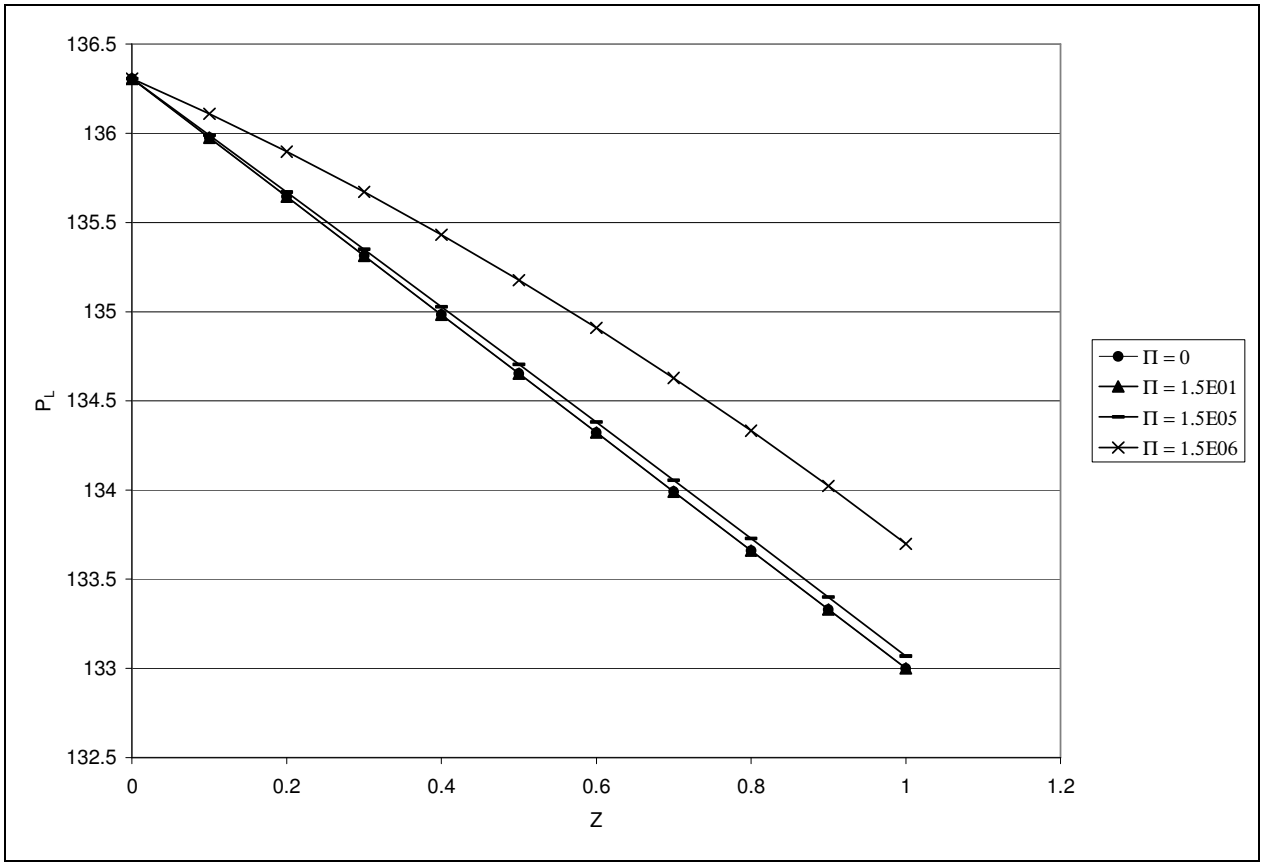

Figure 8-11: Dimensionless lumenal pressure profiles (P_L) as functions of the axial spatial coordinate (Z) for different dimensionless osmotic pressures (Π)

minimising secondary flows within the extra-capillary space. Taylor and Boukouris (1995) theoretically demonstrated that secondary (Starling) flows within the extra-capillary space of HF bioreactors can be reduced by increased osmotic pressures on the shell-side of the bioreactor.

8.5 Flow profiles (without biofilm growth)

8.5.1 Velocity profiles

The steady-state lumenal and matrix velocity distributions, as calculated from Equations 5-24, 5-25 and 5-27, are shown on Figure 8-12. It is noted that as the dimensionless radial coordinate (R) increases, the dimensionless axial velocity (U_L) decreases, until it reaches zero at $R = 1$ (at the membrane wall). This result is consistent with the 'no slip' condition of Equation 5-14d. The radial velocity (V_L), which is zero in Poiseuille flow, has a finite magnitude except at $R = 0$ (at the membrane centre) where it is zero. These solutions assume similarity in the velocity profiles since the $Re_w < 1$ (see Appendix E). Similarity in velocity profiles only exists for 'fully developed

flows'. In the current experimental set-up, the flow entering the SFCMBR was fully developed and hence there was similarity of the profiles.

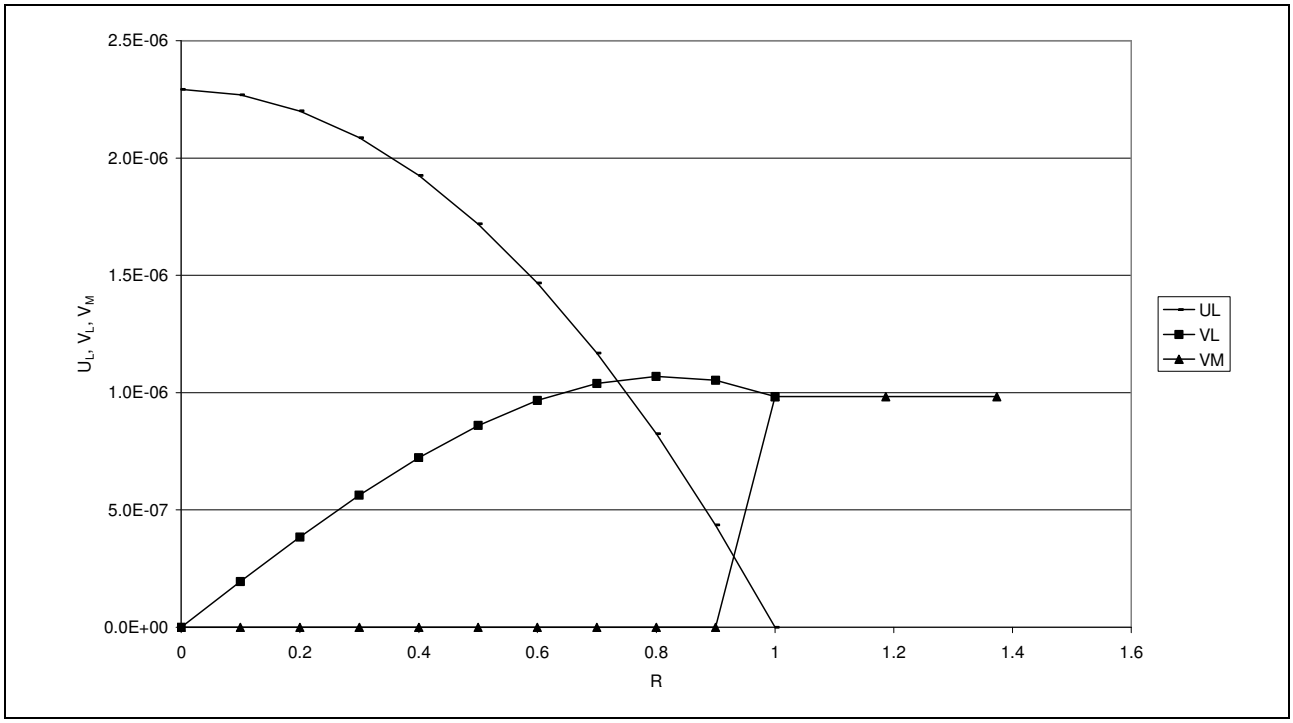

Figure 8-12: Steady-state velocity profiles in the lumen (U_L, V_L) and matrix (V_M) of the SFCMBR as a function of the radial spatial co-ordinate (R)

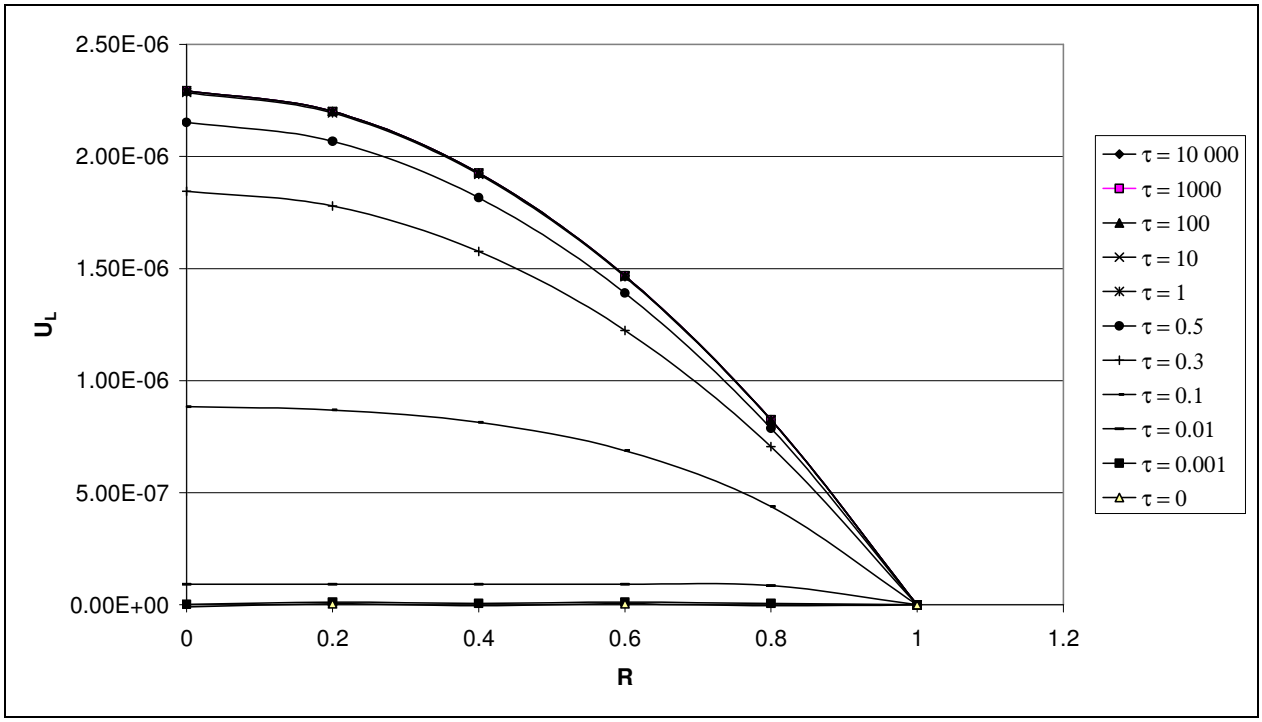

Figure 8-13: Transient lumenal axial velocity profiles (U_L) as a function of the radial spatial co-ordinate (R)

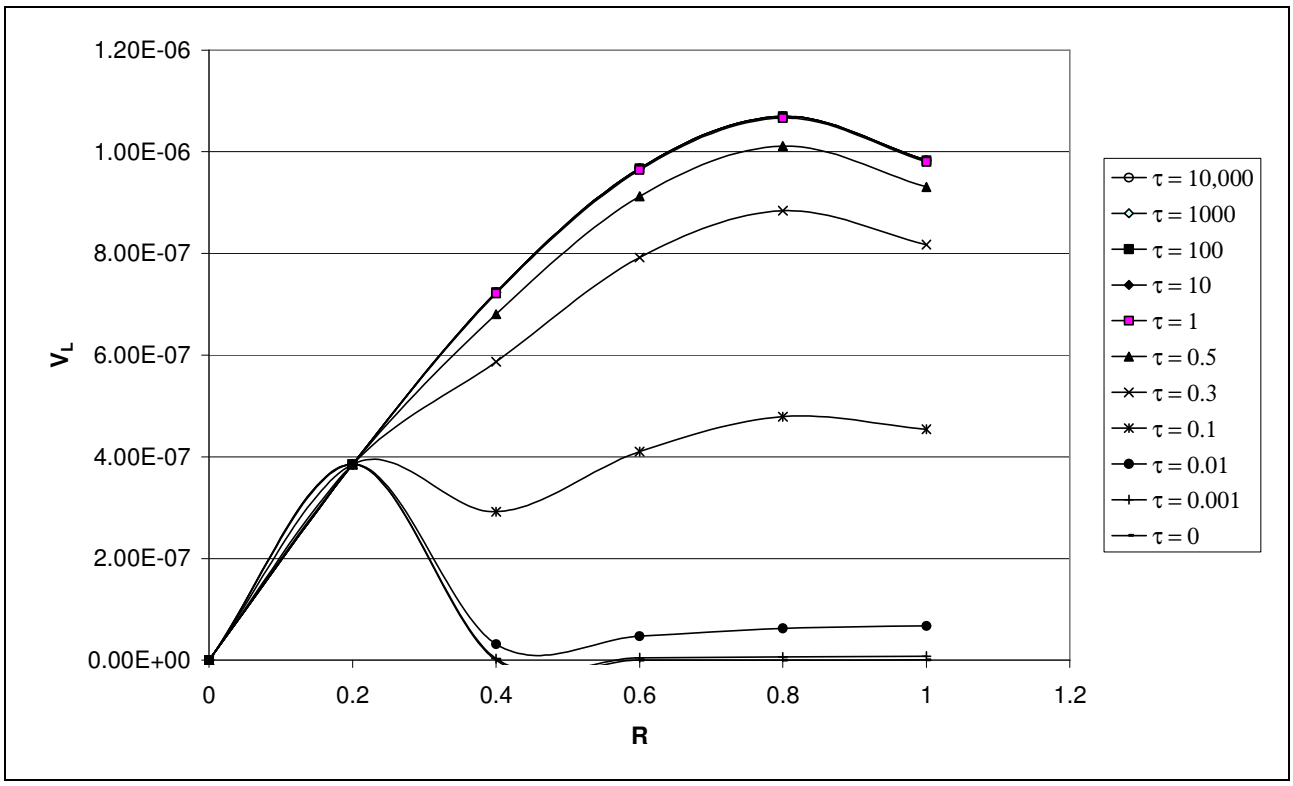

Figure 8-14: Transient lumenal radial velocity profiles (U_L) as a function of the radial spatial co-ordinate (R)

The resulting transient-state axial and radial velocity profiles from the developed analytical models, Equations 5-24 and 5-25, respectively, are plotted in Figure 8-13 and Figure 8-14. As can be seen from both figures, in the limiting case $\tau \to \infty$, the velocity profiles approach steady-state. For the model parameter values listed in Table 5-1 this corresponds to a $\tau = 1000$ (7.5min).

8.5.2 Streamlines

The method of producing a streamline from Equation 5-35 is to set ψ_L equal to an arbitrarily chosen constant and plotting the *R* versus *Z* curve. Other streamlines are obtained by setting ψ_L equal to various other constants. To obtain *R* for a given *Z* value in Equation 5-35 is an iterative process. Unfortunately, the solver algorithm used (Microsoft solver®) does not converge for the range $Z = 0$ to $Z = 1$. However, the shape of the streamlines can still be extracted by recognising that the function of the streamline is a polynomial of the 4th degree in *R*. Several of the streamlines are plotted in Figure 8-15, for a choice of the model parameter values in Table 5-1. For the same parameter values, and for a different fraction retentate ($f = 0.8$), the streamlines take the form shown in Figure 8-16. These profiles are similar to those developed by Kelsey *et al.* (1990). The streamlines indicate that the fluid tends to curl towards the membrane surface, away

from the membrane centre, during dead-end filtration. The functions *f(Z)* and *f(R)* are functions of the dimensionless axial and radial spatial coordinates respectively, and were derived from Equation 5-35.

An alternative method to produce the streamlines is to plot 3-dimensional lumenal axial velocity profiles for different radial coordinates. When using this method, the streamlines for the upper half of the membrane are shown in Figure 8-17. This method also produces a similar result of lines (representing flow path) curling towards the membrane surface in the dead-end filtration mode.

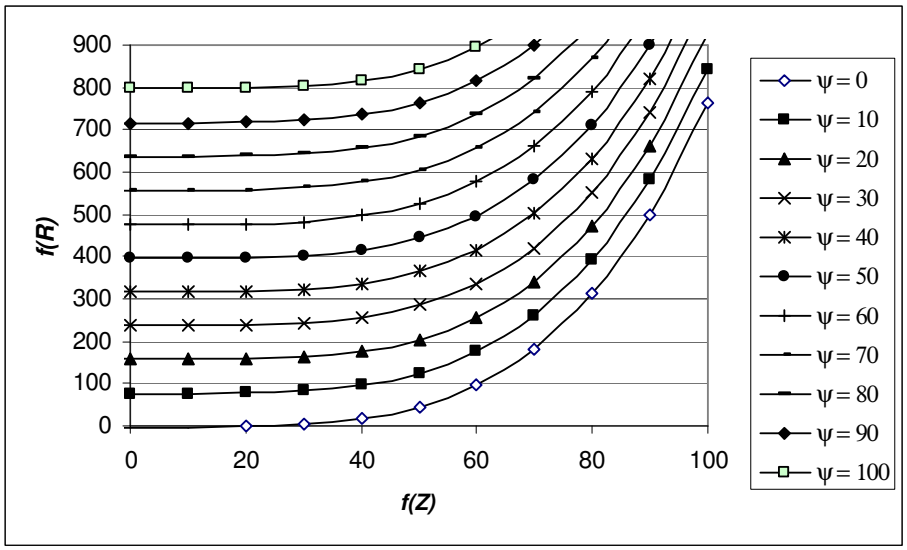

Figure 8-15: Streamlines in the upper half of the capillary membrane operated in the dead-end mode (*f* = 0)

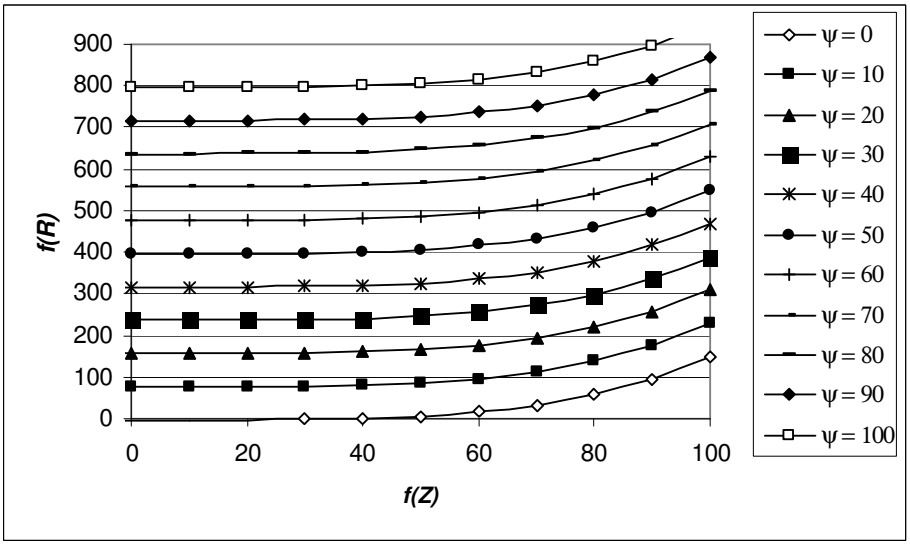

Figure 8-16: Streamlines in the upper half of the capillary membrane operated at *f* = 0.8

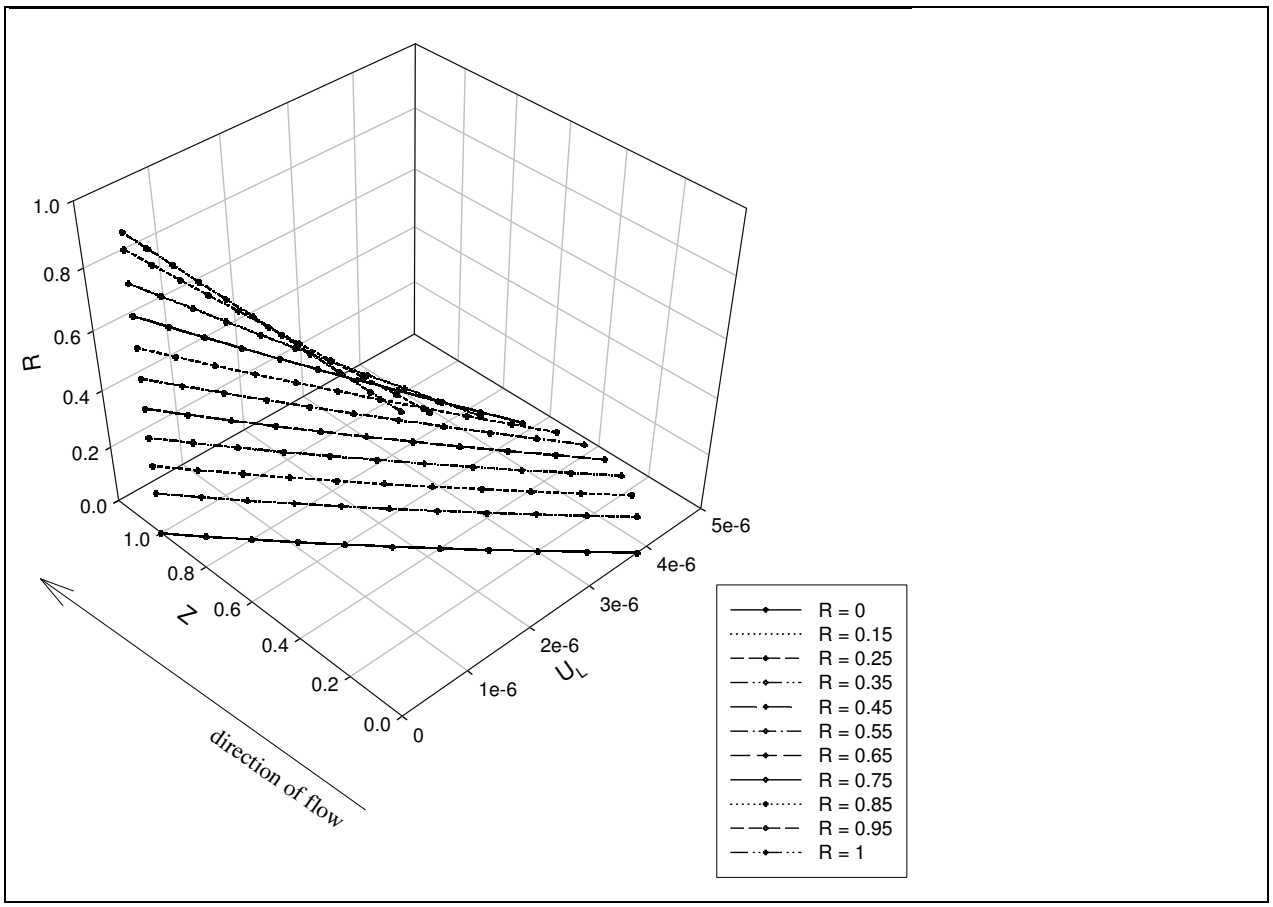

Figure 8-17: Streamlines for the upper half of the polysulphone capillary membrane operated in dead-end filtration mode (f = 0)

8.5.3 Volumetric flow

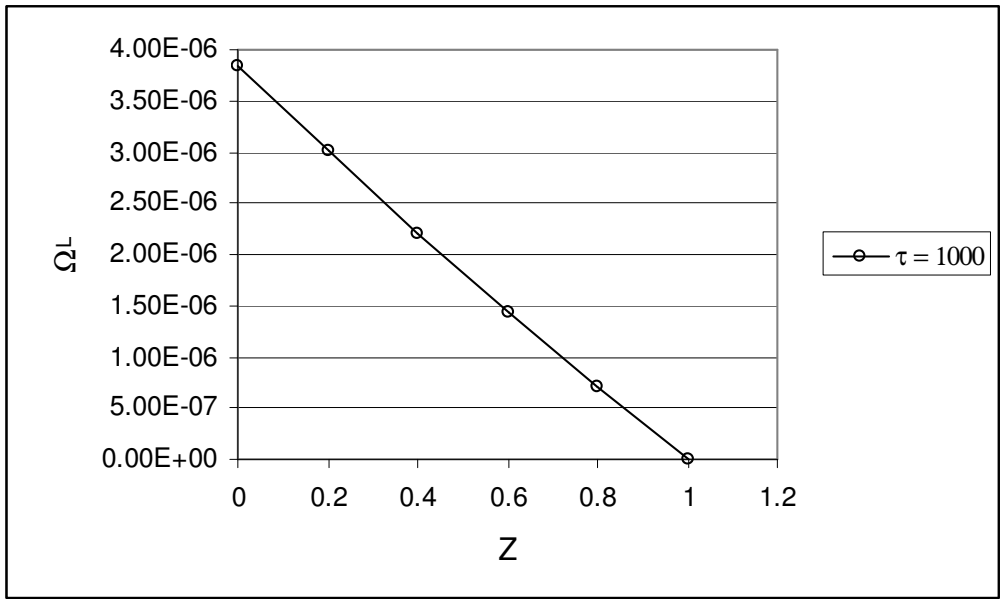

Figure 8-18: Volumetric flow (Ω_L) profile as a function of the axial spatial coordinate (Z)

The dimensions of the experimental SFCMBR used to generate the profile in Figure 8-18 were listed in Table 7-1. From Equation 5-26, if the dimensionless lumenal pressure profile, P_L, is linear, then the dimensionless lumenal volumetric flowrate, Ω_L, will also be linear, as shown in Figure 8-18. The volumetric flow profile, illustrated in Figure 8-18, is for a SFCMBR operated in the dead-end mode. At $Z = 1$ (at the membrane exit) there is zero flow of the lumenal fluid. This profile is in contrast with that developed by Kelsey *et al.* (1990) for a closed-shell mode bioreactor. In the closed-shell mode, Kelsey *et al.* (1990) noted that the volumetric flowrate was nearly constant along the length of the bioreactor. This was attributed to Starling flow that occurs in the closed-shell mode. This theoretical consideration of the flowrate is an important consideration in the design, and more specifically the choosing of the appropriate mode of operation, of a MBR.

8.6 Redox potentials and pH

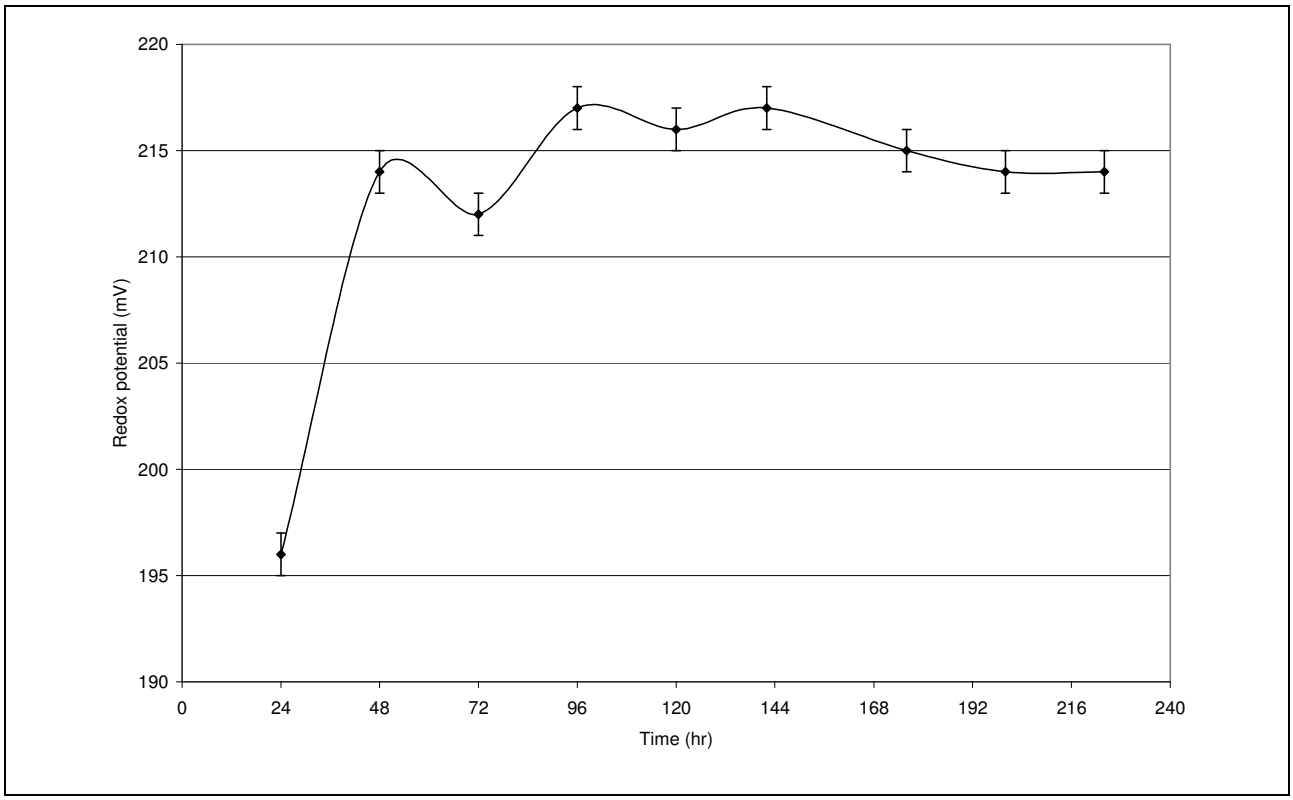

Figure 8-19: Example of the average redox potentials of the permeate solution from the SFCMBR

Although the exact mechanism for pH changes were not known, Leukes (1999) and Solomon (2001) established that pH changes are related to LiP and MnP production in a SFCMBR. These

researchers also reported that enzyme activity was detected above redox potential (mV) values of 200. In the current study, the pH and redox potential values were monitored for the full duration of an 8 day experimental run, and the average results are shown in Figure 8-19 and Figure 8-20 respectively. As shown in Figure 8-19, the redox potential increased from 196 mV after 24hr to peak at 218 mV after 96hr of operation. As shown in Figure 8-20, the pH decreases gradually during the operation, from 3.7 after 24hr to 3.45 after 216hr.

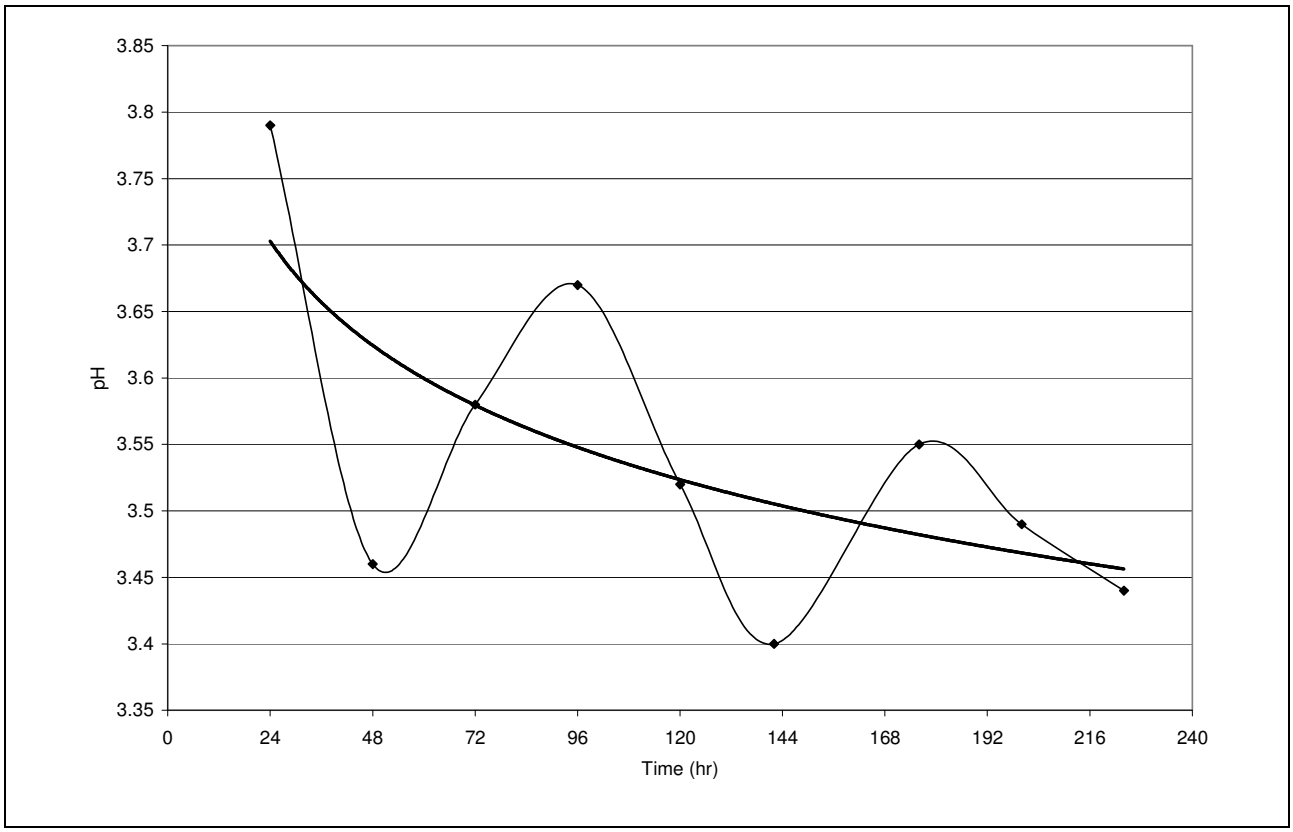

Figure 8-20: Example of the average pH profile of the permeate solution from the SFCMBR

9. CONCLUSIONS

9.1 Summary

The purpose of this study was to develop momentum transfer models for the nutrient on the lumen side of a capillary polysulphone membrane in a SFCMBR, operated continuously for enzyme production, which incorporate osmotic pressure effects and account for the different modes and orientations of membrane operations. These models were developed, and from a comparison of the developed analytical models with experimental data and some of the widely used models from literature, the predictive capabilities of the developed models were validated. A sensitivity analysis was performed on all the input variables in the developed model. The developed analytical flow profiles were for the hydrostatic pressures, axial and radial velocities, and volumetric flows in the lumen and shell-sides of the SFCMBR.

A numerical scheme, restricted to lumenal profiles, was also developed. It was shown that a comprehensive solution for the numerical scheme required a finer grid, which required more time computations, and the accuracy of the scheme decreased with increasing grid spacing.

A polarization deposit layer was observed inside the lumen of some of the membranes after day 4 to day 5 of operation, however due to the inconsistency in the occurrence of this layer, the resulting osmotic pressure effects could only be studied hypothetically. The osmotic pressure was shown to have a negative effect on both the pressure and velocity profiles. An increase in osmotic pressure was shown to reduce the radial and axial velocity profiles, while decreasing the TMP at the same time.

A comparison of the axial hydrostatic pressure drop between a vertically and a horizontally orientated MBR illustrated the significance of accounting for gravitational force in the vertical orientation. It was found that the pressure drop increased linearly with membrane length for the vertical SFCMBR, whereas it remained fairly constant in the horizontal. These experiments justified the development of the new models for the vertically orientated MBR's.

The hydraulic permeability of the PSu capillary membranes, used in this study, was shown to be a function of temperature. At 20°C the average permeability was found to be 9.08×10^{-11} m/Pas (2.18×10^{-17} m^2) compared to 1.43×10^{-10} m/Pas ($3.38\times10^{-17}m^2$) at 37°C.

Observations of the biofilm development showed that the biofilm thickness increased with time. The biofilm was thickest at the inlet and middle sections of the membrane and gradually decreased towards the end. Biphasic growth was observed in the growth pattern of the fungus. After 96hr of operation (following the first exponential growth phase) a second exponential growth phase was observed. The hydrostatic pressure profiles were monitored immediately after 24hr of inoculation with 3×10^{06} spores of *P. chrysosporium*. It was observed that both inlet and outlet pressures to the SFCMBR increased linearly until day 4 to day 5 of operation. After this period, a brief exponential increase in the pressure profiles was observed. This period was followed by another linear increase in the pressures. These pressure patterns were presumed to be as a result of the growth phases of the fungus.

Furthermore, it was shown that while the pH gradually decreased with biofilm development on the membrane, the redox potential increased and peaked at 218mV.

9.2 Future Work

- A nutrient volumetric flowrate of 6.20ml/hr was used in all the biofilm growth experiments of this study, however, more experiments are needed to define an optimum flowrate for enzyme production.

- A correlation is needed between the biofilm development of *P. chrysosporium* and the hydraulic permeability of the membranes.

- A means of experimentally obtaining the pressure profiles within the membrane lumen has to be developed. Only the inlet and outlet pressures to the SFCMBR could experimentally be measured. Quaile and Levy (1975) used a hot wire anemometer to experimentally obtain the velocity profiles. From such a profile, it is possible to obtain a pressure profile of the flow, and this could be used to validate the theoretical predictions.

Another alternative would be to use ultrasonic velocimeters (custom made for the size of capillary membranes used) or magnetic resonance imaging to obtain the velocity profiles, and from these profiles determine the pressure profiles.

- The developed analytical models can be broadened to include angular variation effects (i.e., the case when $m \neq 0$ in Equation 5-21).

- Finally, a commercially available CFD software package (such as CFX or Fluent) has to be used to further validate the accuracy of the developed numerical scheme.

REFERENCES

Abramowitz, M. & Stegun, I.A. (eds). 1965. *Handbook of mathematical functions*. New York: Dover.

Anderson, J.D. 1995. *Computational fluid dynamics: the basics with applications*. New York: McGraw Hill.

Apelblat, A., Katzir-Katchalsky, A. & Silberberg, A. 1974. A mathematical analysis of capillary-tissue fluid exchange. *Biorheology,* 11: 1-49.

Asenjo, J.A. & Merchuk, J.C. 1994. *Bioreactor system design*. New York: Marcel Dekker.

Belfort, G. 1989. Membranes and bioreactors: a technical challenge in biotechnology. *Biotechnology and Bioengineering,* 33: 1047-1066.

Berman, A.S. 1953. Laminar flow in channels with porous walls. *Journal of Applied Physics,* 24: 1232-1235.

Bird, R.B., Stewart, W.E. & Lightfoot, E.N. 2002. *Transport phenomena.* 2nd ed. New York: John Wiley.

Brouckaert, C.J., Wadley, S. & Hurt, Q.E. 1995. *Research on the modeling of tubular reverse osmosis systems: final report to the Water Research Commission*. Pretoria: Water Research Commission. [Water Research Commission Project no. 325/1/95].

Bruining, W.J. 1989. A general description of flows and pressures in hollow fiber membrane modules. *Chemical Engineering Science,* 44: 1441-1447.

Catapano, G., Iorio, G., Drioli, E. & Filosa, M. 1988. Experimental analysis of a cross-flow membrane bioreactor with entrapped whole cell: influence of transmembrane pressure

and substrate feed concentration on reactor performance. *Journal of Membrane Science,* 35: 325-338.

Catapano, G., Iorio, G., Drioli, E., Lombardi, C.P., Crucitti, F., Doglietto, G.B. & Bellantone, M. 1990. Theoretical and experimental analysis of a hybrid bioartificial membrane pancreas: a distributed parameter model taking into account Starling fluxes. *Journal of Membrane Science,* 52: 351-378.

CFX. 2005. *Computational fluid dynamics software and services*. http://www-waterloo.ansys.com/cfx/# [23 May 2005].

Chander, M. & Arora, D.S. 2007. Evaluation of some white-rot fungi for their potential to decolourise industrial dyes. *Dyes and Pigments,* 72: 192-198.

Chatterjee, S.G. & Belfort, G. 1986. Fluid flow in an idealized spiral wound membrane module. *Journal of Membrane Science,* 28: 191-208.

Damak, K., Ayadi., A., Zeghmati, B. & Schmitz, P. 2004. A new Navier-Stokes and Darcy's law combined model of fluid flow in crossflow filtration tubular membranes. *Desalination,* 161: 67-77.

De, S., Perkins, M. & Dutta, S.K. 2006. Nitrate reductase gene involvement in hexachlorobiphenyl dechlorination by *Phanerochaete chrysosporium*. *Journal of Hazardous Materials,* B135: 350-354

Domínguez, A., Rivela, I., Couto, R.S. & Sanromán, M.A. 2001. Design of a new rotating drum bioreactor for ligninolytic enzyme production by *Phanerochaete chrysosporium* grown on an inert support. *Process Biochemistry,* 37: 549-554.

Dhouib, A., Aloui, F., Hamad, N. & Sayadi, S. 2006. Pilot-plant treatment of olive mill wastewaters by *Phanerochaete chrysosporium* coupled to anaerobic digestion and ultrafiltration. *Process Biochemistry,* 41: 159-167.

Dzul-Puc, J.D., Esparza-Garcia, F., Barajas-Aceves, M. & Rodriguez-Vazquez, R. 2005. *Benzo[a]pyrene* removal from soil by *Phanerochaete chrysosporium* grown on sugarcane bagasse and pine sawdust. *Chemosphere,* 58: 1-7.

Elshahed, M. 2004. Blood flow in capillary under starling hypothesis. *Applied Mathematics and Computation*, 149: 431-439.

Ergun, S. 1952. Flow through packed columns. *Chemical Engineering Progress*, 48: 89-94.

Ferapontova, E., Castillo, J. & Gorton, L. 2006. Bioelectrocatalytic properties of lignin peroxidase from *Phanerochaete chrysosporium* in reactions with phenols, catechols and lignin-model compounds. *Biochimica et Biophysica Acta,* 1760: 1343-1354.

Fungal Genomics Project. 2005. *Phanerochaete chrysosporium*. https://fungalgenomics.concordia.ca/fungi/Pchr.php [19 May 2005].

Garcin, C.J. 2002. Design and manufacturing of a membrane bioreactor for the cultivation of fungi. Unpublished MSc thesis, Rhodes University, Grahamstown.

Geankoplis, C.J. 1993. *Transport processes and unit operation*. 3rd ed. New Jersey: Prentice Hall.

Godongwana, B., Sheldon, M.S. & Solomons, D.M. 2007. Momentum transfer inside a vertically orientated capillary membrane bioreactor. *Journal of Membrane Science,* 303: 86-99.

Govender, S. 2000. Optimisation studies on a membrane gradostat bioreactor for ligninase production using white rot fungi. Unpublished MTech thesis, ML Sultan Technikon, Durban.

Govender, S., Jacobs, E.P., Leukes, W.D., Odhav, B. & Pillay, V.L. 2004. Towards an optimum spore immobilisation strategy using *Phanerochaete chrysosporium*, reverse filtration and ultrafiltration membranes. *Journal of Membrane Science,* 238: 83-92.

Hai, F.I., Yamamoto, K. & Fukushi, K. 2006. Development of a submerged membrane fungi reactor for textile wastewater treatment. *Desalination,* 192: 315-322.

Hiratsuka, N., Oyadomari, M., Shinohara, H., Tanaka, H. & Wariishi, H. 2005. Metabolic mechanisms involved in hydroxylation reactions of diphenyl compounds by the lignin-degrading basidiomycete *Phanerochaete chrysosporium*. *Biochemical Engineering Journal,* 23: 241-246.

Howard, R.L., Abotsi, E., Jansen van Rensburg, E.L. & Howard, S. 2003. Lignocellulose biotechnology: issues of bioconversion and enzyme production. *Journal of Biotechnology,* 2: 602-619.

Jacobs, E.P. & Leukes, W.D. 1996. Formation of an externally unskinned polysufone capillary membrane. *Journal of Membrane Science,* 121: 149-157.

Jacobs, E.P. & Sanderson, R.D. 1997. *Capillary membrane production development: final report to the Water Research Commission by the Institute of Polymer Science*. Pretoria: Water Research Commission. [Water Research Commission Project no. 632/1/97].

JGI. 2004. *Archival data: Phanerochaete chrysosporium v1*.0. http://genome.jgi-psf.org/whiterot1/whiterot1.home.html [16 May 2005].

Kelsey, L.J., Pillarella, M.R. & Zydney, A.L. 1990. Theoretical analysis of convective flow profiles in a hollow fiber membrane bioreactor. *Chemical Engineering Science,* 45: 3211–3220.

Kirk, T.K. & Fenn, P. 1979. Formation and action of the ligninolytic system in basidiomycetes. In **Franklin, J.C., Hedger, J.N. & Swift, M.J.** (eds). 1979. *Decomposer basidiomycetes: their biology and ecology*. Cambridge: Cambridge University Press.

Kodama, T., Shimada, K & Mori, T. 1969. Studies on aerobic biphasic growth of a denitrifying bacterium, *Pseudomonas stutzeri*. *Plant Cell Physiology,* 10: 855-865.

Leukes, W.D. 1999. Development and characterisation of a membrane gradostat bioreactor for the bioremediation of aromatic pollutants using white rot fungi.Unpublished PhD thesis, Rhodes University, Grahamstown.

Liao, Z., Klein, E., Poh, C.K., Huang, Z., Lu, J., Hardy, P.A. & Gao, D. 2005. Measurement of hollow fiber membrane transport properties in hemodialyzers. *Journal of Membrane Science,* 256: 176-183.

Locatelli, F., Ronco, C. & Telta, C. (eds). 2003. Polyethersulfone: Membranes for multiple clinical applications. *Contributions to Nephrology,* 138: 1-12.

Lowry, H.V., Hayden, H.A. & Pitman, K.E. 1971. *Advanced mathematics for technical students: part three*. London: Longman Group.

Martin, W. 2000. Recovery of impregnated gold from waste mine timber through biological degradation. Unpublished MTech thesis, Cape Technikon, Cape Town.

McGrath, R. & Singleton, I. 2000. *Pentachlorophenol* transformation in soil: a toxicological assessment. *Soil Biology and Biochemistry,* 32: 1311-1314.

Meunier, J.-R. & Choder, M. 1999. *Saccharomyces cerevisiae* colony growth and ageing: biphasic growth accompanied by changes in gene expression. *Yeast,* 15: 1159-1169.

Mielgo, I., Palma, C., Guisan, J.M., Fernandez-Lafuente, R., Moreira, M.T., Feijoo, G. & Lema, J.M. 2003. Covalent immobilisation of manganese peroxidase*s* (MnP) from *Phanerochaete chrysosporium* and *Bjerkandera* sp. BOS55. *Enzyme and Microbial Technology,* 32: 769-775.

Moreira, M.T., Feijoo, G., Palma, C. & Lema, J.M. 1997. Continuous production of manganese peroxidase by *Phanerochaete chrysosporium* immobilized on polyurethane foam in a pulsed packed-bed bioreactor. *Biotechnology and Bioengineering,* 56: 130-137.

Moreira, E.A, Innocentini, M.D.M. & Coury, J.R. 2004. Permeability of ceramic foams to compressible and incompressible flow. *Journal of the European Ceramic Society,* 24: 3209-3218.

Moussy, Y. 1999. Bioartificial kidney. I. Theoretical analysis of convective flow in hollow fiber modules: application to a bioartificial hemofilter. *Biotechnology and Bioengineering*, 68: 142-152.

Moussy, Y. 2000. A model for high-pressure ultrafiltration of blood. *Biotechnology and Bioengineering,* 69(1): 21-30.

Munson, B.R., Young, D.F. & Okiishi, T.H. 2006. *Fundamentals of fluid mechanics*. 5th ed. New York: John Wiley.

Nilsson, I., Moller, A., Mattiasson, B., Rubindamayugi, M.S.T. & Welander, U. 2006. Decolorization of synthetic and real textile wastewater by the use of white-rot fungi. *Enzyme and Microbial Technology,* 38: 94-100.

Ntwampe, S.KO. 2005. Multicapillary membrane design. Unpublished MTech thesis, Cape Peninsula University of Technology, Cape Town.

Ntwampe, S.K.O. & Sheldon, M.S. 2006. Quantifying growth kinetics of *Phanerochaete chrysosporium* immobilised on a vertically orientated polysulphone capillary membrane: Biofilm development and substrate consumption. *Biochemical Engineering Journal,* 30: 147-151.

Patkar, A.Y., Koska, Y., Taylor, D.G., Bowen, B.D. & Piret, J.M. 1994. Experimental and modeling study of hollow fiber bioreactor protein distributions. *American Institute of Chemical Engineers Journal,* 5: 415-425.

Perry, R.H., Green, D.W. & Maloney, J.O. (eds). 1998. *Perry's chemical engineer's handbook*. 7th ed. New York: McGraw Hill.

Quaile, J.P. & Levy, E.K. 1975. Laminar flow in a porous tube with suction. *Transactions of the American Society of Mechanical Engineers,* 2: 66-71.

Resende, M.M., Ratusznei, S.M., Torres Suazo, C.A. & Giordano, R.C. 2002. Simulating a ceramic membrane bioreactor for the production of penicillin: an example of the importance of consistent initialization for solving DAE systems. *Process Biochemistry,* 37: 1297-1305.

Rodriguez, C.S., Rivela, I. & Sanroman, A. 2001. Design of different bioreactor configurations: application to ligninolytic enzyme production in semi-solid-state cultivation. *Journal of Chemical Technology and Biotechnology,* 76: 78-82.

Sayadi, S., Allouche, N., Jaoua, M. & Aloui, F. 2000. Detrimental effects of high molecular-mass polyphenols on olive mill wastewater biotreatment. *Process Biochemistry,* 35: 725-735.

Sharaf, M.A. & Abo-Elmagd, M. 2005. Thermal effects on CR-39 detector response and permeability of some membranes used in radon measurements. *Radiation Measurements,* 39: 441-445.

Sheldon, M.S. & Small, H.J. 2005. Immobilisation and biofilm development of *Phanerochaete chrysosporium* on polysulphone and ceramic membranes. *Journal of Membrane Science,* 263: 30-37.

Solomon, M.S. 2001. Membrane bioreactor production of lignin and manganese peroxidase. Unpublished MTech thesis, Cape Technikon, Cape Town.

Solomon, M.S. & Petersen, F.W. 2002. Membrane bioreactor production of lignin and manganese peroxidase. *Membrane Technology Newsletter,* 144: 6-8.

Spiegel, M.R. 1974. *Schaum's outline series of theory and problems of complex variables with an introduction to conformal mapping and its applications*. New York: McGraw Hill.

Taylor, D.G., Piret, J.M. & Bowen, B.D. 1994. Protein polarization in isotropic membrane hollow-fiber bioreactors. *American Institute of Chemical Engineers Journal,* 40: 321-333.

Taylor, D.G. & Boukouris, D. 1995. Influencing hollow fiber bioreactor hydrodynamics through osmotic pressures: a model study. *Chemical Engineering Science,* 50: 1513-1517.

Thakaran, J.P. & Chau, P.C. 1986. Operation and pressure distribution of immobilised cell hollow fiber bioreactors. *Biotechnology and Bioengineering,* 28: 1064–1071.

Tien, M. & Kirk, T.K. 1988. Lignin peroxidase of *Phanerochaete chrysosporium*. *Methods in Enzymology*, 16: 238-249.

Tu, S.-C., Ravindran, V. & Pirbazari, M. 2005. A pore diffusion model for forecasting the performance of membrane processes. *Journal of Membrane Science,* 265: 29-50.

Unyayar, S., Unyayar, A. & Unal, F. 2000. Production of auxin and abscisic acid by *Phanerochaete chrysosporium* ME446 immobilized on polyurethane foam. *Turkish Journal of Biology,* 24: 769-774.

Van der Plas, J.P. 1998. The adsorption mechanism of aurocyanide onto wood chips. Unpublished MTech thesis, Cape Technikon, Cape Town.

Venkatadri, R. & Irvine, R.L. 1993. Cultivation of *Phanerochaete chrysosporium* and production of lignin peroxidase in novel biofilm reactor systems: hollow fiber reactor and silicone membrane reactor. *Water Research*, 27: 591-596.

Wall, M.B., Cameron, D.C. & Lightfoot, E.N. 1993. Biopulping design and kinetics. *Biotechnology Advancements*, 11: 645-662.

Water Research Council. 2000. *Ultrafiltration capillary membrane process development for drinking water.*
http://www.fwr.org/wrcsa/965103.htm [15 April 2005].

Willershausen, H., Jager, A. & Graf, H. 1987. Ligninase production of *Phanerochaete chrysosporium* by immobilization in bioreactors. *Journal of Biotechnology,* 6: 239-243.

Wu, J. & Yu, H.-Q. 2007. Biosorption of 2,4-dichlorophenol by immobilized white-rot fungus *Phanerochaete chrysosporium* from aqueous solutions. *Bioresource Technology,* 98: 253-259.

Yuan, S.W. & Finkelstein, A.B. 1956. Laminar pipe flow with injection and suction through a porous wall. *Transactions of the American Society of Mechanical Engineers,* 78: 719-724.

Zwillinger, D. (ed). 1996. *CRC Standard mathematical tables and formulae*. 30th ed. Boca Raton: CRC Press.

APPENDIX A

ANALYTICAL SOLUTION CALCULATIONS

A.1. The generic equation

The z component of momentum transfer in cylindrical coordinates (see Appendix G), as given by the Navier-Stokes equations, in non-conservation form is:

$$\rho\left(\frac{\partial v_z}{\partial t}+v_r\frac{\partial v_z}{\partial r}+\frac{v_\theta}{r}\frac{\partial v_z}{\partial \theta}+v_z\frac{\partial v_z}{\partial z}\right)= \mu\left[\frac{1}{r}\frac{\partial}{\partial r}\left(r\frac{\partial v_z}{\partial r}\right)+\frac{1}{r^2}\frac{\partial^2 v_z}{\partial \theta^2}+\frac{\partial^2 v_z}{\partial z^2}\right]-\frac{\partial p}{\partial z}+\rho g_z \qquad \textbf{3-1}$$

This equation may be reduced by considering the fact that for small Re_w (see Appendix E) the inertial terms will be negligible (Berman, 1953; Kelsey, 1990; Moussy, 1999). The inertia-free form of Equation 3-1 is:

$$\rho\left(\frac{\partial v_z}{\partial t}\right)=\mu\left[\frac{1}{r}\frac{\partial}{\partial r}\left(r\frac{\partial v_z}{\partial r}\right)+\frac{1}{r^2}\frac{\partial^2 v_z}{\partial \theta^2}+\frac{\partial^2 v_z}{\partial z^2}\right]-\frac{\partial p}{\partial z}+\rho g_z \qquad \textbf{A 1}$$

In most viscous flows normal stress effects $\frac{\partial^2 v_z}{\partial z^2}$ are not as important as shear stresses (Anderson, 1995) and are negligible when the aspect ratio R_L/L is less than 10^{-2}, a condition that is satisfied in almost all HF and capillary membrane devices (Kelsey *et al.*, 1990). Equation A1 then simplifies to:

$$\rho\left(\frac{\partial v_z}{\partial t}\right)=\mu\left[\frac{1}{r}\frac{\partial}{\partial r}\left(r\frac{\partial v_z}{\partial r}\right)+\frac{1}{r^2}\frac{\partial^2 v_z}{\partial \theta^2}\right]-\frac{\partial p}{\partial z}+\rho g_z \qquad \textbf{A 2}$$

Equation A2 may be written in dimensionless form by introducing the following dimensionless groups:

$$U=\frac{v_z}{v_{z0}}=\frac{v_z}{(p_0-p_1)R_L^2/4\mu L} \qquad \textbf{5-2}$$

$$P=\frac{4p}{(p_0-p_1)} \qquad \textbf{5-8}$$

$$Z=\frac{z}{L} \qquad \textbf{5-9}$$

$$R = \frac{r}{R_L} \qquad \textbf{5-10}$$

$$\tau = \frac{\mu t}{\rho R_L^2} \qquad \textbf{5-11}$$

Therefore:

$$\frac{\partial U_L}{\partial \tau} = \frac{4\rho L}{(p_0 - p_1)} \frac{\partial v_z}{\partial t} \qquad \textbf{A 3}$$

$$\frac{\partial P_L}{\partial Z} = \frac{4L}{(p_0 - p_1)} \frac{\partial p_L}{\partial z} \qquad \textbf{A 4}$$

$$\frac{1}{R} \frac{\partial U_L}{\partial R} = \frac{4\mu L}{(p_0 - p_1) r} \frac{\partial v_z}{\partial r} \qquad \textbf{A 5}$$

Multiplying Equation A2 by $4L/(p_0 - p_1)$ gives:

$$\frac{4\rho L}{(p_0 - p_1)} \frac{\partial v_z}{\partial t} = \frac{4\mu L}{(p_0 - p_1)} \left[\frac{1}{r} \frac{\partial}{\partial r} \left(r \frac{\partial v_z}{\partial r} \right) + \frac{1}{r^2} \frac{\partial^2 v_z}{\partial \theta^2} \right] - \frac{4L}{(p_0 - p_1)} \frac{\partial p_L}{\partial z} + \frac{4\rho g_z L}{(p_0 - p_1)} \qquad \textbf{A 6}$$

Considering Equations A3 – A5, Equation A6 above may be rewritten in terms of the dimensionless variables as:

$$\frac{\partial U_L}{\partial \tau} = \frac{1}{R} \frac{\partial}{\partial R} \left(R \frac{\partial U_L}{\partial R} \right) + \frac{1}{R} \frac{\partial^2 U_L}{\partial \theta^2} - \left(\frac{\partial P_L}{\partial Z} - b \right) \qquad \textbf{A 7}$$

where:

$$b = \frac{4\rho g_z L}{(p_0 - p_1)} \qquad \textbf{A 8}$$

To solve for Equation A7 we make use of separable partial differential equations. This technique works by guessing the form of the solution of the partial differential equation which turns the equation into partial ordinary differential equations, which are easier to treat. The solution of A7 is assumed to be of the form:

$$U_L(R, \theta, \tau) = \Xi(R)\Theta(\theta)\mathrm{K}(\tau) \qquad \textbf{A 9}$$

Substitution of Equation A9 into A7 and dividing by $\Xi(R)\Theta(\theta)\mathrm{K}(\tau)$ gives:

$$\frac{1}{\mathrm{K}}\frac{\partial \mathrm{K}}{\partial \tau}=\frac{1}{\Xi}\frac{\partial^2 \Xi}{\partial R^2}+\frac{1}{R\Xi}\frac{\partial \Xi}{\partial R}+\frac{1}{R^2\Theta}\frac{\partial^2 \Theta}{\partial \theta^2}-\frac{G}{\Xi\Theta\mathrm{K}} \qquad \textbf{A 10}$$

where:

$$G=\left(\frac{\partial P_L}{\partial Z}-b\right) \qquad \textbf{A 11}$$

To solve Equation A10 it is necessary that the partial derivatives in this equation are with respect to only one variable, and this is done by assuming the following relations:

$$\frac{\partial^2 \Theta}{\partial \theta^2}=-m^2\Theta \qquad \textbf{A 12}$$

$$\frac{\partial \mathrm{K}}{\partial \tau}=-\alpha^2\mathrm{K} \qquad \textbf{A 13}$$

The bases of these assumptions are apparent when considering their solutions, which in their respective order are:

$$\Theta = A_1\cos m\theta + A_2 \sin m\theta \qquad \textbf{A 14}$$

$$\mathrm{K} = B_0 e^{-\alpha^2\tau} \qquad \textbf{A 15}$$

The physical meaning of Equation A14 is that the function Θ has cylindrical symmetry, because as the argument $m\theta$ approaches 2π then Θ approaches a constant value, A_1. The term $e^{-\alpha^2\tau}$ in Equation A15 is a dampening factor, and the physical significance of this term is that as τ approaches infinity the function K approaches a steady-state value, B_0. Substituting Equations A12 – A15 back into Equation A10 yields:

$$-\alpha^2=\frac{1}{\Xi}\frac{d^2\Xi}{dR^2}+\frac{1}{R\Xi}\frac{d\Xi}{dR}-\frac{m^2}{R^2}-\frac{G}{\Xi\left(A_1\cos m\theta + A_2\sin m\theta\right)B_0 e^{-\alpha^2\tau}}, \quad B_0\neq 0 \qquad \textbf{A 16}$$

Multiplying Equation A16 by $R^2\Xi$ and rearranging the terms gives:

$$R^2\frac{d^2\Xi}{dR^2}+R\frac{d\Xi}{dR}+\left(\alpha^2R^2-m^2\right)\Xi=\frac{R^2G}{\left(A_1\cos m\theta + A_2\sin m\theta\right)B_0 e^{-\alpha^2\tau}} \qquad \textbf{A 17}$$

If the R.H.S of Equation A17 is replaced with $f(Z,\theta,\tau)$, it is very interesting to note the resulting familiar Equations in Table 5-2 from Equation A17 for the different conditions listed in the table.

Table 5-2: Generic equation of flows with a low Rew through cylindrical surfaces

α	m	$f(Z,\theta,\tau)$	Resulting equation
> 0	≥ 0	= 0	Bessel's equation
= 0	> 0	> 0	Poisson's equation
= 0	> 0	= 0	Laplace's equation

A.2 Vertical SFCMBR calculations (constant shell side pressure)

A.2.1 Axial velocity inside the membrane lumen

The solutions presented here are only applicable to a system with a constant shell side hydrostatic pressure, and assume m = 0 to be the applicable condition in solving Equation A17. The independence of the function Ξ on Θ corresponds to the assumption of circular symmetry about the z-axis of the capillary membranes used (see Figure G-1 in Appendix G). In this special case Equation A17, when applied to the lumen side of the SFCMBR, reduces to:

$$\frac{1}{R}\frac{d}{dR}\left(R\frac{d\Xi_L}{dR}\right)+\left(\alpha^2\right)\Xi_L=\frac{G}{A_1\mathrm{K}} \qquad \textbf{A 18}$$

It is presumed that the system will attain a steady-state velocity U_∞ at some time τ_∞, and hence the solution of Equation A18 will be of the form:

$$\Xi=\Xi_\infty-\Xi_\tau \quad or \quad U=U_\infty-U_\tau \qquad \textbf{A 19}$$

where U_∞ and U_τ are the steady-state and transient axial velocity distributions respectively, Ξ_∞ and Ξ_τ are functions of U_∞ and U_τ respectively. Equation A18 may therefore be written as:

$$\frac{1}{R}\frac{d}{dR}\left[R\frac{d\left(\Xi_\infty-\Xi_\tau\right)}{dR}\right]+\alpha^2\left(\Xi_\infty-\Xi_\tau\right)=\frac{G}{A_1\mathrm{K}} \qquad \textbf{A 20}$$

In terms of the function Ξ, the steady-state condition Equation 5-14*b* may be written as:

$$\alpha^2\left(\Xi_\infty-\Xi_\tau\right)=\Xi_\tau=0 \qquad for \qquad \tau\geq\tau_\infty \qquad \textbf{A 21}$$

Also, since the steady-state function Ξ_∞ is not dependant on τ:

$$\alpha^2\Xi_\infty=0 \qquad for \qquad \tau_0\leq\tau\leq\tau_\infty \qquad \textbf{A 22}$$

The function Ξ_∞ can therefore be evaluated by substituting the steady-state condition A21 into Equation A20 to give:

$$\frac{1}{R}\frac{d}{dR}\left(R\frac{d\Xi_\infty}{dR}\right)=\frac{G}{A_1\mathrm{K}_\infty} \qquad \textbf{A 23}$$

Integrating Equation A23 with respect to R, assuming G is not a function of R, gives:

$$R\frac{d\Xi_\infty}{dR}=\frac{G}{A_1\mathrm{K}_\infty}\frac{R^2}{2}+C_1 \qquad \textbf{A 24}$$

C_1 is evaluated from B.C.3 (Equation 5-14*e*)

$$\therefore C_1=0 \qquad \textbf{A 25}$$

Substituting C_1 back into Equation A24 and integrating again with respect to R gives:

$$\Xi_\infty=\frac{1}{4}\frac{G}{A_1\mathrm{K}_\infty}R^2+C_2 \qquad \textbf{A 26}$$

C_2 is evaluated from B.C.2 (Equation 5-14*d*)

$$C_2=-\frac{1}{4}\frac{G}{A_1\mathrm{K}_\infty} \qquad \textbf{A 27}$$

The 'no slip' assumption of B.C.2 and B.C.9 is based on the fact that the parameter χL is 0.02 for the SFCMBR system used. Substituting C_2 back into Equation A26 gives the function of the steady-state lumenal axial velocity profile:

$$\Xi_\infty=-\frac{1}{4}\left(1-R^2\right)\frac{G}{A_1\mathrm{K}_\infty} \qquad \textbf{A 28}$$

Substituting Equations A11 and A28 into Equation A9 gives the steady-state lumenal axial velocity profile:

$$U_\infty=-\frac{1}{4}\left(1-R^2\right)\left(\frac{dP_L}{dZ}-b\right) \qquad \textbf{A 29}$$

Substituting Equations A15, A22 and A28 back into Equation A20 results in:

$$\frac{1}{R}\frac{d}{dR}\left(R\frac{d\Xi_\tau}{dR}\right)+\alpha^2\Xi_\tau=\frac{G}{A_1B_0}\left(e^{\alpha^2\tau_\infty}-e^{\alpha^2\tau}\right), \qquad B_0\neq 0 \qquad \textbf{A 30}$$

The constant A_1 can be arbitrarily put equal to unity without loss of generality. The transient velocity function Ξ_τ is finite for $\tau < \tau_\infty$, but as τ_∞ approaches infinity the function Ξ_τ is

undefined in Equation A30, therefore $\frac{G}{B_0}$ has to be zero in this equation. This condition is only met if B_0 is very large. Equation A30 then simplifies to:

$$\frac{1}{R}\frac{d}{dR}\left(R\frac{d\Xi_\tau}{dR}\right)+\alpha^2\Xi_\tau=0 \qquad \textbf{A 31}$$

Equation A31 is a special case of Bessel's equation (Equation 4-5) and therefore should have a solution of the form:

$$\Xi_\tau = B_1 J_0(\alpha R)+B_2 Y_0(\alpha R) \qquad \textbf{A 32}$$

where B_1, and B_2 are constants and J_0 and Y_0 are Bessel functions of zero order of the first kind and second kind respectively. Because the function $Y_0(\alpha R)$ tends to minus infinity as R goes to zero, B_2 in A32 has to be zero. Imposing the 'no slip condition' Equation 5-14d, the axial lumenal velocity U_L should be equal to zero at $R = 1$, Ξ must therefore also vanish at $R = 1$. Since B_1 cannot be set equal to zero without obtaining the trivial solution $\Xi_\tau = 0$, the Bessel function $J_0(\alpha R)$ must be set equal to zero:

$$\therefore J_0(\alpha R)=0 \qquad \textbf{A 33}$$

But Equation A33 has an infinite number of roots α (often called eigenvalues) which will satisfy the boundary conditions of Equation A32. The first three of these roots are $\alpha_1 = 2.405$, $\alpha_2 = 5.520$, $\alpha_3 = 8.654$, etc (see Appendix F). Hence, there are many solutions $\Xi_\tau = B_{1n} J_0(\alpha_n R)$ with $n = 1,2,3,\ldots\infty$, which will satisfy Equation A31 and the corresponding boundary conditions. Substituting Equations A15 and A32 into Equation A9, and considering the above arguments results in the following expression for U_τ:

$$U_\tau(R,\tau)=\sum_{n=1}^{\infty} B_n e^{-\alpha_n^2\tau} J_0(\alpha_n R) \qquad \textbf{A 34}$$

where:

$$B_n = B_0 B_{1n} \qquad \textbf{A 35}$$

The initial condition, Equation 5-14a stipulates that at $\tau = 0$, $U_\tau = U_\infty$, therefore:

$$-\frac{1}{4}(1-R^2)\left(\frac{dP_L}{dZ}-b\right)=\sum_{n=1}^{\infty} B_n J_0(\alpha_n R) \qquad \textbf{A 36}$$

Equation A36, in which a known function is expressed as a linear combination of Bessel functions, is called a Fourier-Bessel series. The constant B_n in the Fourier-Bessel series is evaluated by multiplying Equation A36 by $J_0(\alpha_m R)R$ and integrating from 0 to 1:

$$-\frac{1}{4}\left(\frac{dP_L}{dZ}-b\right)\int_0^1 J_0(\alpha_m R)(1-R^2)RdR = \int_0^1 J_0(\alpha_m R)R\left\{\sum_{n=1}^{\infty} B_n J_0(\alpha_n R)\right\}dR \qquad \textbf{A 37}$$

On the assumption that the integral and summation signs may be interchanged, Equation A37 becomes:

$$-\frac{1}{4}\left(\frac{dP_L}{dZ}-b\right)\int_0^1 J_0(\alpha_m R)(1-R^2)RdR = \sum_{n=1}^{\infty} B_n \int_0^1 J_0(\alpha_n R)J_0(\alpha_m R)RdR \qquad \textbf{A 38}$$

The L.H.S of Equation A38 is evaluated by making use of the property of Bessel functions in Equation 4-15:

$$\therefore -\frac{1}{4}\left(\frac{dP_L}{dZ}-b\right)\int_0^1 J_0(\alpha_m R)(1-R^2)RdR = \frac{1}{4}\left(\frac{dP_L}{dZ}-b\right)\left(\frac{4}{\alpha_m^3}\right)J_0'(\alpha_m) \qquad \textbf{A 39}$$

Equation A39 may further be simplified by considering the property of Bessel functions in Equation 4-12:

$$\frac{1}{4}\left(\frac{dP_L}{dZ}-b\right)\left(\frac{4}{\alpha_m^3}\right)J_0'(\alpha_m) = -\frac{1}{4}\left(\frac{dP_L}{dZ}-b\right)\left(\frac{4}{\alpha_m^3}\right)J_1(\alpha_m) \qquad \textbf{A 40}$$

The integral on the R.H.S of Equation A38 may be evaluated with the help of the Lommel integrals:

$$\int_0^x J_n(\alpha_l r)J_n(\alpha_m r)rdr = 0, \qquad (l \neq m) \qquad \textbf{4-16}$$

and,

$$\int_0^x rJ_n^2(\alpha_m r)dr = \frac{x^2}{2}\left[J_n'(\alpha_m x)^2 + \left(1-\frac{n^2}{\alpha_m^2 x^2}\right)J_n^2(\alpha_m x)\right] \qquad \textbf{4-14}$$

where $J_n'(\alpha_m x)$ is the derivative of $J_n(\alpha_m x)$. Equation 4-16 shows that the Bessel functions of the first kind of integer order form an orthogonal set with respect to the eigenvalues α_m, α_l on the interval $0< r <x$. The importance of this property in evaluating the R.H.S of Equation A38 is that the only term that contributes (in the summation term) is that for which $m = n$. The R.H.S of Equation A38 then becomes:

$$\therefore B_m \int_0^1 J_0^2(\alpha_m R) R dR = \frac{B_m}{2}\left[J_0'(\alpha_m)^2 + J_0^2(\alpha_m)\right] \qquad \textbf{A 41}$$

Making use of the property of Bessel functions in Equation 4-12, Equation A41 then becomes:

$$\therefore B_m \int_0^1 J_0^2(\alpha_m R) R dR = \frac{B_m}{2}\left[J_1^2(\alpha_m) + J_0^2(\alpha_m)\right] \qquad \textbf{A 42}$$

However, from Equation A33, the eigenvalues α_m are such that $J_0(\alpha_m) = 0$. Accordingly the last term on the R.H.S of Equation A42 is zero. Substituting Equations A40 and A42 in the L.H.S and R.H.S of Equation A38 respectively, results in the following expression for B_m:

$$B_m = -\frac{2}{\alpha_m^3 J_1(\alpha_m)}\left(\frac{dP_L}{dZ} - b\right) \qquad \textbf{A 43}$$

Substituting B_m into Equation A34 gives:

$$U_\tau = -2\left[\sum_{n=1}^{\infty} \frac{J_0(\alpha_n R)}{\alpha_n^3 J_1(\alpha_n)} e^{-\alpha_n^2 \tau}\right]\left(\frac{dP_L}{dZ} - b\right) \qquad \textbf{A 44}$$

Substituting the solutions of both the steady-state and transient axial velocity distributions, Equations A28 and A44, back into Equation A19 gives:

$$U_L(Z, R, \tau) = -\frac{1}{4}\left[\left(1 - R^2\right) - 8\sum_{n=1}^{\infty} \frac{J_0(\alpha_n R)}{\alpha_n^3 J_1(\alpha_n)} e^{-\alpha_n^2 \tau}\right]\left(\frac{dP_L}{dZ} - b\right) \qquad \textbf{A 45}$$

Equation A45 is an expression for the lumenal axial velocity distribution as a function of the axial and radial spatial coordinates as well as time.

The method used above in solving the linear partial differential equations (using the method of separation of variables and superposition of solutions) is often referred to as Fourier's method.

A.2.2 Radial velocity inside the membrane lumen

The continuity equation in cylindrical coordinates is given by:

$$\frac{\partial \rho}{\partial t} = -\left[\frac{1}{r}\frac{\partial(\rho r v_r)}{\partial r} + \frac{1}{r}\frac{\partial(\rho v_\theta)}{\partial \theta} + \frac{\partial(\rho v_z)}{\partial z}\right] \qquad \textbf{3-4}$$

When considering two-dimensional flow of constant density (i.e. $\frac{\partial \rho}{\partial t} = 0$) Equation 3-4 becomes:

$$\frac{1}{r}\frac{\partial(rv_r)}{\partial r} = -\frac{\partial(v_z)}{\partial z} \qquad \textbf{A 46}$$

Introducing a dimensionless radial velocity V_L:

$$V = \frac{v_r}{v_{z0}} = \frac{v_r}{(p_0 - p_1)R_L^2 / 4\mu L} \qquad \textbf{5-3}$$

Equation A46 may be rewritten in dimensionless form as:

$$\frac{1}{R}\frac{\partial(RV_L)}{\partial R} = -\frac{\partial U_L}{\partial Z} \qquad \textbf{A 47}$$

The R.H.S. of Equation A47 may be evaluated from Equation A45 as:

$$\frac{\partial U_L}{\partial Z} = -\frac{1}{4}\frac{\partial\left[\left[\left(1-R^2\right) - 8\sum_{n=1}^{\infty}\frac{J_0(\alpha_n R)}{\alpha_n^3 J_1(\alpha_n)}e^{-\alpha_n^2\tau}\right]\left(\frac{dP_L}{dZ} - b\right)\right]}{\partial Z} \qquad \textbf{A 48}$$

$$\therefore \frac{\partial U_L}{\partial Z} = -\frac{1}{4}\left[\left(1-R^2\right) - 8\sum_{n=1}^{\infty}\frac{J_0(\alpha_n R)}{\alpha_n^3 J_1(\alpha_n)}e^{-\alpha_n^2\tau}\right]\frac{d^2P_L}{dZ^2} \qquad \textbf{A 49}$$

Substituting Equation A49 into A47 and integrating with respect to *R*, making use of the property of Bessel functions in Equation 4-13, gives:

$$RV_L = \frac{1}{4}\left[\frac{R^2}{2}\left(1-\frac{R^2}{2}\right) - 8\sum_{n=1}^{\infty}\frac{RJ_1(\alpha_n R)}{\alpha_n^4 J_1(\alpha_n)}e^{-\alpha_n^2\tau}\right]\frac{d^2P_L}{dZ^2} + C_3 \qquad \textbf{A 50}$$

C_3 is evaluated from B.C.4 (Equation 5-14*f*)

$$\therefore C_3 = 0 \qquad \textbf{A 51}$$

Substituting C_3 back into Equation A50 gives:

$$V_L = \frac{1}{4}\left[\frac{R}{2}\left(1-\frac{R^2}{2}\right) - 8\sum_{n=1}^{\infty}\frac{J_1(\alpha_n R)}{\alpha_n^4 J_1(\alpha_n)}e^{-\alpha_n^2\tau}\right]\frac{d^2P_L}{dZ^2} \qquad \textbf{A 52}$$

A.2.3 Velocity through the matrix

The volumetric flux through the matrix of the membrane is given by Equation 3-13:

$$J = -\frac{\left(\frac{1}{k_m}+\frac{1}{k_g}+\frac{1}{k_{in}}\right)^{-1}}{\mu}\left[\frac{(p_S+\Phi)-p_L}{(d_w+d_g+d_{in})}-\rho g\right] \qquad \textbf{3-13}$$

Pore fouling, which is an irreversible process caused by the deposition and adsorption of solutes to the membrane pores, will not be considered in this analysis and therefore Equation 3-13 reduces to:

$$J = -\frac{(k_m.k_g)}{\mu}\left[\frac{(p_S+\Phi)-p_L}{(d_w+d_g)}-\rho g\right] \qquad \textbf{A 53}$$

Since the volumetric flux J is the same as the matrix velocity v_M, Equation A53 may be written in dimensionless form by introducing the following dimensionless groups:

$$\Pi = \frac{4\Phi}{(p_0-p_1)} \qquad \textbf{5-7}$$

$$P = \frac{4p}{(p_0-p_1)} \qquad \textbf{5-8}$$

$$\kappa = \frac{L\left(\frac{1}{k_m}+\frac{1}{k_g}\right)^{-1}}{R_L^2(d_w+d_g)} \qquad \textbf{5-12}$$

and

$$V_M = \frac{v_M}{(p_0-p_1)R_L^2/4\mu L} \qquad \textbf{A 54}$$

Considering Equations 5-7, 5-8, 5-12 and A54, Equation A53 may be written in terms of the dimensionless variables as:

$$V_M = -\kappa[P_{Sb\pi}-P_L] \qquad \textbf{A 55}$$

where:

$$P_{Sb\pi} = P_S+\Pi-\left(\frac{d_w+d_g}{L}\right)b \qquad \textbf{A 56}$$

A.2.4 Volumetric flowrate in the lumen

To evaluate the volumetric flowrate in the lumen Q_L of the SFCMBR, it is necessary to consider the flow as passing through a differential area $dA = (2\pi r)dr$, in which case:

$$dQ_L = v_z(2\pi r)dr \qquad \textbf{A 57}$$

and therefore:

$$Q_L = 2\pi \int_0^{R_L} v_z r dr \qquad \textbf{A 58}$$

The dimensionless form of Equation A58 is:

$$\Omega_L = 4\int_0^1 U_L R dR \qquad \textbf{A 59}$$

Substituting Equation A45 in Equation A59 and integrating between the limits 0 and 1 results in the following expression for the lumenal volumetric flowrate:

$$\Omega_L = -\left(\frac{1}{4} - 8\sum_{n=1}^{\infty} \frac{e^{-\alpha_n^2 \tau}}{\alpha_n^4}\right)\left(\frac{dP_L}{dZ} - b\right) \qquad \textbf{A 60}$$

A.2.5 Pressure profiles in the membrane lumen

To solve for the lumenal pressure profile P_L in Equation A55 we make use of B.C.5, and this substitution results in:

$$\frac{d^2 P_L}{dZ^2} - 16\kappa P_L = -16\kappa P_{Sb\pi} \qquad \textbf{A 61}$$

By assuming that the pressure profile will not be a function of the radial spatial coordinate the partial derivative expression can be written as a total derivative expression. Equation A61 is a simple ordinary differential equation (O.D.E) and may be solved using Laplace transforms with B.C.6, and has a solution of the form:

$$P_L(Z) = (P_0 - P_{Sb\pi})\cosh\left(4\sqrt{\kappa}\right)Z + \frac{a}{4\sqrt{\kappa}}\sinh\left(4\sqrt{\kappa}\right)Z + P_{Sb\pi} \qquad \textbf{A 62}$$

$$\therefore \frac{dP_L}{dZ} = 4\sqrt{\kappa}(P_0 - P_{Sb\pi})\sinh\left(4\sqrt{\kappa}\right)Z + a\cosh\left(4\sqrt{\kappa}\right)Z \qquad \textbf{A 63}$$

Defining a fraction retentate at steady-state as (Bruining, 1989):

$$f = \frac{U_{L(1)}}{U_{L(0)}} \qquad \textbf{A 64}$$

The transient-state axial velocity profile given by Equation A45, simplifies at steady-state and at $Z = 0$ to:

$$U_L(0, R, \tau_\infty) = -\frac{1}{4}\left(1 - R^2\right)\left(\frac{dP_{L(0)}}{dZ} - b\right) \qquad \textbf{A 65}$$

where:

$$\frac{dP_{L(0)}}{dZ} = a \qquad \textbf{A 66}$$

Similarly at steady-state and at $Z = 1$, Equation A45 simplifies to:

$$U_L(1, R, \tau_\infty) = -\frac{1}{4}\left(1 - R^2\right)\left[\frac{dP_{L(1)}}{dZ} - b\right] \qquad \textbf{A 67}$$

where:

$$\frac{dP_{L(1)}}{dZ} = 4\sqrt{\kappa}\left(P_0 - P_{Sb\pi}\right)\sinh\left(4\sqrt{\kappa}\right) + a\cosh\left(4\sqrt{\kappa}\right) \qquad \textbf{A 68}$$

$$\therefore U_L(1) = -\frac{1}{4}\left(1 - R^2\right)\left[4\sqrt{\kappa}\left(P_0 - P_{Sb\pi}\right)\sinh\left(4\sqrt{\kappa}\right) + a\cosh\left(4\sqrt{\kappa}\right) - b\right] \qquad \textbf{A 69}$$

Substituting Equations A65 and A69 into Equation A64 gives:

$$a = \frac{4\sqrt{\kappa}\left(P_0 - P_{Sb\pi}\right)\sinh\left(4\sqrt{\kappa}\right)}{\left[f - \cosh\left(4\sqrt{\kappa}\right)\right]} - \frac{b\left(1 - f\right)}{\left[f - \cosh\left(4\sqrt{\kappa}\right)\right]} \qquad \textbf{A 70}$$

A.2.6 Axial velocity on the shell-side of the membrane

The treatment for the axial velocity profile on the shell-side is identical to that of the lumenal axial velocity profile; only the mathematics is more involving. Since the pressure is constant along the length of the membrane on the shell-side of the SFCMBR:

$$\frac{dP_S}{dZ} = 0 \qquad \textbf{A 71}$$

the expression for G in Equation A17 reduces to:

$$G = -b \qquad \textbf{A 72}$$

The steady-state shell axial velocity profile $U_S(R, \tau_\infty)$ is then given by:

$$\frac{1}{R}\frac{\partial}{\partial R}\left(R\frac{\partial U_S}{\partial R}\right) = -b \qquad \textbf{A 73}$$

Integrating Equation A73 with respect to R and making use of B.C.8 gives:

$$R\frac{\partial U_S}{\partial R} = \frac{b}{2}\left(R_2^2 - R^2\right) \qquad \textbf{A 74}$$

integrating Equation A74 again with respect to R and making use of B.C.9 to solve for the integration constant results in:

$$U_S(R, \tau_\infty) = \frac{b}{4}\left[2R_2^2 \ln\frac{R}{R_3} + R_3^2 - R^2\right] \qquad \textbf{A 75}$$

The transient-state axial velocity profile is obtained using Fourier's method as before (and some standard integrals of Bessel functions in Appendix F) to give:

$$U_S(R, \tau) = \sum_{n=1}^{\infty} B_n e^{-\alpha_n^2 \tau} J_0(\alpha_n R) \qquad \textbf{A 76}$$

and B_n is given by:

$$B_n = -\frac{2}{J_1^2(\alpha_n)}\left\{\frac{R_2^2}{2}\left(\frac{1}{2}\ln R_3 + \frac{1}{4}\right)J_0(\alpha_n) + \frac{R_2^2}{4\alpha_n^2}\left[\alpha_n\left(\frac{1}{2\Gamma(2)} - J_1(\alpha_n)\right) + \left(\ln R_3 + \frac{1}{2}\right)J_2(\alpha_n)\right] - \frac{J_1(\alpha_n)}{\alpha_n^3}\right\} \qquad \textbf{A 77}$$

Substituting the solutions of both the steady-state and transient axial velocity profiles, Equations A75 and A76, into Equation A19 gives:

$$U_S = \frac{b}{4}\left\{\left[2R_2^2 \ln\frac{R}{R_3} + R_3^2 - R^2\right] - 4\sum_{n=1}^{\infty} B_n e^{-\alpha_n^2 \tau} J_0(\alpha_n R)\right\} \qquad \textbf{A 78}$$

There is no radial velocity on the shell-side of the membrane for a constant shell side pressure SFCMBR:

$$\therefore V_S = 0 \qquad \textbf{A 79}$$

A.2.7 Volumetric flowrate in the shell side

Following the same argument as for the lumenal flowrate, the shell side volumetric flowrate Q_S is evaluated from the expression:

$$\Omega_S = 4\int_0^1 U_S R dR \qquad \textbf{A 80}$$

Substituting Equation A78 in Equation A80 and integrating between the limits 0 and 1 results in the following expression for the lumenal volumetric flowrate:

$$\Omega_S = -b\left\{\left[R_2^2\left(\ln R_3 + \frac{1}{2}\right) - \frac{R_3^2}{2} + \frac{1}{4}\right] + \frac{4}{\alpha_n b}\sum_{n=1}^{\infty} B_n e^{-\alpha_n^2\tau} J_1(\alpha_n)\right\} \qquad \textbf{A 81}$$

A.3 Horizontal SFCMBR calculations (constant shell side pressure)

As in the case of the vertical SFCMBR, the starting point is the Navier-Stokes equation but this time assuming gravitational acceleration effects will be negligible (i.e. $\rho g_z = 0$). The treatment is exactly the same as for the vertical SFCMBR and the resulting mathematical expressions then become for: the dimensionless axial velocity profile in the lumen side, U_L:

$$U_L(Z,R,\tau) = -\frac{1}{4}\left[\left(1-R^2\right) - 8\sum_{n=1}^{\infty}\frac{J_0(\alpha_n R)}{\alpha_n^3 J_1(\alpha_n)} e^{-\alpha_n^2\tau}\right]\frac{dP_L}{dZ} \qquad \textbf{A 82}$$

the velocity in the lumen side, V_L, is the same as in the vertical orientated SFCMBR:

$$V_L = \frac{1}{4}\left[\frac{R}{2}\left(1-\frac{R^2}{2}\right) - 8\sum_{n=1}^{\infty}\frac{J_1(\alpha_n R)}{\alpha_n^4 J_1(\alpha_n)} e^{-\alpha_n^2\tau}\right]\frac{d^2 P_L}{dZ^2} \qquad \textbf{A 52}$$

the velocity profile through the matrix, V_M, is

$$V_M = -\kappa\left[P_{S\pi} - P_L\right] \qquad \textbf{A 83}$$

where:

$$P_{S\pi} = P_S + \Pi \qquad \textbf{A 84}$$

and the pressure profile inside the lumen of the membrane bioreactor:

$$P_L(Z) = (P_0 - P_{S\pi})\cosh\left(4\sqrt{\kappa}\right)Z + \frac{a}{4\sqrt{\kappa}}\sinh\left(4\sqrt{\kappa}\right)Z + P_{S\pi} \qquad \textbf{A 85}$$

where:

$$a = \frac{4\sqrt{\kappa}(P_0 - P_{S\pi})\sinh\left(4\sqrt{\kappa}\right)}{\left[f - \cosh\left(4\sqrt{\kappa}\right)\right]} \qquad \textbf{A 86}$$

There is neither radial nor axial shell flow for the constant shell pressure horizontal SFCMBR:

$$V_S = U_S = 0 \qquad \textbf{A 87}$$

A.4 Stream function for vertical SFCMBR (constant shell side pressure)

A.4.1 Stream functions for the membrane lumen

A stream function is defined such that:

$$U = -\frac{1}{R}\frac{\partial \psi}{\partial R} \qquad \textbf{A 88}$$

and

$$V = \frac{1}{R}\frac{\partial \psi}{\partial Z} \qquad \textbf{A 89}$$

Substituting Equation A45 into Equation A88 and integrating with respect to R between the limits 0 and 1 gives:

$$\psi_L(Z,\tau) = \frac{1}{4}\left[\frac{1}{2} - 8\sum_{n=1}^{\infty}\frac{e^{-\alpha_n^2\tau}}{\alpha_n^4}\right]\left(\frac{dP_L}{dZ} - b\right) \qquad \textbf{A 90}$$

Similarly, the substitution of Equation A52 into Equation A89 results in:

$$\psi_L(R,\tau) = \frac{1}{4}\left[\frac{R^2}{2}\left(1 - \frac{R^2}{2}\right) - 8\sum_{n=1}^{\infty}\frac{RJ_1(\alpha_n R)e^{-\alpha_n^2\tau}}{\alpha_n^4 J_1(\alpha_n)}\right]\left(\frac{dP_{L(1)}}{dZ} - \frac{dP_{L(0)}}{dZ}\right) \qquad \textbf{A 91}$$

The equation of the stream function is obtained by combining Equations A90 and A91:

$$\psi_L(R,Z,\tau)=\frac{1}{4}\left\{\left[\frac{1}{2}-8\sum_{n=1}^{\infty}\frac{e^{-\alpha_n^2\tau}}{\alpha_n^4}\right]\left(\frac{dP_L}{dZ}-b\right)+\left[\frac{R^2}{2}\left(1-\frac{R^2}{2}\right)-8\sum_{n=1}^{\infty}\frac{RJ_1(\alpha_n R)e^{-\alpha_n^2\tau}}{\alpha_n^4 J_1(\alpha_n)}\right]\left(\frac{dP_{L(1)}}{dZ}-\frac{dP_{L(0)}}{dZ}\right)\right\}$$

A 92

At steady state (i.e., at $\tau=\tau_\infty$), Equation A92 reduces to:

$$\psi_L=\frac{1}{4}\left\{\frac{1}{2}\left(\frac{dP_L}{dZ}-b\right)+\left[\frac{R^2}{2}\left(1-\frac{R^2}{2}\right)\right]\left(\frac{dP_{L(1)}}{dZ}-\frac{dP_{L(0)}}{dZ}\right)\right\}$$

A 93

A.4.2 Stream functions for the membrane shell

Substituting A75 into Equation A88 and integrating with respect to *R* between the limits R_2 and R_3 gives:

$$\psi_S(Z,\tau_\infty)=\frac{R_2^2}{4}\left[\ln(R_3-R_2)-\ln R_3\right]\left(R_3^2-R_2^2\right)-\frac{R_2^2}{8}\left(R_3^2-R_2^2\right)+\frac{R_3^2}{8}\left(R_3^2-R_2^2\right)-\frac{\left(R_3^4-R_2^4\right)}{16}$$

A 94

Substituting V_S into Equation A89 and integrating with respect to *Z* between the limits 0 and 1 results in:

$$\psi_S(R,\tau_\infty)=0$$

A 95

The equation of the stream function is obtained by combining Equations A94 and A95:

$$\psi_S=-b\left\{\frac{R_2^2}{4}\left[\ln(R_3-R_2)-\ln R_3\right]\left(R_3^2-R_2^2\right)-\frac{R_2^2}{8}\left(R_3^2-R_2^2\right)+\frac{R_3^2}{8}\left(R_3^2-R_2^2\right)-\frac{\left(R_3^4-R_2^4\right)}{16}\right\}$$

A 96

A.5 Vertical SFCMBR calculations (variable shell side pressure)

A.5.1 Axial and radial velocities inside the membrane lumen

The treatment and the solutions for the lumenal flow profiles is exactly the same as for a constant shell-side pressure SFCMBR:

$$U_L(Z,R,\tau)=-\frac{1}{4}\left[\left(1-R^2\right)-8\sum_{n=1}^{\infty}\frac{J_0(\alpha_n R)}{\alpha_n^3 J_1(\alpha_n)}e^{-\alpha_n^2\tau}\right]\left(\frac{dP_L}{dZ}-b\right)$$

A 45

$$V_L = \frac{1}{4}\left[\frac{R}{2}\left(1-\frac{R^2}{2}\right)-8\sum_{n=1}^{\infty}\frac{J_1(\alpha_n R)}{\alpha_n^4 J_1(\alpha_n)}e^{-\alpha_n^2\tau}\right]\frac{d^2P_L}{dZ^2} \qquad \textbf{A 52}$$

$$\Omega_L = -\left(\frac{1}{4}-8\sum_{n=1}^{\infty}\frac{e^{-\alpha_n^2\tau}}{\alpha_n^4}\right)\left(\frac{dP_L}{dZ}-b\right) \qquad \textbf{A 60}$$

A.5.2 Axial velocity on the membrane shell

The steady-state Navier-Stokes equations, neglecting the inertial terms and considering only two-dimensional flow, when applied in the shell of the membrane bioreactor simplify to:

$$\mu\left[\frac{1}{r}\frac{\partial}{\partial r}\left(r\frac{\partial v_{zS}}{\partial r}\right)\right] = \frac{\partial p_S}{\partial z} - \rho g_z \qquad \textbf{A 97}$$

In dimensionless form this equation becomes

$$\frac{1}{R}\frac{\partial}{\partial R}\left(R\frac{\partial U_S}{\partial R}\right) = \frac{\partial P_S}{\partial Z} - b \qquad \textbf{A 98}$$

Integrating the above equation with respect to R and assuming P_S not to be a function of R, gives:

$$\left(\frac{dP_S}{dZ}-b\right)\frac{R^2}{2} = R\frac{dU_S}{dR} + C_4 \qquad \textbf{A 99}$$

C_4 is evaluated from B.C.8

$$C_4 = \left(\frac{dP_S}{dZ}-b\right)\frac{R_2^2}{2} \qquad \textbf{A 100}$$

Substituting C_4 back into Equation A99 gives:

$$\frac{1}{2}\left(\frac{dP_S}{dZ}-b\right)\left(R^2-R_2^2\right) = R\frac{dU_S}{dR} \qquad \textbf{A 101}$$

Integrating this equation again with respect to R and making use of B.C.9 to solve for the integration constant yields:

$$U_S(R,\tau_\infty) = \frac{1}{4}\left(R^2 - R_3^2 - 2R_2^2\ln\frac{R}{R_3}\right)\left(\frac{dP_S}{dZ}-b\right) \qquad \textbf{A 102}$$

The method of obtaining the transient-state axial shell velocity profile was described in Section A.2.6. the only difference, however, is that:

$$\frac{dP_S}{dZ} \neq 0 \qquad \textbf{A 103}$$

Equation A78 then becomes:

$$U_S(Z,R,\tau) = -\left\{\frac{1}{4}\left[2R_2^2 \ln\frac{R}{R_3} + R_3^2 - R^2\right] - \sum_{n=1}^{\infty} B_n e^{-\alpha_n^2\tau} J_0(\alpha_n R)\right\}\left(\frac{dP_S}{dZ} - b\right) \qquad \textbf{A 104}$$

where:

$$B_n = -\frac{2}{J_1^2(\alpha_n)}\left\{\frac{R_2^2}{2}\left(\frac{1}{2}\ln R_3 + \frac{1}{4}\right)J_0(\alpha_n) + \frac{R_2^2}{4\alpha_n^2}\left[\alpha_n\left(\frac{1}{2\Gamma(2)} - J_1(\alpha_n)\right) + \left(\ln R_3 + \frac{1}{2}\right)J_2(\alpha_n)\right] - \frac{J_1(\alpha_n)}{\alpha_n^3}\right\} \qquad \textbf{A 105}$$

A.5.3 Radial velocity on the membrane shell

The shell radial velocity profile can be obtained by making use of the axial profile in conjunction with the continuity equation:

$$\frac{1}{R}\frac{\partial(RV_S)}{\partial R} = -\frac{\partial U_S}{\partial Z} \qquad \textbf{A 106}$$

and

$$\frac{dU_S}{dZ} = \frac{1}{4}\left(R^2 - R_3^2 - 2R_2^2 \ln\frac{R}{R_3}\right)\frac{d^2P_S}{dZ^2} \qquad \textbf{A 107}$$

Substituting Equation A107 in Equation A106 and integrating gives:

$$RV_S = -\frac{1}{4}\frac{d^2P_S}{dZ^2}\left[\frac{R^4}{4} - \frac{R^2}{2}R_3^2 - 2R_2^2\left(\frac{R^2}{2}\ln\frac{R}{R_3} - \frac{R^2}{4}\right)\right] + C_5 \qquad \textbf{A 108}$$

C_5 is evaluated from B.C.10

$$C_5 = \frac{1}{4}\frac{d^2P_S}{dZ^2}\left[\frac{R_2^4}{4} - \frac{R_2^2}{2}R_3^2 - 2R_2^2\left(\frac{R_2^2}{2}\ln\frac{R_2}{R_3} - \frac{R_2^2}{4}\right)\right] \qquad \textbf{A 109}$$

Substituting C_5 back into Equation A108 gives:

$$V_S = \frac{1}{16R}\left[R_2^4 - R^4 - 2R_3^2\left(R_2^2 - R^2\right) - 8R_2^2\left[\left(\frac{R_2^2}{2}\ln\frac{R_2}{R_3} - \frac{R_2^2}{4}\right) - \left(\frac{R^2}{2}\ln\frac{R}{R_3} - \frac{R^2}{4}\right)\right]\right]\frac{d^2P_S}{dZ^2}$$

A 110

A.5.4 Pressure profiles in the membrane shell

Recalling B.C.11 (i.e. at $R = R_x$, $V_M = V_S$):

$$\therefore -\kappa\left(P_{Sb\pi} - P_L\right) = \frac{1}{16R_x}\left[R_2^4 - R_x^4 - 2R_3^2\left(R_2^2 - R_x^2\right) - 8R_2^2\left[\left(\frac{R_2^2}{2}\ln\frac{R_2}{R_3} - \frac{R_2^2}{4}\right) - \left(\frac{R_x^2}{2}\ln\frac{R_x}{R_3} - \frac{R_x^2}{4}\right)\right]\right]\frac{d^2P_S}{dZ^2}$$

A 111

If we substitute:

$$f\left(R_x\right) = \left[R_2^4 - R_x^4 - 2R_3^2\left(R_2^2 - R_x^2\right) - 8R_2^2\left[\left(\frac{R_2^2}{2}\ln\frac{R_2}{R_3} - \frac{R_2^2}{4}\right) - \left(\frac{R_x^2}{2}\ln\frac{R_x}{R_3} - \frac{R_x^2}{4}\right)\right]\right]$$

A 112

Then Equation A111 becomes:

$$\frac{d^2P_S}{dZ^2} + \frac{16\kappa R_x}{f\left(R_x\right)}P_{Sb\pi} - \frac{16\kappa R_x}{f\left(R_x\right)}P_L = 0$$

A 113

Equation A113 combined with Equation A61, with the corresponding boundary and initial conditions, are all that is required to solve for the pressure field on the lumen and shell sides of the membrane.

$$\frac{d^2P_L}{dZ^2} - 16\kappa P_L = -16\kappa P_{Sb\pi}$$

A 61

Combining Equation A113 with Equation A61 gives:

$$\frac{d^2P_S}{dZ^2} = \frac{R_x}{f\left(R_x\right)}\frac{d^2P_L}{dZ^2}$$

A 114

Taking the second derivative of Equation A113 results in

$$\frac{d^4P_S}{dZ^4} + \frac{16\kappa R_x}{f\left(R_x\right)}\frac{d^2P_S}{dZ^2} - \frac{16\kappa R_x}{f\left(R_x\right)}\frac{d^2P_L}{dZ^2} = 0$$

A 115

Substituting Equation A114 in Equation in A115 gives

$$\frac{d^4P_S}{dZ^4} - 16\kappa\left[\frac{f(R_x)-R_x}{f(R_x)}\right]\frac{d^2P_S}{dZ^2} = 0 \qquad \textbf{A 116}$$

Then if we replace the function of R_x with

$$\omega^2 = 16\kappa\left[\frac{f(R_x)-R_x}{f(R_x)}\right]\frac{d^2P_S}{dZ^2} \qquad \textbf{A 117}$$

$$\therefore \frac{d^4P_S}{dZ^4} - \omega^2\frac{d^2P_S}{dZ^2} = 0 \qquad \textbf{A 118}$$

This is a simple O.D.E. if we resolve it by making $Y = \frac{d^2P_S}{dZ^2}$ in Equation A118 to obtain:

$$\frac{d^2Y}{dZ^2} - \omega^2 Y = 0 \qquad \textbf{A 119}$$

From Equation A114 it can be seen that if the second and third derivatives of the lumenal pressure at entrance to the membrane are $\frac{d^2P_{L(0)}}{dZ^2} = A$ and $\frac{d^3P_{L(0)}}{dZ^3} = B$, then the corresponding second and third derivatives of the shell-side pressure at the point of entrance will be $\frac{d^2P_{S(0)}}{dZ^2} = \frac{R_xA}{f(R_x)}$ and $\frac{d^3P_{S(0)}}{dZ^3} = \frac{R_xB}{f(R_x)}$ respectively.

$$Y_{(0)} = \frac{R_xA}{f(R_x)} \qquad \textbf{A 120}$$

and

$$Y'_{(0)} = \frac{R_xB}{f(R_x)} \qquad \textbf{A 121}$$

If we make use of Equations A120 and A121 as initial conditions to solve Equation A119 the result is:

$$Y = \frac{AR_x\cosh\omega Z}{f(R_x)} + \frac{BR_x\sinh\omega Z}{\omega f(R_x)} \qquad \textbf{A 122}$$

Recalling that $Y = \frac{d^2P_S}{dZ^2}$

$$\therefore \frac{d^2 P_S}{dZ^2} = \frac{AR_x \cosh \omega Z}{f(R_x)} + \frac{BR_x \sinh \omega Z}{\omega f(R_x)} \qquad \textbf{A 123}$$

Integrating Equation A123 twice with respect to Z gives:

$$P_S = \frac{AR_x \cosh \omega Z}{\omega^2 f(R_x)} + \frac{BR_x \sinh \omega Z}{\omega^3 f(R_x)} + H_g Z + D \qquad \textbf{A 124}$$

where H_g and D are integration constants. The corresponding lumenal pressure profile is given by:

$$P_L = \frac{A \cosh \omega Z}{\omega^2} + \frac{B \sinh \omega Z}{\omega^3} + H_g Z + D \qquad \textbf{A 125}$$

H_g is evaluated from B.C.7

$$H_g = b + \frac{BR_x}{\omega^2 f(R_x)} \qquad \textbf{A 126}$$

Recalling the definition of the fraction retentate

$$f = \frac{U_{L(1)}}{U_{L(0)}} \qquad \textbf{A 64}$$

and noting that the lumenal velocity profiles on the SFCMBR with a variable pressure on the shell side will still be given by the same expressions (as for a constant shell pressure SFCMBR):

$$U_L(0, R, \tau_\infty) = -\frac{1}{4}(1 - R^2)\left(\frac{dP_{L(0)}}{dZ} - b\right) \qquad \textbf{A 65}$$

$$U_L(1, R, \tau_\infty) = -\frac{1}{4}(1 - R^2)\left[\frac{dP_{L(1)}}{dZ} - b\right] \qquad \textbf{A 67}$$

Equation A64 then becomes:

$$-\frac{1}{4}(1 - R^2)\left(\frac{A}{\omega}\sinh \omega + \frac{B}{\omega^2}\cosh \omega + H_g - b\right) = -\frac{1}{4} f (1 - R^2)\left(\frac{B}{\omega^2} + H_g - b\right) \qquad \textbf{A 127}$$

$$\therefore A = \frac{B}{\omega \sinh \omega}(f - \cosh \omega) + \frac{\omega(C - b)}{\sinh \omega}(f - 1) \qquad \textbf{A 128}$$

We have so far two equations (Equation A126 and Equation A128) and 4 unknowns (A, B, D, and H_g). The two other equations necessary to solve for the unknowns arise from B.C.7

$$\therefore \frac{A}{\omega^2} + D = P_{L(0)} \qquad \textbf{A 129}$$

$$\frac{A}{\omega^2}\frac{R_x}{f(R_x)} + D = P_{S(0)} \qquad \textbf{A 130}$$

Solving the 4 equations simultaneously results in:

$$A = \frac{\omega^2 f(R_x)\left(P_{L(0)} - P_{S(0)}\right)}{\left[f(R_x) - R_x\right]} \qquad \textbf{A 131}$$

$$B = \frac{\omega^3 f(R_x)^2\left(P_{L(0)} - P_{S(0)}\right)\sinh\omega}{\left[f(R_x) - R_x\right]\left[f(R_x)(f - \cosh\omega) + R_x(f-1)\right]} \qquad \textbf{A 132}$$

$$H_g = b + \frac{\omega R_x f(R_x)\left(P_{L(0)} - P_{S(0)}\right)\sinh\omega}{\left[f(R_x) - R_x\right]\left[f(R_x)(f - \cosh\omega) + R_x(f-1)\right]} \qquad \textbf{A 133}$$

$$D = P_{L(0)} - \frac{f(R_x)\left(P_{L(0)} - P_{S(0)}\right)}{\left[f(R_x) - R_x\right]} \qquad \textbf{A 134}$$

A.6 Horizontal SFCMBR calculations (variable shell side pressure)

The treatment is exactly the same as for the vertical SFCMBR with variable shell side pressure, neglecting the gravitational acceleration terms. The lumenal profiles are therefore given by:

$$U_L(Z,R,\tau) = -\frac{1}{4}\left[\left(1-R^2\right) - 8\sum_{n=1}^{\infty}\frac{J_0(\alpha_n R)}{\alpha_n^3 J_1(\alpha_n)}e^{-\alpha_n^2\tau}\right]\frac{dP_L}{dZ} \qquad \textbf{A 82}$$

$$V_L = \frac{1}{4}\left[\frac{R}{2}\left(1-\frac{R^2}{2}\right) - 8\sum_{n=1}^{\infty}\frac{J_1(\alpha_n R)}{\alpha_n^4 J_1(\alpha_n)}e^{-\alpha_n^2\tau}\right]\frac{d^2P_L}{dZ^2} \qquad \textbf{A 52}$$

The resulting mathematical expressions then become for: the dimensionless axial velocity profile in the shell, U_S:

$$U_S = -\frac{1}{4}\left\{\left[2R_2^2\ln\frac{R}{R_3} + R_3^2 - R^2\right] - 4\sum_{n=1}^{\infty}B_n e^{-\alpha_n^2\tau}J_0(\alpha_n R)\right\}\frac{dP_S}{dZ} \qquad \textbf{A 135}$$

V_S is the same as in the vertical orientated SFCMBR:

$$V_S = \frac{1}{16R}\left[R_2^4 - R^4 - 2R_3^2\left(R_2^2 - R^2\right) - 8R_2^2\left[\left(\frac{R_2^2}{2}\ln\frac{R_2}{R_3} - \frac{R_2^2}{4}\right) - \left(\frac{R^2}{2}\ln\frac{R}{R_3} - \frac{R^2}{4}\right)\right]\right]\frac{d^2P_S}{dZ^2}$$

A 110

the velocity profile through the matrix, V_M, is

$$V_M = -\kappa\left(P_{S\pi} - P_L\right)$$

A 136

the pressure profile inside the lumen of the membrane bioreactor:

$$P_L = \frac{A\cosh\omega Z}{\omega^2} + \frac{B\sinh\omega Z}{\omega^3} + HZ + D$$

A 137

and the pressure profile in the shell side of the membrane:

$$P_S = \frac{AR_x\cosh\omega Z}{\omega^2 f\left(R_x\right)} + \frac{BR_x\sinh\omega Z}{\omega^3 f\left(R_x\right)} + HZ + D$$

A 138

where:

$$A = \frac{\omega^2 f\left(R_x\right)\left(P_{L(0)} - P_{S(0)}\right)}{\left[f\left(R_x\right) - R_x\right]}$$

A 131

$$B = \frac{\omega^3 f\left(R_x\right)^2\left(P_{L(0)} - P_{S(0)}\right)\sinh\omega}{\left[f\left(R_x\right) - R_x\right]\left[f\left(R_x\right)\left(f - \cosh\omega\right) + R_x\left(f - 1\right)\right]}$$

A 132

$$D = P_{L(0)} - \frac{f\left(R_x\right)\left(P_{L(0)} - P_{S(0)}\right)}{\left[f\left(R_x\right) - R_x\right]}$$

A 134

$$H = \frac{\omega R_x f\left(R_x\right)\left(P_{L(0)} - P_{S(0)}\right)\sinh\omega}{\left[f\left(R_x\right) - R_x\right]\left[f\left(R_x\right)\left(f - \cosh\omega\right) + R_x\left(f - 1\right)\right]}$$

A 139

A.7 Stream function for vertical SFCMBR (variable shell side pressure)

The stream function in the lumen of the variable shell side pressure SFCMBR is the same as for the constant shell side pressure SFCMBR, and is given by:

$$\psi_L = \frac{1}{4}\left\{\frac{1}{2}\left(\frac{dP_L}{dZ} - b\right) + \left[\frac{R^2}{2}\left(1 - \frac{R^2}{2}\right)\right]\left(\frac{dP_{L(1)}}{dZ} - \frac{dP_{L(0)}}{dZ}\right)\right\}$$

A 93

The stream function in the shell is obtained by substituting Equation A102 into Equation A88 and integrating with respect to R between the limits R_2 and R_3 to give:

$$\psi_S(Z,\tau_\infty)=\left\{\frac{R_2^2}{4}\left[\ln(R_3-R_2)-\ln R_3\right]\left(R_3^2-R_2^2\right)-\frac{R_2^2}{8}\left(R_3^2-R_2^2\right)+\frac{R_3^2}{8}\left(R_3^2-R_2^2\right)-\frac{\left(R_3^4-R_2^4\right)}{16}\right\}\left(\frac{dP_S}{dZ}-b\right)$$

A 140

Substituting Equation A110 into Equation A89 and integrating with respect to Z between the limits 0 and 1 results in:

$$\psi_S(R,\tau_\infty)=\frac{1}{16}\left\{R_2^4-R^4-2R_3^2\left(R_2^2-R^2\right)-8R_2^2\left[\left(\frac{R_2^2}{2}\ln\frac{R_2}{R_3}-\frac{R_2^2}{4}\right)-\left(\frac{R^2}{2}\ln\frac{R}{R_3}-\frac{R^2}{4}\right)\right]\right\}\left(\frac{dP_{S(1)}}{dZ}-\frac{dP_{S(0)}}{dZ}\right)$$

A 141

The equation of the stream function is obtained by combining Equations A140 and A141:

$$\psi_S=\frac{1}{16}\left\{R_2^4-R^4-2R_3^2\left(R_2^2-R^2\right)-8R_2^2\left[\left(\frac{R_2^2}{2}\ln\frac{R_2}{R_3}-\frac{R_2^2}{4}\right)-\left(\frac{R^2}{2}\ln\frac{R}{R_3}-\frac{R^2}{4}\right)\right]\right\}\left(\frac{dP_{S(1)}}{dZ}-\frac{dP_{S(0)}}{dZ}\right)$$
$$+\left(\frac{dP_S}{dZ}-b\right)\varpi$$

A 142

where:

$$\varpi=\frac{R_2^2}{4}\left[\ln(R_3-R_2)-\ln R_3\right]\left(R_3^2-R_2^2\right)-\frac{R_2^2}{8}\left(R_3^2-R_2^2\right)+\frac{R_3^2}{8}\left(R_3^2-R_2^2\right)-\frac{\left(R_3^4-R_2^4\right)}{16}$$ **A 143**

APPENDIX B

NUMERICAL SCHEME CALCULATIONS

B.1 Axial velocity profile

The starting point is the *z*-component of the Navier-Stokes equation in cylindrical coordinates (in non-conservation form).

$$\rho\left(\frac{\partial v_z}{\partial t}+v_r\frac{\partial v_z}{\partial r}+\frac{v_\theta}{r}\frac{\partial v_z}{\partial \theta}+v_z\frac{\partial v_z}{\partial z}\right)= \mu\left[\frac{1}{r}\frac{\partial}{\partial r}\left(r\frac{\partial v_z}{\partial r}\right)+\frac{1}{r^2}\frac{\partial^2 v_z}{\partial \theta^2}+\frac{\partial^2 v_z}{\partial z^2}\right]-\frac{\partial p}{\partial z}+\rho g_z \qquad \textbf{3-1}$$

The dimensionless variables are the same as for the analytical solutions in Appendix A, there is however one additional parameter and that is the aspect ratio, β:

$$\beta=\frac{R_L}{L} \qquad \textbf{B 1}$$

Multiplying Equation 3-1 by $\frac{R_L^2}{\mu v_{z0}}$ and ignoring angular variations, i.e., $v_\theta=\frac{\partial}{\partial\theta}=0$ gives:

$$\frac{\rho R_L^2}{\mu v_{z0}}\frac{\partial v_z}{\partial t}+\frac{\rho R_L^2}{\mu v_{z0}}\left[v_r\frac{\partial v_z}{\partial r}+v_z\frac{\partial v_z}{\partial z}\right]=\frac{R_L^2}{v_{z0}}\left[\frac{1}{r}\frac{\partial}{\partial r}\left(r\frac{\partial v_z}{\partial r}\right)+\frac{\partial^2 v_z}{\partial z^2}\right]-\frac{R_L^2}{\mu v_{z0}}\frac{\partial P}{\partial z}+\frac{\rho R_L^2 g_z}{\mu v_{z0}} \qquad \textbf{B 2}$$

Defining Re_b as:

$$\mathrm{Re}_b=\frac{\rho v_{z0}R_L}{\mu} \qquad \textbf{B 3}$$

Equation B2 above can be written in dimensionless form as:

$$\frac{\partial U}{\partial \tau}+\mathrm{Re}_b\left(V\frac{\partial U}{\partial R}+\beta U\frac{\partial U}{\partial Z}\right)=\frac{1}{R}\frac{\partial}{\partial R}\left(R\frac{\partial U}{\partial R}\right)+\beta^2\frac{\partial^2 U}{\partial Z^2}-\beta\frac{\partial P}{\partial Z}+b \qquad \textbf{B 4}$$

Equation B4 will be discretized by forward differencing the time derivative and pressure terms and central differencing the spatial derivatives:

$$\therefore\frac{\partial U}{\partial \tau}=\frac{U_{i,j}^{n+1}-U_{i,j}^{n}}{\Delta\tau} \qquad \textbf{B 5}$$

$$V\frac{\partial U}{\partial R}=V_{i,j}^{n}\frac{U_{i,j+1}^{n}-U_{i,j-1}^{n}}{2\Delta R} \qquad \textbf{B 6}$$

$$U\frac{\partial U}{\partial Z}=U_{i,j}^{n}\frac{U_{i+1,j}^{n}-U_{i-1,j}^{n}}{2\Delta Z} \qquad \textbf{B 7}$$

$$\frac{\partial^2 U}{\partial Z^2}=\frac{U_{i+1,j}^{n}-2U_{i,j}^{n}+U_{i-1,j}^{n}}{\Delta Z^2} \qquad \textbf{B 8}$$

And

$$\frac{\partial P}{\partial Z}=\frac{P_{i+1,j}^{n}-P_{i,j}^{n}}{\Delta Z} \qquad \textbf{B 9}$$

Equation B4 then becomes:

$$\frac{U_{i,j}^{n+1}-U_{i,j}^{n}}{\Delta\tau}+\mathrm{Re}_b\left(V_{i,j}^{n}\frac{U_{i,j+1}^{n}-U_{i,j-1}^{n}}{2\Delta R}+\beta U_{i,j}^{n}\frac{U_{i+1,j}^{n}-U_{i-1,j}^{n}}{2\Delta Z}\right)=\frac{1}{R}\frac{U_{i,j+1}^{n}-U_{i,j-1}^{n}}{2\Delta R}$$
$$+\frac{U_{i,j+1}^{n}-2U_{i,j}^{n}+U_{i,j-1}^{n}}{\Delta R^2}+\beta^2\frac{U_{i+1,j}^{n}-2U_{i,j}^{n}+U_{i-1,j}^{n}}{\Delta Z^2}-\beta\frac{P_{i+1,j}^{n}-P_{i,j}^{n}}{\Delta Z}+b \qquad \textbf{B 10}$$

The superscript *n* in Equations B5 – B9 above is referred to as the running index for the marching variable, τ in this case. The velocity profile given by Equation B10 is solved in steps of time and the progressive time steps are represented by *n*, *n*+1, *n*+2, *n*+3 …

B.2. Radial velocity profile

The solution of the radial profile is extracted from the *r*-component of the Navier-Stokes equation in cylindrical coordinates (in non-conservation form):

$$\rho\left(\frac{\partial v_r}{\partial t}+v_r\frac{\partial v_r}{\partial r}+\frac{v_\theta}{r}\frac{\partial v_r}{\partial\theta}-\frac{v_\theta^2}{r}+v_z\frac{\partial v_r}{\partial z}\right)=$$
$$\mu\left[\frac{1}{r}\frac{\partial}{\partial r}\left(r\frac{\partial v_r}{\partial r}\right)-\frac{v_r}{r^2}+\frac{1}{r^2}\frac{\partial^2 v_r}{\partial\theta^2}-\frac{2}{r^2}\frac{\partial v_\theta}{\partial\theta}+\frac{\partial^2 v_r}{\partial z^2}\right]-\frac{\partial p}{\partial r}+\rho g_r \qquad \textbf{3-2}$$

The treatment is exactly the same as for the axial profile. Equation 3-2 in dimensionless form becomes:

$$\frac{\partial V}{\partial\tau}+\mathrm{Re}_b\left(V\frac{\partial V}{\partial R}+\beta U\frac{\partial V}{\partial Z}\right)=\frac{1}{R}\frac{\partial}{\partial R}\left(R\frac{\partial V}{\partial R}\right)-\frac{V}{R^2}+\beta^2\frac{\partial^2 V}{\partial Z^2}-\frac{\partial P}{\partial R} \qquad \textbf{B 11}$$

and the resulting finite-difference quotient is:

$$\frac{V_{i,j}^{n+1}-V_{i,j}^{n}}{\Delta\tau}+\mathrm{Re}_b\left(V_{i,j}^{n}\,\frac{V_{i,j+1}^{n}-V_{i,j-1}^{n}}{2\Delta R}+\beta U_{i,j}^{n}\,\frac{V_{i+1,j}^{n}-V_{i-1,j}^{n}}{2\Delta Z}\right)=\frac{1}{R}\,\frac{V_{i,j+1}^{n}-V_{i,j-1}^{n}}{2\Delta R}+\frac{V_{i,j+1}^{n}-2V_{i,j}^{n}+V_{i,j-1}^{n}}{\Delta R^{2}}$$

$$-\frac{V_{i,j}^{n}}{R^{2}}+\beta^{2}\,\frac{V_{i+1,j}^{n}-2V_{i,j}^{n}+V_{i-1,j}^{n}}{\Delta Z^{2}}-\frac{P_{i,j+1}^{n}-P_{i,j}^{n}}{\Delta R}$$

B 12

APPENDIX C

GROWTH AND MAINTENANCE OF THE FUNGUS

C.1 Spore Inducing Medium (Tien & Kirk, 1988)

Cultures of *P. chrysosporium* strain BKMK-1767 (ATCC 24725) were maintained on supplemented malt agar slants. To prepare the spore-inducing medium for the cultures, the following procedure was followed. The ingredients listed below were added in the order into a 1000 ml bottle:

Glucose	10g
Malt extract	10g
Peptone	2g
Yeast extract	2g
Asparagine	1g
KH_2PO_4	2g
$MgSO_4.7H_2O$	1g
Thiamin-HCl	1mg
Agar-agar	20g

The mixture was filled up to the 1L mark with distilled water, and stirred to dissolve the powder. When the powder was completely dissolved, the bottle was covered with tinfoil to prevent contamination and autoclaved for 20 minutes at 121°C to ensure sufficient sterilization. After removing from the autoclave, the mixture was allowed to cool to a workable temperature, under a laminar flow hood. The Agar solution was then cast into Petri dishes.

C.2 Casting of the Agar

The casting of the Agar was done under a laminar flow hood using the flaming technique (flame after opening and before closing the bottle). Each Petri dish was filled with the still hot agar to a thickness of about 1 cm. The Agar flask outlet was flamed before and after the agar was poured into a Petri dish to avoid any possible transferred contamination. The lids were left slightly open

for a short while to prevent moisture forming (condensation) underneath the lids. After the Agar was cooled down sufficiently, it became stiff with a consistency of jelly. This was followed by the inoculation of *P. chrysosporium* spores on the Petri dishes.

C.3 Inoculation of *P. chrysosporium* onto Petri dishes

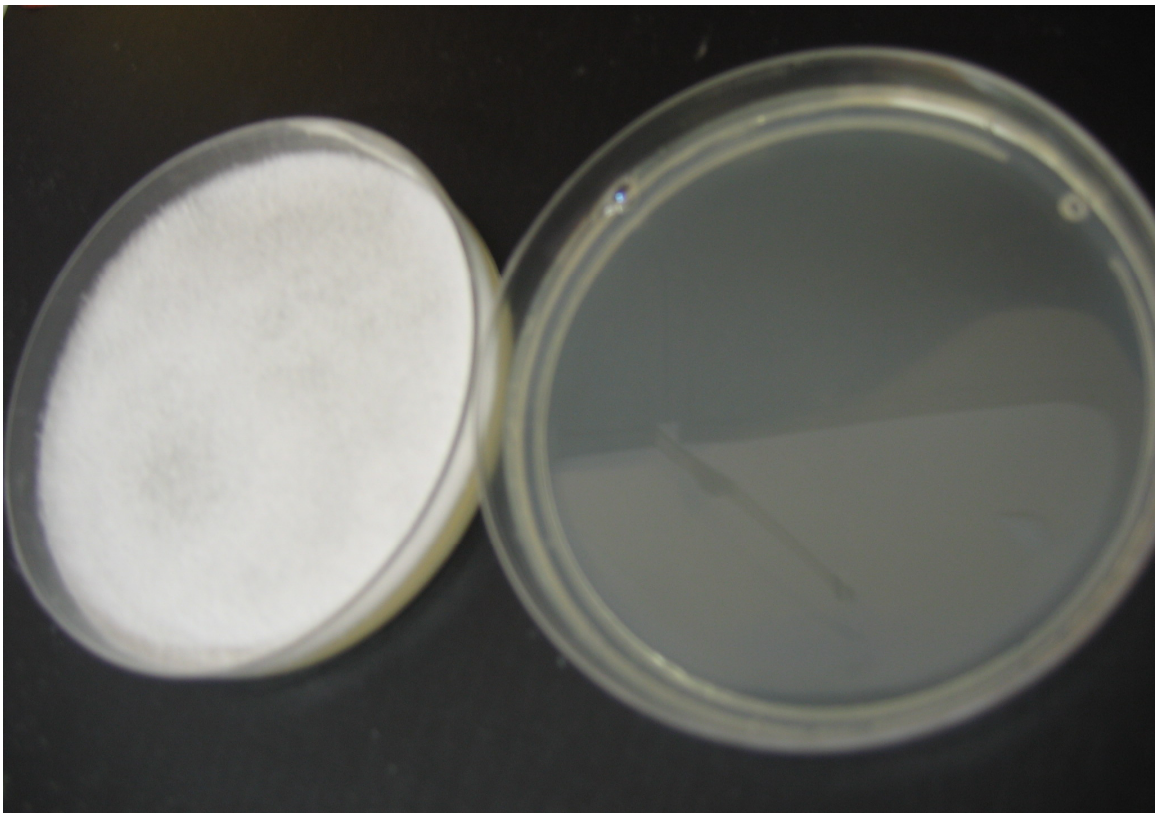

Figure C- 1: A comparison of a Petri dish with growth and one without growth

The inoculation of the spores was done under an operating laminar flow hood and a clean surface sterilized thoroughly with 70% alcohol. A platinum rod was used as the tool to transfer spores. The platinum rod was flamed under a Bunsen burner and cooled down before dipping it into the fresh agar located on the rim of the Petri dish. A square piece (about 1 cm) of the inoculation culture was cut out and placed in the middle of the fresh Petri dish. The dish was sealed with Parafilim M (Pechiney, USA), before it was stored upside down in an incubator at 37 °C, until there was visible growth of the spores as shown (on the left plate) in Figure C- 1.

C.4 Spore solution preparation

The following equipment was autoclaved;

- 1000 ml distilled water in a schott bottle
- 60 ml syringe with glass wool
- 250 ml flask
- 100 ml schott bottles

5 ml of cooled sterile distilled water was poured into each Petri dish containing spores and mycelium, under sterile conditions. The dish lid was closed and the water shaken in rotational movements for about a minute, to ensure that all spores were in solution. The washing solution was transferred from the Petri dishes into a sterile 100 ml bottle, this was repeated three to four times on one agar slant. This procedure was continued until there was enough spore solution. This solution was in fact a spore/mycelium solution, which needed to be separated.

C.5 Separation of spores from mycelium

A heat sterilized (autoclaved) syringe with glass wool was used to separate the spores from the mycelium solution. The solution was filtered through a 0.22μm filter into a 250 ml flask.

C.6 Determination of spore purity and concentration

C.6.1 Spore purity

Under sterile conditions, a small drop of spore solution was placed onto a slide and covered with a cover slip to be observed under a light microscope at ×100 magnification. Undamaged, uniform oval spores with a small size distribution and no or very few visible mycelium pieces should be observed.

C.6.2 Spore concentration

The spore solution concentration was determined by measuring absorbance at 650 nm with a

spectrophotometer. The spectrophotometer was 'blanked' by using distilled water, that is, the concentration of the spore solution was measured against that of distilled water. An absorbance of 1.0 cm^{-1} is approximately 5 x 10^6 spores/ml (Tien and Kirk, 1988).

APPENDIX D

PREPARATION OF THE NUTRIENT SOLUTION

D.1 Trace element stock solution

Dissolve 1.5 g Nitrilotriacetate in 800ml distilled water. Trace element solution is a light yellow colour. After dissolving the Nitrilotriacetate completely, adjust the pH to 6.5 with 1M KOH (28g/500ml). Add each of the following components sequentially:

$MgSO_4$	3g	(6.14 g $MgSO_4*7H_2O$)
$MnSO_4$	0.5g	(0.56 g $MnSO_4*H_2O$)
NaCl	1g	
$FeSO_4.7H_2O$	0.1g	
$CoCl_2$	0.1g	(0.187 g $CoCl_2*6\ H_2O$)
$ZnSO_4.7H_2O$	0.1g	
$CuSO_4$	0.1g	
$AlK(SO_4)_2.12H_2O$	10mg	(0.01g)
H_3BO_3	10mg	(0.01g)
$Na_2MoO_4.2H_2O$	10mg	(0.01g)

Make up to 1L with autoclaved distilled water. Filter sterilise the solution into an autoclaved bottle using a 0.22 μm filter (do not autoclave).

D.2 Basal III medium stock solution

KH_2PO_4	20g	
$MgSO_4$	5g	(10.23 mg $MgSO_4.7H_2O$)
$CaCl_2$	1g	(1.32 g $CaCl_2*2\ H_2O$)
Trace element solution	100ml	(see D1 above)

Make up to 1L with autoclaved distilled water. Filter sterilise through a 0.22µm filter into a sterile bottle and store at 4°C (do not autoclave).

D.3 10% Glucose stock solution

Glucose 100g

Make up to 1L with autoclaved distilled water. Autoclave for 20 minutes and store at 4°C.

D.4 0.1 M 2,2-dimethylsuccinate stock solution (pH 4.2)

2,2-dimethylsuccinate 13.045ml in 1L autoclaved distilled water.

Autoclave for 20 minutes and store at 4°C. A sodium acetate buffer can also be used as an alternative when large amounts of medium are required.

D.5 Thiamin-HCl

Thiamin-HCl 100mg/L stock

Filter sterilise through a 0.22µm filter into a sterile bottle and store at 4° (do not autoclave).

D.6 Ammonium tartrate

Ammonium tartrate 8g

Make up to 1L with autoclaved distilled water. Autoclave for 20 minutes and store at 4°C.

D.7 0.02M Veratryl alcohol

Veratryl alcohol 2.907ml in 1L

Filter sterilise through a 0.22µm filter into a sterile bottle and store at 4°C (do not autoclave). Store in a dark place when not in use (veratryl acohol is light sensitive).

D.8 Nutrient solution make-up

Table D- 1: Nutrient solution make-up

Component	Volume (ml)	% of total volume	Chemical Formula
Basal 3 medium	100.00	10.00	…
10% Glucose stock solution	100.00	10.00	$C_6H_{12}O_6$
0.1 M 2,2 Dimethylsuccinate	100.00	10.00	$C_6H_{10}O_4$
Thiamin	10.00	1.00	$C_{12}H_{17}ClN_4OS \bullet HCl$
Ammonium tartrate	25.00	2.50	$C_4H_{12}N_2O_6$
0.02 M veratryl alcohol	100.00	10.00	$C_9H_{12}O_3$
Trace elements	60.00	6.00	…
Distilled water	505.00	50.5	H_2O

The make-up of the final nutrient solution is a combination of the above components in the proportions listed in Table D- 1.

APPENDIX E

AUXILIARY CALCULATIONS

E.1 Hydraulic permeability of the membrane

The Forchheimer equation with the proposed correlation by Ergun (1952) was used to estimate the hydraulic permeability k_m of the membranes. This model was used because it was difficult to determine k_m experimentally when there was growth on the surface of the membrane. To determine the accuracy of the Forchheimer model in predicting values of k_m, model prediction values were compared to experimentally determined values at 20°C and at 30°C when there was no growth on the surface of the membrane. The experimental values are presented in Table E- 1.

Table E- 1: Properties of the polysulphone membrane and water at 293K and 310K

(K)	$\mu_{water} \times 10^3$ (Pa.s)	ρ_{water} (kg/m^3)	d_{pore} (m)	d_w (m)	$k_{m(\text{experimental})}$ (m^2)	r_o (m)	r_i (m)
293	0.8937	998	0.000011	0.0002475	2.18×10^{-17}	0.0009625	0.0006625
310	0.682	994	0.000011	0.0002475	3.38×10^{-17}	0.0009625	0.0006625

The Forchheimer equation was introduced in Section 3.3.3 as

$$\frac{\Delta p}{d_w} = \frac{\mu}{k_1} J + \frac{\rho}{k_2} J^2 \qquad \textbf{3-18}$$

where k_1 (m^2) and k_2 (m) are referred to as Darcyan and non-Darcyan permeability parameters respectively, and k_1 represents the membrane hydraulic permeability k_m. Ergun (1952) proposed the following expressions for k_1 and k_2, for granular beds (which are assumed to be applicable to the polysulphone membrane):

$$k_1 = \frac{\varepsilon^3 d_{pore}^2}{150(1-\varepsilon)^2} \qquad \textbf{3-19}$$

$$k_2 = \frac{\varepsilon^3 d_{pore}}{1.75(1-\varepsilon)} \qquad \textbf{3-20}$$

The average inlet and outlet pressures p_0 and p_1 at a permeate volume flux of 8.53×10^{-7}m/s are respectively 130.67kPa and 122.66kPa for the 55cm membrane bioreactor operated at 20°C.

Substituting these values into Equation 3-18 with the water properties specified in Table E- 1 gives:

$$3.23\times10^{7} = \frac{7.63\times10^{-10}}{k_1} + \frac{7.27\times10^{-10}}{k_2} \qquad \textbf{E 1}$$

Both unknowns k_1 and k_2 in Equation E1 are functions of the surface porosity ε, and can be obtained by varying values of ε until the right hand side equals the left hand side in Equation E1. This operation is easily executed by the Microsoft solver® algorithm. The resulting porosity is 0.03 and the corresponding values of k_1 and k_2 at 20°C are $2.36\times10^{-17}m^2$ and $1.78\times10^{-10}m$ respectively. The values of k_1 and k_2 were predicted using this method for a 23.3cm membrane, a 29cm membrane, and a 55cm membrane. The average value of the membrane hydraulic permeability k_1 of the 3 membrane lengths was found to be $3.93\times10^{-17}m^2$ which compares well with the experimental value of $2.18\times10^{-17}m^2$. The Forchheimer equation predicts a k_1 value of $4.68\times10^{-17}m^2$ at 37°C and the experimental value is $3.38\times10^{-17}m^2$.

E.2 Schmidt Number of the nutrient solution

Table E- 2: Atomic volumes (Geankoplis, 1993)

Element	Atomic volume (m^3/gmol)	Element	Atomic volume (m^3/gmol)
C	0.0148	*N*	0.0156
H	0.0037	*Cl*	0.0216
O	0.0074	*S*	0.0256

The Schmidt number *Sc* of a solution is given by Equation 5-1:

$$Sc = \frac{\mu}{\rho D_{AB}} \qquad \textbf{5-1}$$

and the diffusivity D_{AB} for solutes with a molecular weight less than 1000g/mol is given by the Wilke-Chang equation (Geankoplis, 1993):

$$D_{AB} = 1.173\times10^{-16}\left(\varphi M_B\right)^{1/2}\frac{T}{\mu_B V_A^{0.6}} \qquad \textbf{E 2}$$

where φ is an association parameter and has a value of 2.6 when water is the solvent, M_B is the molecular weight of the solvent in g/mol, V_A is the solute molar volume at its normal boiling

point in m^3/gmol, and T is the solution final temperature in K. The solute molar volume V_A is calculated from the chemical formula by making use of the atomic volumes in Table E- 2.

The molar volume of Glucose is calculated from the chemical formula as follows

$$Glu\cos e \rightarrow C_6H_{12}O_6$$
$$V_{(Glu\cos e)} = 6(0.0148)+12(0.0037)+6(0.0074)$$
$$V_{(Glu\cos e)} = 0.1776 m^3 / gmol$$

The overall molar volume V_A is the sum of the individual molar volumes of the components of the nutrient solution:

$$V_A = 0.1V_{(Glu\cos e)} + 0.1V_{(Dimethylsuccinate)} + 0.01V_{(Thia\min)} + 0.025V_{(Ammonium\,tartrate)} + 0.1V_{(Verylalcohol)} \quad \textbf{E 3}$$

The viscosity of water μ_B at 37°C (310K) is 0.000682Pa.s (Geankoplis, 1993), and its molecular weight M_B is 18.02g/mol. The Wilke-Chang equation predicts diffusivities with a mean deviation of 20% for aqueous solutions. The corrected diffusivity D_{AB} therefore is 1.594×10^{-09}m^2/s. The viscosity of the nutrient solution at 37°C is 1.18×10^{-03} Pas. Taking the density ρ of the nutrient solution as that of water at 37°C (i.e. 994kg/m^3), the Sc of the solution is given by:

$$Sc = \frac{1.18\times10^{-03}}{994.0\times1.594\times10^{-09}} = 744.7$$

E.3 Wall Reynolds Number of the nutrient solution

The wall Reynolds Re_w number is defined as

$$\mathrm{Re}_w = \frac{\rho v_w r_H}{\mu} \quad \textbf{E 4}$$

where r_H is the hydraulic radius of the membrane $r_o - r_i$ in m, ρ is the density of the nutrient solution in kg/m^3 taken as that of water at 37°C (see Table E- 1), and μ is the dynamic viscosity of the solution at the same temperature (0.00118Pa.s). The wall velocity v_w is defined as

$$v_w = -\frac{(k_m.k_g)}{\mu}\left[\frac{(p_S+\Phi)-p_L}{(d_w+d_g)}-\rho g\right] \quad \textbf{E 5}$$

where Φ is the osmotic pressure due to the solutes on the surface of the membrane lumen in Pa, p_S is the hydrostatic pressure on the shell side of the membrane in Pa, p_L is the hydrostatic pressure on the lumen side of the membrane, and d_w is the membrane wall thickness in m, k_g is the hydraulic permeability of the gel layer in m^2 (equal to 0 for a clogged membrane and equal to 1 for a clean membrane), and d_g is the gel layer thickness in m. The osmotic pressure Φ is obtained from the solute concentrations by making use of Equation 3-17:

$$\Phi = \sum_{i=1}^{n} \omega_i c_{wi} R^* T \qquad \textbf{3-17}$$

For the model parameters listed in Table 7-1 the Re_w was found to be:

$$\mathrm{Re}_w = \frac{994 \times 1.24 \times 10^{-06} \left(0.0009625 - 0006625\right)}{0.00118} = 3.133 \times 10^{-04}$$

The Re_w is well below 1 and therefore the assumptions of similarity in the velocity profiles and negligible inertial contributions are justified.

APPENDIX F

BESSEL FUNCTIONS

F.1 Bessel's differential equation (Zwillinger, 1996)

Bessel's differential equation is:

$$x^2u'' + xu' + \left(x^2 - \upsilon^2\right)u = 0 \qquad \upsilon \geq 0 \qquad \textbf{F 1}$$

The solutions of Equation F1 are denoted with the functions $J_\upsilon(x)$ and $Y_\upsilon(x)$, which are referred to as ordinary Bessel functions:

$$u = c_1 J_\upsilon(x) + c_2 Y_\upsilon(x) \qquad \textbf{F 2}$$

When υ is an integer, the following relation exists:

$$J_{-n}(x) = (-1)^n J_n(x), \qquad n = 0, 1, 2, 3, \ldots \qquad \textbf{F 3}$$

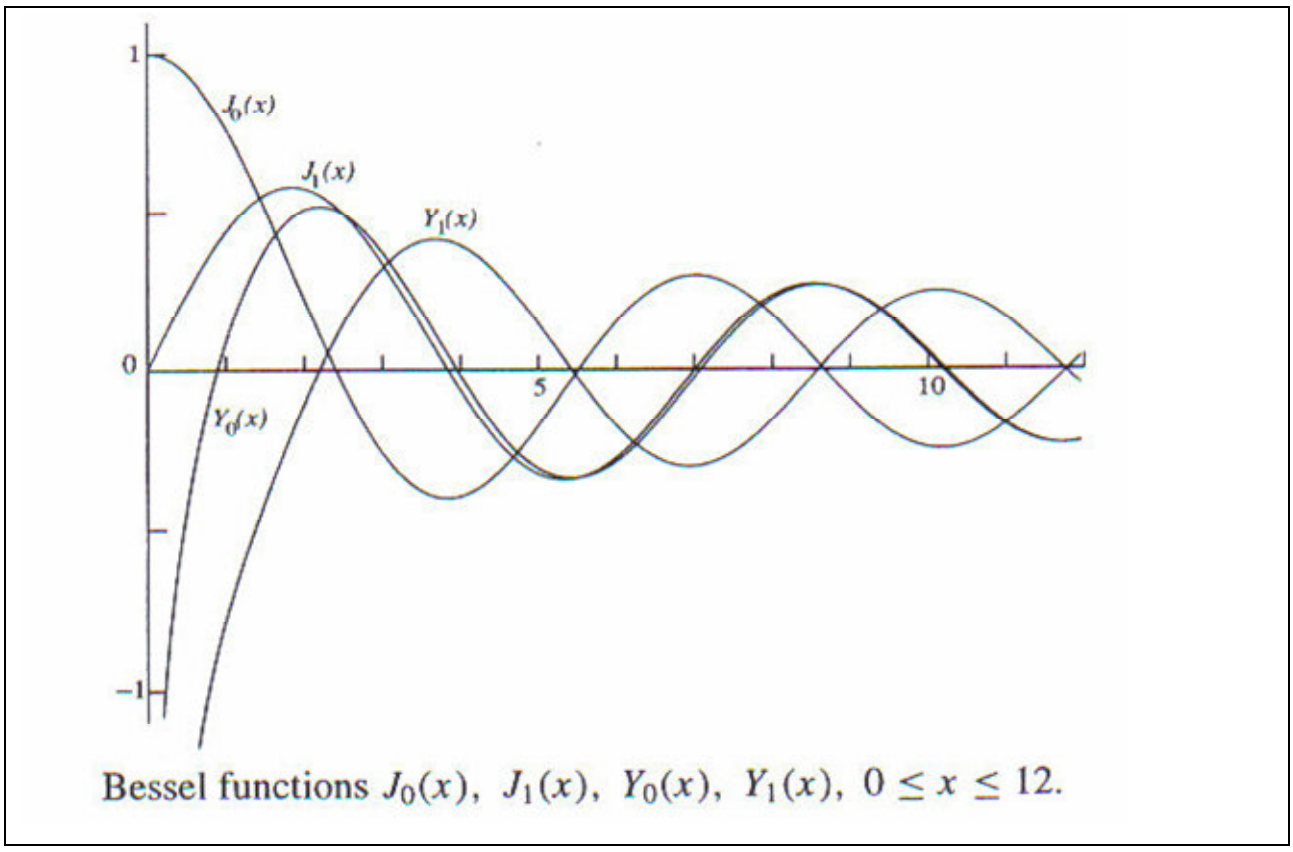

Figure F- 1: Bessel functions of the first and second kind of order 0 and 1, for $0 \leq x \leq 12$

The numerical values of the Bessel functions plotted in Figure F- 1 are tabulated in Table F- 1.

Table F- 1: Numerical values of Bessel functions (Abramowitz & Stegun, 1964)

x	$J_0(x)$	$J_1(x)$	$J_2(x)$	$Y_0(x)$
0	1.00000000	0.00000000	0.00000000	$-\infty$
0.2	0.99002497	0.09950083	0.00498335	-1.08110532
0.4	0.96039823	0.19602658	0.01973466	-0.60602457
0.6	0.91200486	0.28670099	0.04366510	-0.30850987
0.8	0.84628735	0.36884205	0.07581776	-0.08680228
1	0.76519769	0.44005059	0.11490349	0.08825696
1.2	0.67113274	0.49828906	0.15934902	0.22808350
1.4	0.56685512	0.54194771	0.20735590	0.33789513
1.6	0.45540217	0.56989594	0.25696775	0.42042690
1.8	0.33998641	0.58151695	0.30614354	0.47743171
2.0	0.22389078	0.57672481	0.35283403	0.51037567
2.2	0.11036227	0.55596305	0.39505869	0.52078429
2.4	0.00250768	0.52018527	0.43098004	0.51041475
2.6	-0.09680495	0.47081827	0.45897285	0.48133059
2.8	-0.18503603	0.40970925	0.47768550	0.43591599
3.0	-0.26005195	0.33905896	0.48609126	0.37685001
3.2	-0.32018817	0.26134325	0.48352770	0.30705325
3.4	-0.36429560	0.17922585	0.46972257	0.22961534
3.6	-0.39176898	0.09546555	0.44480540	0.14771001
3.8	-0.40255641	0. 01282100	0.40930431	0.06450325
4.0	-0.39714981	-0.06604333	0.36412815	-0.01694074
4.2	-0.37655705	-0.13864694	0.31053470	-0.09375120
4.4	-0.34225679	-0.20277552	0.25008610	-0.16333646
4.6	-0.29613782	-0.25655284	0.18459311	-0.22345995
4.8	-0.24042533	-0.29849986	0.11605039	-0.27230379
5.0	-0.17759677	-0.32757914	0.04656512	-0.30851763

F.2 Zeros of Bessel functions (Zwillinger, 1996)

For $\upsilon \geq 0$ in Equation F1, the zeros $\alpha_{\upsilon,n}$, $y_{\upsilon,n}$ of $J_\upsilon(x)$ and $Y_\upsilon(x)$ can be arranged as sequences:

$$0 < \alpha_{\upsilon,1} < \alpha_{\upsilon,2} < \alpha_{\upsilon,3} \ldots < \alpha_{\upsilon,n} < \ldots, \qquad \lim_{n\to\infty} \alpha_{\upsilon,n} = \infty \qquad \textbf{F 4}$$

$$0 < y_{\upsilon,1} < y_{\upsilon,2} < y_{\upsilon,3} \ldots < y_{\upsilon,n} < \ldots, \qquad \lim_{n\to\infty} y_{\upsilon,n} = \infty \qquad \textbf{F 5}$$

Between two consecutive positive zeros of $J_\upsilon(x)$, there is exactly one zero of $J_{\upsilon+1}(x)$. Conversely, between two consecutive positive zeros of $J_{\upsilon+1}(x)$, there is exactly one zero of $J_\upsilon(x)$. The same holds for the zeros of $Y_\upsilon(x)$. Moreover, between each pair of consecutive positive zeros of $J_\upsilon(x)$, there is exactly one zero of $Y_\upsilon(x)$, and conversely.

Table F- 2: Positive zeros $\alpha_{\upsilon,n}$, $y_{\upsilon,n}$ of Bessel functions $J_\upsilon(x)$, $Y_\upsilon(x)$, $\upsilon = 0, 1$.

n	$\alpha_{0,n}$	$\alpha_{1,n}$	$y_{0,n}$	$y_{1,n}$
1	2.40483	3.83171	0.89358	2.19714
2	5.52008	7.01559	3.95768	5.42968
3	8.65373	10.17347	7.08605	8.59601
4	11.79153	13.32369	10.22235	11.74915
5	14.93092	16.47063	13.36110	14.89744
6	18.07106	19.61586	16.50092	18.04340
7	21.21164	22.76008	19.64131	21.18807

F.3 Important integrals of Bessel functions (Abramowitz & Stegun, 1965)

1. $$\int_0^z r^v J_{v-1}(r)dr = z^v J_v(z), \qquad v > 0 \qquad \textbf{F 6}$$

2. $$\int_0^z r^{-v} J_{v+1}(r)dr = \frac{1}{2^v \Gamma(v+1)} - z^{-v} J_v(z) \qquad \textbf{F 7}$$

3. $$\int_0^z J_1(r)dr = -J_0(z) \qquad \textbf{F 8}$$

4. $$2n\int_0^z \frac{J_{2n}(r)dr}{r} = 1 - \frac{2}{z}\sum_{k=1}^{n}(2k-1)J_{2k-1}(z), \qquad n > 0$$ **F 9**

5. $$\int_0^z J_{n+1}(r)dr = \int_0^z J_{n-1}(r)dr - 2J_n(z), \qquad n > 0$$ **F 10**

APPENDIX G

CURVILINEAR COORDINATES

G.1 Cylindrical coordinates (Bird *et al.*, 2002)

Although formal derivations are usually made in Cartesian coordinates, for working problems it is often more natural to use curvilinear coordinates. The two most commonly occurring curvilinear coordinate systems are the cylindrical and the spherical.

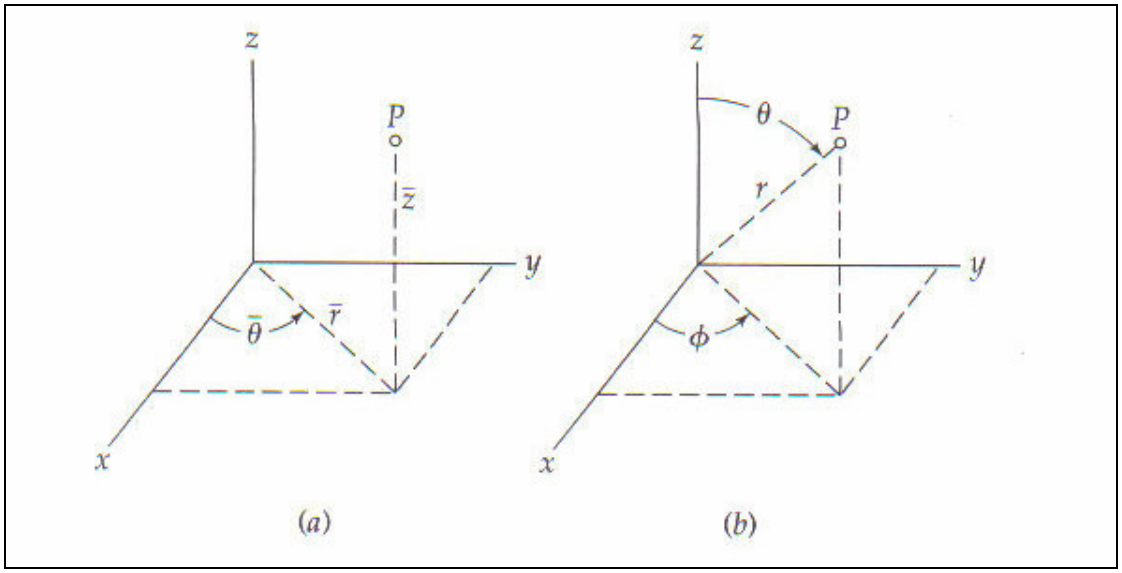

Figure G- 1: (a) Cylindrical coordinates and (b) Spherical coordinates

In cylindrical coordinates, instead of designating the coordinates of a point by x, y, z, a point is located by giving the values of r, θ, z. These coordinates are shown in Figure G- 1(a). They are related to the Cartesian coordinates by:

$$\begin{cases} x = r\cos\theta & r = +\sqrt{x^2 + y^2} \\ y = r\sin\theta & \theta = \arctan\left(y/x\right) \\ z = z & z = z \end{cases} \qquad \textbf{G 1}$$

To convert derivatives of scalars with respect to x, y, z into derivatives with respect to r, θ, z, the 'chain rule' of partial differentiation is used. The derivative operators are readily found to be related thus:

$$\begin{cases} \dfrac{\partial}{\partial x} = (\cos\theta)\dfrac{\partial}{\partial r} + \left(-\dfrac{\sin\theta}{r}\right)\dfrac{\partial}{\partial \theta} + (0)\dfrac{\partial}{\partial z} \\ \dfrac{\partial}{\partial y} = (\sin\theta)\dfrac{\partial}{\partial r} + \left(\dfrac{\cos\theta}{r}\right)\dfrac{\partial}{\partial \theta} + (0)\dfrac{\partial}{\partial z} \\ \dfrac{\partial}{\partial z} = (0)\dfrac{\partial}{\partial r} + (0)\dfrac{\partial}{\partial \theta} + (1)\dfrac{\partial}{\partial z} \end{cases} \qquad \textbf{G 2}$$

With these relations, derivatives of any scalar functions with respect to x, y, and z can be expressed in terms of derivatives with respect to r, θ, z.

G.2 Equations of motion for a Newtonian fluid

G.2.1 Cartesian coordinates (x, y, z)

$$\rho\left(\frac{\partial v_x}{\partial t} + v_x\frac{\partial v_x}{\partial x} + v_y\frac{\partial v_x}{\partial y} + v_z\frac{\partial v_x}{\partial z}\right) = \mu\left[\frac{\partial^2 v_x}{\partial x^2} + \frac{\partial^2 v_x}{\partial y^2} + \frac{\partial^2 v_x}{\partial z^2}\right] - \frac{\partial p}{\partial x} + \rho g_x \qquad \textbf{G 3}$$

$$\rho\left(\frac{\partial v_y}{\partial t} + v_x\frac{\partial v_y}{\partial x} + v_y\frac{\partial v_y}{\partial y} + v_z\frac{\partial v_y}{\partial z}\right) = \mu\left[\frac{\partial^2 v_y}{\partial x^2} + \frac{\partial^2 v_y}{\partial y^2} + \frac{\partial^2 v_y}{\partial z^2}\right] - \frac{\partial p}{\partial y} + \rho g_y \qquad \textbf{G 4}$$

$$\rho\left(\frac{\partial v_z}{\partial t} + v_x\frac{\partial v_z}{\partial x} + v_y\frac{\partial v_z}{\partial y} + v_z\frac{\partial v_z}{\partial z}\right) = \mu\left[\frac{\partial^2 v_z}{\partial x^2} + \frac{\partial^2 v_z}{\partial y^2} + \frac{\partial^2 v_z}{\partial z^2}\right] - \frac{\partial p}{\partial z} + \rho g_z \qquad \textbf{G 5}$$

G.2.2 Cylindrical coordinates (r, θ, z)

$$\rho\left(\frac{\partial v_r}{\partial t} + v_r\frac{\partial v_r}{\partial r} + \frac{v_\theta}{r}\frac{\partial v_r}{\partial \theta} - \frac{v_\theta^2}{r} + v_z\frac{\partial v_r}{\partial z}\right) =$$
$$\mu\left[\frac{1}{r}\frac{\partial}{\partial r}\left(r\frac{\partial v_r}{\partial r}\right) - \frac{v_r}{r^2} + \frac{1}{r^2}\frac{\partial^2 v_r}{\partial \theta^2} - \frac{2}{r^2}\frac{\partial v_\theta}{\partial \theta} + \frac{\partial^2 v_r}{\partial z^2}\right] - \frac{\partial p}{\partial r} + \rho g_r \qquad \textbf{G 6}$$

$$\rho\left(\frac{\partial v_\theta}{\partial t} + v_r\frac{\partial v_\theta}{\partial r} + \frac{v_\theta}{r}\frac{\partial v_\theta}{\partial \theta} + \frac{v_\theta v_r}{r} + v_z\frac{\partial v_\theta}{\partial z}\right) =$$
$$\mu\left[\frac{1}{r}\frac{\partial}{\partial r}\left(r\frac{\partial v_\theta}{\partial r}\right) - \frac{v_\theta}{r^2} + \frac{1}{r^2}\frac{\partial^2 v_\theta}{\partial \theta^2} + \frac{2}{r^2}\frac{\partial v_r}{\partial \theta} + \frac{\partial^2 v_\theta}{\partial z^2}\right] - \frac{1}{r}\frac{\partial p}{\partial \theta} + \rho g_\theta \qquad \textbf{G 7}$$

$$\rho\left(\frac{\partial v_z}{\partial t}+v_r\frac{\partial v_z}{\partial r}+\frac{v_\theta}{r}\frac{\partial v_z}{\partial \theta}+v_z\frac{\partial v_z}{\partial z}\right)=$$
$$\mu\left[\frac{1}{r}\frac{\partial}{\partial r}\left(r\frac{\partial v_z}{\partial r}\right)+\frac{1}{r^2}\frac{\partial^2 v_z}{\partial \theta^2}+\frac{\partial^2 v_z}{\partial z^2}\right]-\frac{\partial p}{\partial z}+\rho g_z \qquad \textbf{G 8}$$

G.2.3 Spherical coordinates(r,θ,ϕ)

$$\rho\left(\frac{\partial v_r}{\partial t}+v_r\frac{\partial v_r}{\partial r}+\frac{v_\theta}{r}\frac{\partial v_r}{\partial \theta}+\frac{v_\phi}{r\sin\theta}\frac{\partial v_r}{\partial \phi}-\frac{v_\theta^2+v_\phi^2}{r}\right)=-\frac{\partial p}{\partial r}+\rho g_r+$$
$$\mu\left[\frac{1}{r^2}\frac{\partial^2}{\partial r^2}\left(r^2 v_r\right)+\frac{1}{r^2\sin\theta}\frac{\partial}{\partial\theta}\left(\sin\theta\frac{\partial v_r}{\partial\theta}\right)+\frac{1}{r^2\sin^2\theta}\frac{\partial^2 v_r}{\partial\phi^2}\right] \qquad \textbf{G 9}$$

$$\rho\left(\frac{\partial v_\theta}{\partial t}+v_r\frac{\partial v_\theta}{\partial r}+\frac{v_\theta}{r}\frac{\partial v_\theta}{\partial \theta}+\frac{v_\phi}{r\sin\theta}\frac{\partial v_\theta}{\partial \phi}+\frac{v_r v_\theta-v_\phi^2\cot\theta}{r}\right)=-\frac{1}{r}\frac{\partial p}{\partial\theta}+\rho g_\theta+$$
$$\mu\left[\frac{1}{r^2}\frac{\partial}{\partial r}\left(r^2\frac{\partial v_\theta}{\partial r}\right)+\frac{1}{r^2}\frac{\partial}{\partial\theta}\left(\frac{1}{\sin\theta}\frac{\partial}{\partial\theta}\left(v_\theta\sin\theta\right)\right)+\frac{1}{r^2\sin^2\theta}\frac{\partial^2 v_\theta}{\partial\phi^2}+\frac{2}{r^2}\frac{\partial v_r}{\partial\theta}-\frac{2\cot\theta}{r^2\sin\theta}\frac{\partial v_\phi}{\partial\phi}\right] \qquad \textbf{G 10}$$

$$\rho\left(\frac{\partial v_\phi}{\partial t}+v_r\frac{\partial v_\phi}{\partial r}+\frac{v_\theta}{r}\frac{\partial v_\phi}{\partial \theta}+\frac{v_\phi}{r\sin\theta}\frac{\partial v_\phi}{\partial \phi}+\frac{v_r v_\phi+v_\theta v_\phi\cot\theta}{r}\right)=-\frac{1}{r\sin\theta}\frac{\partial p}{\partial\phi}+\rho g_\phi+$$
$$\mu\left[\frac{1}{r^2}\frac{\partial}{\partial r}\left(r^2\frac{\partial v_\phi}{\partial r}\right)+\frac{1}{r^2}\frac{\partial}{\partial\theta}\left(\frac{1}{\sin\theta}\frac{\partial}{\partial\theta}\left(v_\phi\sin\theta\right)\right)+\frac{1}{r^2\sin^2\theta}\frac{\partial^2 v_\phi}{\partial\phi^2}+\frac{2}{r^2\sin\theta}\frac{\partial v_r}{\partial\phi}+\frac{2\cot\theta}{r^2\sin\theta}\frac{\partial v_\theta}{\partial\phi}\right] \qquad \textbf{G 11}$$

APPENDIX H

MEMBRANE THICKNESSES

H.1 Preparation of samples for SEM imaging

After the experiment was stopped samples of the membrane with biofilm were cut using a sterile blade and placed into a 10% gluteraldehyde solution for 24hrs. The samples were then taken through an alcohol dehydration series (this replaces all the water in the sample with alcohol). This involved placing the samples in different concentrations of alcohol for at least 10 minutes. The concentrations used were: 30%, 50% 70% 80% 90% 95% 100%. Once the samples were in 100% alcohol they were taken to the Electron Microscopic Unit (EMU), University of Cape Town (RSA). At the EMU, they were critical point dried (CPD), this process involved replacing the alcohol with liquid carbon dioxide and eventually gaseous carbon dioxide. The samples were then dry and were mounted on small aluminium SEM stubs. They were then sputter coated with gold/palladium and were ready for examination with the SEM. Figure H- 1 is in image taken with the fully analytical Leo S440 SEM.

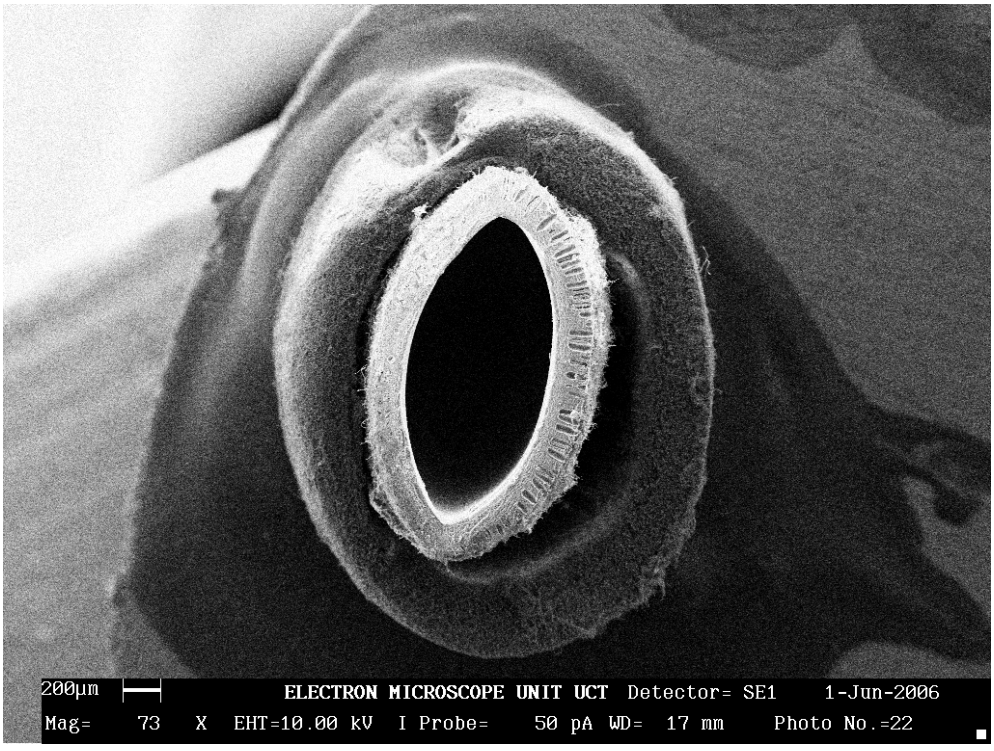

Figure H- 1: A scanning electron microscope image of a capillary membrane with biofilm

H.2 Thickness measurements

The SEM images of the membrane portions with *P. chrysosporium* growth are presented as TIFF files with the magnification, electron high tension (EHT), and aspect ratio provided at the bottom of the image as shown in Figure H- 1. Five representative measurements of the biofilm thickness were taken out of each SEM image, and the average of these values was taken to be the true biofilm thickness of that specific SEM image.

Representative samples of the membrane inlet, middle, and membrane outlet (with growth) were cut and prepared as was described in Section H.1., before thickness measurements were taken.